Study of thin liquid film drainage in bubble-liquid-solid systems using integrated thin liquid film force apparatus (ITLFFA)

by

Xurui Zhang

A thesis submitted in partial fulfillment of the requirements for the degree of

Doctor of Philosophy

in

Materials Engineering

Department of Chemical and Materials Engineering
University of Alberta

Abstract

Interactions involving deformable surfaces reveal a number of distinct physicochemical characteristics that do not exist in interactions between rigid solid surfaces. The main focus of this thesis is to develop a unique fully custom-designed instrument, referred to as an integrated thin liquid film force apparatus (ITLFFA) to investigate interactions between a deformable and a solid surface in liquids.

Incorporating a bimorph force sensor with interferometry, the ITLFFA allows simultaneous measurement of the time-dependent interaction forces and the corresponding spatiotemporal film thickness of the intervening liquid film. The ITLFFA possesses specific features of measurement under a wide range of hydrodynamic conditions, with a displacement velocity of deformable surfaces ranging from 2 μm/s to 50 mm/s. Equipped with a high speed camera, the results of a bubble interacting with hydrophilic and partially hydrophobic surfaces in aqueous solutions indicated that ITLFFA can provide information on interaction forces and thin liquid film drainage dynamics not only in a stable film but also in films of quick rupture process. The weak interaction force was extracted from a measured film profile. As a result of its well-characterized experimental conditions, ITLFFA permits the accurate and quantitative comparison/validation between the measured and calculated interaction forces and temporal film profiles.

Using the ITLFFA, the dynamic drainage process of the liquid film trapped between an air bubble and a flat silica surface over a wide range of hydrodynamic conditions was studied in aqueous solutions of different salt concentrations. Our study demonstrates that increasing the bubble approach velocity has a significant impact on the hydrodynamic pressure and fluid flow within the draining film, promoting the dimple formation and

increasing drainage time. The drainage time also depends on the competition between the electrical double-layer and van der Waals interactions, which are repulsive in our system, resulting in a stable liquid film on the hydrophilic surface, with the film thickness being determined by the balance of capillary pressure of the bubbles with the repulsive forces of the film scaled by the electrolyte concentrations. The evolution of the draining film is analyzed using the Stokes-Reynolds-Young-Laplace (SRYL) model. Comparisons between the theory and experimental results indicate that the model captures essential physical properties of the drainage system. Moreover, the thickness of the first occurrence of the dimple can also be precisely predicted from the bubble approach velocity with a simple analytical expression.

The dynamic thin liquid film drainage between a bubble and a hydrophobic solid surface of different hydrophobicities with nanoroughness was also studied using this device. For a given bubble approach velocity, the thickness of the first occurrence of the dimple for the hydrophobic surface was much thinner than that of the hydrophilic surface, indicating an apparent surface mobility on the hydrophobic surface. The experimental results were modelled by the SRYL model to obtain the degree of surface mobility for the hydrophobic surface as a function of bubble approach velocity, illustrating a velocity dependent surface mobility. Moreover, the thin film ruptured at thickness as large as hundreds of nanometers.

The major contributions to science of this thesis are developing a device-ITLFFA that performs the simultaneous measurement of dynamic forces and spatiotemporal film thickness during thin liquid film drainage between deformable and solid surfaces. It allows measurements over a wide range of hydrodynamic conditions that fills the experimental gap of current techniques. The systematic study of the effect of approach velocity and

surface hydrophobicity on the drainage dynamics of thin liquid films appealed us to consider them as vital parameters in the theoretical model that shed light on the problem of boundary condition and hydrophobic interaction.

Preface

This thesis is composed of a series of papers that have either been published or in preparation. The following is a statement of contributions made to the jointly authored papers contained in this thesis:

1. Xurui Zhang, Plamen Tchoukov, Rogerio Manica, Louxiang Wang, Qingxia Liu and Zhenghe Xu, Simultaneous measurement of dynamic force and spatial thin film thickness between deformable and solid surfaces by integrated thin liquid film force apparatus, *Soft Matter*, **2016**, 12, 9105. Zhang performed all the experiments and data analysis, and wrote the entire paper. All other authors contributed to the discussion on experimental design and interpretation of results, and commented on the manuscript.
2. Xurui Zhang, Rogerio Manica, Plamen Tchoukov, Qingxia Liu and Zhenghe Xu, Effect of approach velocity on thin liquid film drainage between an air bubble and a flat solid surface, *Journal of Physical Chemistry C*, **2017**, 121, 5573. Zhang performed all the experiments and data analysis, and wrote the entire paper. Manica helped with the modeling section. All other authors contributed to the discussion and commented on the manuscript.
3. Xurui Zhang, Rogerio Manica, Yuechao Tang, Plamen Tchoukov, Qingxia Liu and Zhenghe Xu, Measurement of hydrodynamic boundary condition at hydrophobic surfaces during bubble impact, in preparation. Zhang performed all the experiments and data analysis, and wrote the entire paper. Manica helped with the modeling section. Tang was responsible for the AFM images. All other authors contributed to the discussion and commented on the manuscript.

Other co-authored publications not listed as Thesis Chapters include:

Chen Shi, Xin Cui, **Xurui Zhang**, Plamen Tchoukov, Qingxia Liu, Noemi Encinas, Maxime Paven, Florian Geyer, Doris Vollmer, Zhenghe Xu, Hans-Jürgen Butt, and Hongbo Zeng, Interaction between air bubbles and superhydrophobic surfaces in aqueous solutions, *Langmuir*, **2015**, 31, 7317. Zhang was responsible for the experiments between the macroscopic bubble and superhydrophobic surface.

- Yuechao Tang, **Xurui Zhang**, Qingxia Liu and Zhenghe Xu, Probing Single-Molecule Adhesion of a Stimuli Responsive Oligo (ethylene glycol) Copolymer on a Molecularly-smooth Hydrophobic MoS_2 Basal Surface, *Langmuir*, DOI: 10.1021/acs.langmuir.7b01187. Zhang helped with the data analysis.

Acknowledgements

I would like to express my gratitude and appreciation to:

- My supervisors, Dr. Zhenghe Xu and Dr. Qingxia Liu for their guidance, patience, encouragement and support in my research and throughout each stage of my graduate studies.
- Dr. Plamen Tchoukov for introducing me to this project and helping me grow up to a professional researcher.
- Dr. Rogerio Manica for the help on the modelling part and discussion and suggestions on papers.
- Dr. Louxiang Wang for teaching me how to use the previous version of the instrument and lots of help when I first came to Canada.
- Mr. Les Dean, Mr. Robert Smith and Mr. Walter Boddez for their useful discussions and help on the design of the new apparatus.
- Mr. James Skwarok, Ms. Jie Ru and Ms. Ni Yang for their help in locating supplies and instrument training.
- Ms. Lisa Carreiro, Ms. Patricia Siferd, Mr. Carl Corbett and Ms. Lily Laser for administrative and technical assistance.
- All the fellow members and friends in Oil Sands Research Group, in particular, Dr. Natalie Kuznicki, Ms. Yin Liang, Ms. Jiebin Bi, Ms. Adriana Briones, Dr. Fan Yang, Dr. Erica Pensini and Dr. Meijiao Deng for the enjoyable research experience. Mr. Baurzhan Primkulov for helping me with the initial data analysis program.
- NSERC Industrial Research Chair Program in Oil Sands Engineering and Alberta Innovates- Energy and Environmental Solutions (AI-EES) for financial support.

Finally, my deepest gratitude goes to my daughter, husband and parents. I am forever grateful for the everlasting love and support of them. Thank you for keeping me happy in the stressful time and inspiring me to be better. It is to you that I dedicate this work.

Table of Contents

List of Tables

List of Figures

Nomenclature

Symbols

$u(r,z,t)$	Velocity of liquid in the radial direction, m/s
μ	Viscosity of solution, Pa·s
$p(r,t)$	Pressure in the film, N/m^2
r	Radial direction, m
z	Vertical direction, m
$h(r,t)$	Film thickness, m
h_0	Film thickness in the center of the film, m
h_b	Film thickness at the barrier rim of the film, m
R	Radius of air bubble, m
R_b	Radius of the barrier rim of the film, m
σ	Surface tension of liquid, N/m
$\Pi(h)$	Disjoining pressure, N/m^2
r_{max}	Outer computational domain, m
K	Spring constant of the cantilever, N/m
θ	Contact angle, ^{o}
b_0, b_h	Slip length, m
$V(t,0)$	Volume of water in the film in the absence of a disjoining pressure, m^3
$V(t,\Pi)$	Volume of water in the film in the presence of a disjoining pressure, m^3
F	Force, N
Q	Accumulated charge, C
d_{13}	Piezo material charge constant,
L	Length, m
E	Young's Modulus, N/m^2
I	Moment of inertia of the bimorph, kg·m^2
$I(r,t)$	Instantaneous light intensity
I_{max}, I_{min}	Maximum and minimum light intensity
λ	Wavelength of the light, m

n_1, n_2, n_3	Refractive index of bubble, liquid and solid
γ	Interfacial tension of air-water interface, N/m
R_0	Radius of bubble, m
r_c	Radius of contact area, m
Re	Reynolds number
V	Approach velocity of bubble, m/s
ρ	Density of water, kg/m^3
$X(t)$	Distance between the end of the capillary and un-deflected bimorph, m
$S(t)$	Deflection of the bimorph, m
Π_{edl}	Electrostatic double layer interaction energy, J/m^2
Π_{vdw}	van der Waals interaction energy, J/m^2
A	Hamaker constant, J
k	Boltzmann constant, J/K
T	Temperature, K
κ^{-1}	Debye length, m
$\varphi_{sl}, \varphi_{bl}$	Surface potential of solid-liquid and bubble-liquid interface, V
$\dot{\gamma}$	Shear rate, /s
h_d	Film thickness of dimple formation, m
Ca	Capillary number
Pe	Peclet number
b	Slip length, m

Abbreviations

TPCL	Three phase contact line
AFM	Atomic force microscope
SRYL	Stokes–Reynolds–Young–Laplace
SFA	Surface force apparatus
ITLFFA	Integrated thin liquid film force apparatus
DLVO	Derjaguin-Landau-Verwey-Overbeek

SDS	Sodium dodecylsulfate
RICM	Reflection interference contrast microscopy
ITFDA	Integrated thin film drainage apparatus
TIR-FRAP	Total internal reflection – fluorescence recovery after photobleaching
OTS	Octadecyltrichlorosilane
SAXS	Small-Angle X-ray Scattering
TIRF	Total Internal Reflection Fluorescence
CCD	Charge-coupled device
FEP	Fluorinated ethylene propylene
DMDCS	Dimethyldichlorosilane
RMS	Root mean square

Chapter 1 Introduction

1.1 Background and motivations

The interaction between deformable droplets or bubbles and solid surfaces in aqueous medium is of paramount importance in various technologies. The key physical process of this interaction is the dynamic drainage of the thin liquid film through which the two dispersed phase (bubbles/droplets and solids) interact with each other. Particularly, this intervening film is vitally important to the flotation separation process that is widely used in the recovery of coal and valuable minerals from the rock, in the treatment and purification of wastewater, and in the de-inking of wastepaper. Generally, the flotation separation is achieved by introducing air bubbles into a pulp that contains hydrophilic and hydrophobic particles. Upon collision of bubbles with hydrophobic particles, bubble-particle aggregates can form so that the rising air bubbles carry the particles to the surface, leaving the hydrophilic particles behind, which settle to the bottom to be discharged. The successful attachment of a bubble to a particle relies on a number of sub-processes. Initially, the liquid film between the bubble and particle will become thinner as the liquid inside the film drains. If the particle is hydrophilic, a stable film will form eventually so that there is no attachment between the bubble and particle. Inversely, if the particle is hydrophobic, the film ruptures at a critical thickness, creating a three phase contact line (TPCL), which spreads further to form a stable perimeter and leads to successful attachment. This whole drainage process determines the efficiency of recovery process. Therefore, a more comprehensive understanding and controlling of the interactions between bubbles/droplet and solid surfaces, especially under dynamic conditions, is essential.

The past decades witnessed numerous techniques developed for studying the interaction between bubbles/droplets and solid surfaces, which can be divided into two groups. The

first group of technique focused on the direct force measurement between deformable and solid surfaces. The atomic force microscope (AFM) with colloidal probe has been used to measure time dependent forces between pairs of drops, bubbles, solid particles and flat surfaces in relative motion. The measured force has been well interpreted by Stokes–Reynolds–Young–Laplace (SRYL) model without any accessible information of bubble/droplet deformation. The other group of technique concerned the film geometry. The temporal and spatial film thickness during the dynamic drainage process was measured by Scheludko cell, bubble expansion method, SFA and rising bubble method. Although these techniques have improved our understanding of interactions involving deformable surfaces, the simultaneous measurement of bubble/droplet geometric deformations and the strength of the interaction is missing. From hydrodynamic point of view, the measurements were conducted within very low Reynolds number regime ($<10^{-2}$) by AFM, Scheludko cell, bubble expansion method and SFA, while the rising bubble method only covered high Reynolds number regime that is larger than 50. There is still an unexplored area from small to intermediate Reynolds number regime (10^{-2}-50).

Interactions involving hydrophobic surfaces play a key role in a wide range of natural phenomena and industrial processes, such as protein folding and separation of oil and water. The basis of this type of interactions is specific orientation of water molecules near non-polar surfaces, which affects its 3D hydrogen bonding network and loses configurational entropy. However, the detailed mechanism of the hydrophobic interaction as well as the precise range and magnitude of such interaction remains under debate even after extensive studies for decades. In this problem, the related topics of the existence and degree of the slip of liquid water on hydrophobic surface remain a subject of controversies.

1.2 Objectives and scope of the thesis

The main objective of this work is to fill the experimental gap of current techniques for investigating the interaction involving deformable surfaces and provide valuable insights to the remaining unsolved problems by interpreting the experimental data using appropriate model.

In the first part of the thesis, integrated thin liquid film force apparatus (ITLFFA) was developed to study the interaction between deformable and solid surfaces. To illustrate the feasibility of the new device, the interaction forces and spatiotemporal film thickness were simultaneously measured between the bubble and hydrophilic/hydrophobic surfaces. The calculated forces from the film profiles matched very well with the measured forces.

The effect of hydrodynamic condition within intermediate Reynolds number regime on the dynamic film drainage process was systematically studied in the second part of the thesis. The model prediction agreed with the experimental results very well, confirming the accurate measurement of this device and expanding the application of the model to a wider range of hydrodynamic condition.

In the last part of the thesis, the interaction between a bubble and hydrophobic surface was studied by the ITLFFA and the model was used for theoretical explanation of experimental phenomena. The study mainly focused on the effect of hydrophobicity and approach velocity on the boundary condition of the hydrophobic surface with nanoroughness.

The major contributions of this thesis to science is developing a unique fully-custom-designed instrument, referred to as integrated thin liquid film force apparatus (ITLFFA), which allows simultaneous measurement of time-dependent interaction forces and spatiotemporal film thickness of the intervening liquid film in a wide range of

hydrodynamic condition. Using the unique features of the new device, the effect of hydrodynamic conditions of the experiment and hydrophobicity of the solid surfaces on the dynamic drainage process between a bubble and solid surface was explored, which provided valuable insights into an important solid-liquid boundary condition problem under debate.

1.3 Structure of the thesis

This thesis has been structured as a compilation of papers. Chapters 3-5 are research papers published in or submitted to scientific journals. The key content of each chapter is shown as follows:

Chapter 1 presents the overall introduction of the thesis, including the background and motivations, objectives and the scope of the thesis.

Chapter 2 provides a comprehensive literature review on the current experimental and theoretical researches of the dynamic interaction involving deformable surfaces. The main controversies in this subject are also discussed.

Chapter 3 introduces the developed instrument called integrated thin liquid film force apparatus (ITLFFA). The main features of this device are demonstrated and its accuracy is verified. A version of this chapter has been published in:

Xurui Zhang, Plamen Tchoukov, Rogerio Manica, Louxiang Wang, Qingxia Liu and Zhenghe Xu, Simultaneous measurement of dynamic force and spatial thin film thickness between deformable and solid surfaces by integrated thin liquid film force apparatus, *Soft Matter*, **2016**, 12, 9105.

Chapter 4 illustrates the use of ITLFFA to study the effect of approach velocity on the interaction between a bubble and a hydrophilic surface. Comparison of the experimental

results and theoretical prediction reveals the essential physical properties of the dynamic interaction. A version of this chapter has been published in:

Xurui Zhang, Rogerio Manica, Plamen Tchoukov, Qingxia Liu and Zhenghe Xu, Effect of approach velocity on thin liquid film drainage between an air bubble and a flat solid surface, *Journal of Physical Chemistry C*, **2017**, 121, 5573.

Chapter 5 discusses the use of ITLFFA to investigate the interaction between a bubble and a hydrophobic surface with nanoroughness. The hydrophobicity and velocity dependent surface mobility was observed by fitting the experimental data with theoretical model. A version of this chapter has been prepared as:

Xurui Zhang, Rogerio Manica, Yuechao Tang, Plamen Tchoukov, Qingxia Liu and Zhenghe Xu, Measurement of hydrodynamic boundary condition at hydrophobic surfaces during bubble impact, in preparation.

Chapter 6 presents the conclusions of this thesis and recommendations for future research. The Appendix at the end of the thesis provides addition calculations and figures for each chapter.

Chapter 2 Literature review-Thin liquid film drainage involving deformable surfaces

2.1 Introduction

Interactions involving deformable surfaces are of paramount importance in diverse technologies such as mineral flotation[1-2], wastewater treatment[3], bioprocessing[4] and drug delivery[5]. Unlike rigid surfaces, deformable surfaces can change shape in response to local variations of the interaction forces so that it encompasses a number of distinguishing physicochemical characteristics that do not exist in interactions between rigid solid surfaces. A thin liquid film of continuous phase entrapped between surfaces drains under the influence of interaction forces, leading to a stable or rupture film. Thus, this dynamic drainage process characterizes all the features of interactions involving deformable surfaces. To have a complete and deep understanding of thin liquid film drainage process, two essential elements are required: spatiotemporal film thickness and interaction forces. The top priority is to understand the interdependence of these two elements.

The purpose of this chapter is to show an overview of experimental studies of dynamic thin liquid film drainage process involving deformable surfaces and find out the unexplored field of current techniques. The development of theoretical models that reveal the physical fundamentals in the drainage process are reviewed as well. The study of controversies on hydrodynamic boundary condition and hydrophobic interaction is discussed to point out a direction for future research.

2.2 Experimental studies

The first qualitative experimental investigation of interactions involving deformable surfaces was done by Derjaguin and Kussakov[6]. They observed the evolution of the thin liquid film between an air bubble and a flat glass plate and deduced that a non-equilibrium

film forms a dimple. Since then, the past decades witnessed the development of various experimental approaches that have been used to study interactions involving deformable surfaces. The current techniques are summarized as follows:

2.2.1 Bubble expansion method

This technique was first developed by Fisher and co-workers[7-8] in 1990s to measure the spatiotemporal film thickness of thin aqueous draining film between air bubbles and solid surfaces using optical interference fringe patterns. As shown in Figure 2-1, the air bubble A was forced from a capillary against a quartz surface Q where the axis of the capillary was perpendicular to the surface. The air bubble was bulged by allowing a spring-loaded plunger P to compress a section of silastic tubing T. The spatiotemporal film thickness was obtained by monitoring time variations of the intensity of the reflected light at different positions of the film. The light can be scanned across the whole film as the beamsplitter B and objective O were able to move laterally.

With this apparatus, they found that the pure water film is thicker than that of the salt solution film at all times when an air bubble interacts with hydrophilic quartz surface. For hydrophobic surface, the film drained more rapidly than that in hydrophilic case and eventually ruptured. Due to the uncertainty of determining the absolute film thickness in hydrophobic case, it was difficult to do quantitative study in depth. Therefore, they studied the effect of salt concentration on thin liquid film drainage between an air bubble and hydrophilic surface using this technique in a following work[9]. They observed that an increase in salt concentration increased the rate of drainage at the boundary ring of the draining film but was accompanied by a decrease at the center of the film. Reasonable agreement was obtained between experimental equilibrium film thicknesses and those

predicted by the standard DLVO theory.

The bubble expansion method initiated a way of quantitative measurement of spatiotemporal film thickness in dynamic film drainage process. However, recording the whole picture of the film at one time is required to acquire smooth profile of the film. In addition, appropriate characterization of how the bubble is driven towards the surface is needed for quantitative analysis.

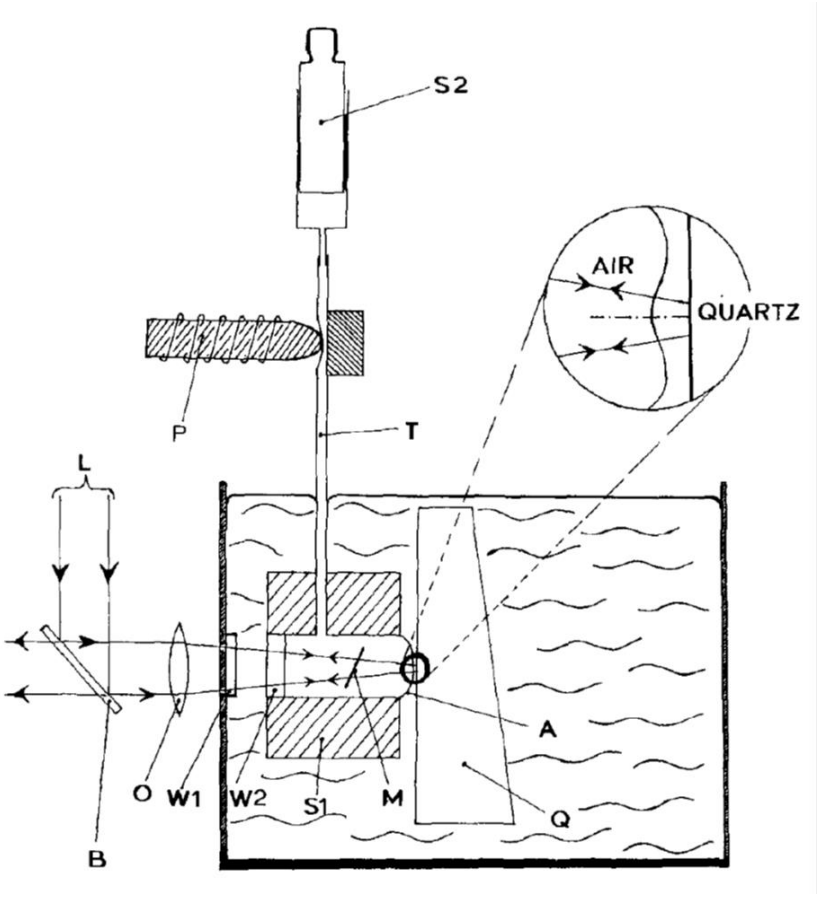

Figure 2-1. Schematic of bubble expansion technique that is used to measure the time-dependent shape of thin liquid film between air bubbles and solid surfaces[7].

2.2.2 Scheludko cell

The University of Sofia has pioneered the study of dynamic drainage of foam and emulsion film by using a cylindrical cell called Scheludko cell. When studying the film between

bubbles and solid surfaces, the Scheludko cell was modified to meet the requirements of gas/liquid/solid system. In this technique, the film was formed by pressing a captive air bubble against a flat solid surface through a capillary (Figure 2-2a), or withdrawing the liquid in the cell between two approaching surfaces (Figure 2-2b). The first method was used to provide an experimental check of Frankel-Mysels Theory in 1964[10], which describes the "dimpling" shape of the film by giving the temporal film thickness of the center and the barrier rim of the film. It was proved that the Frankel-Mysels Theory accounted fairly well for the observed shape in the case of liquid film on the solid substrate without considering the initial stage of the dimpling. The thickness of the film between an air bubble and a hydrophilic silica surface was also investigated using the first method. The aqueous solution of hydrophobically modified inulin polymeric surfactant was studied to explain the stabilizing mechanism of solid particles in liquid dispersions by this polymeric surfactant[11]. A detailed experimental study of the profile of the transition region between the film and the adjacent meniscus has been performed by the second method[12-13]. The profiles obtained for KCI solutions with different concentrations and those theoretically calculated on the basis of a suitable disjoining pressure isotherm were found to be in good agreement.

Although the Scheludko cell is able to measure the film thickness accurately using microinterferometric technique, quantitative details of the spatial film thickness and liquid withdraw conditions are often not reported.

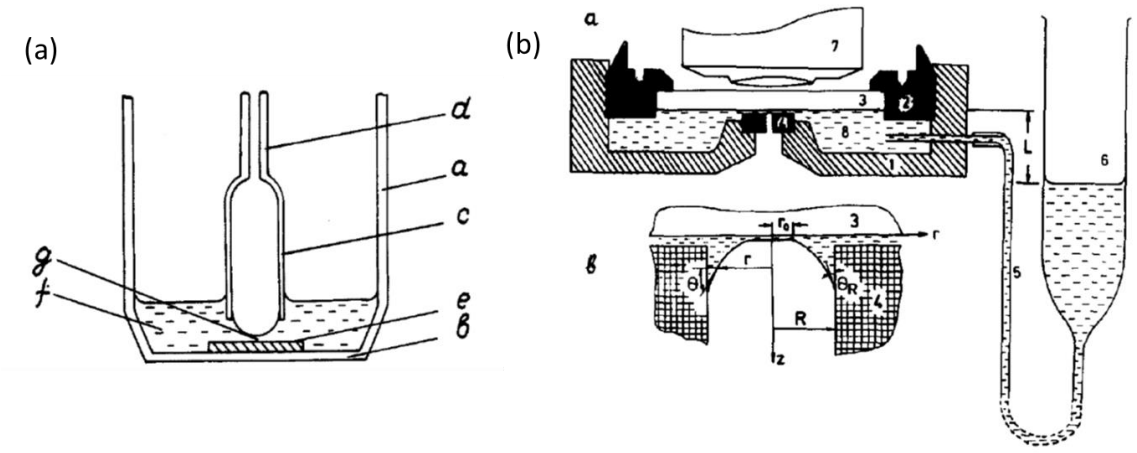

Figure 2-2. Schematic of modified Scheludko cell for investigation of thin liquid film drainage between air bubbles and solid surfaces[10, 13].

2.2.3 Surface force apparatus (SFA)

The surface force apparatus (SFA), first developed in 1969 by Tabor, Winterton and Israelachvili, has been used for decades to measure physical forces between surfaces, such as van der Waals and electrostatic forces in vapors and liquids[14]. With appropriate modification by Horn et al.[15] (Figure 2-3), this technique accurately tracks the evolution of spatiotemporal film thickness of aqueous films trapped between a mercury drop and a mica surface using fringes of equal chromatic order. Due to the high reflectivity of the mercury drop, this method is capable of measuring film thickness with sub-nanometre resolution. The use of mercury drop allowed the control of the strength and sign of the electrostatic force between mercury and mica surface. Such studies provided insights into the role of attractive and repulsive surface force in determining the dynamic film drainage process that led to either a stable equilibrium film or rupture film. Further analysis of hydrodynamic pressure by subtracting disjoining pressure from the total film pressure indicated that hydrodynamic pressure compensated different disjoining pressures to maintain the total film pressure constant within the dimple region[16].

The same technique has also been used to study the interaction between an air bubble and a mica surface in water and electrolyte solutions with different concentrations[17]. It was found that the air bubble was negatively charged with surface potentials of only a few millivolts in the low electrolyte concentrations. The charge of the air-water interface changed from negative to positive when the bubble approached to the mica surface.

Although the SFA could have been used to measure the interaction force, the experiments mentioned above mainly focus on the film drainage process.

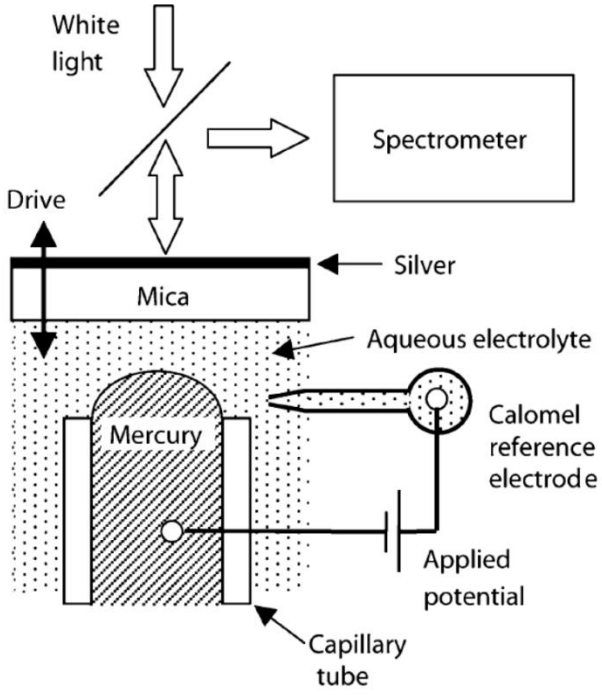

Figure 2-3. Schematic diagram of Surface force apparatus (SFA) for studying thin liquid film drainage between a mercury droplet and a mica surface[15].

2.2.4 Atomic force microscope (AFM)

The Atomic force microscope (AFM) was invented by IBM Scientists in 1982 to conduct imaging and direct force measurement with a sharp tip. In early 1990s, the emergence of the colloidal probe technique[18] allowed direct force measurement involving deformable surfaces by AFM. The earliest attempt of this technique was measuring the colloidal forces

between a colloid particle and a sessile air bubble on a substrate in aqueous solutions[19-20] (Figure 2-4a). The strong long-range attractive forces were observed between hydrophobic silica particles and air bubbles that indicated the hydrophobic nature of air-water interface. The long-ranged attractive component of the force was found to disappear when the anionic surfactant sodium dodecylsulfate (SDS) was added to the solution. The radius of the sessile air bubble is around 250 μm. In order to study the interaction involving small bubbles with a diameter of about 100 μm, the colloidal probe technique was extended to attach small, ultrasonically generated bubbles in water onto the V-shaped cantilever[21] (Figure 2-4b). The dynamic forces between bubbles and different solid surfaces were measured using this approach. Compared to the Navier slip model, the hydrodynamic response of the air/water interface can range from a classical fully immobile surface in the presence of added surfactants to a partially mobile interface in an electrolyte solution without added surfactants[22-23]. The repulsive van der Waals force was proved to exist between bubbles and solid surfaces and its strength depended on the material of the surface[24]. The coalescence between bubbles and drops under a range of solution conditions was also widely studied by this technique[25-28]. Unfortunately, none of the studies mentioned above is able to determining the extent of bubble deformation, which had to be inferred from theoretical model of the drainage process.

Complementary to force measurements by colloidal probe technique using AFM, the combination of AFM and confocal fluorescence microscopy was used to analyze the interaction forces and spatial position of oil droplets[29]. Recently, the AFM integrated with reflection interference contrast microscopy (RICM) has been adapted recently to measure simultaneously the interaction force and the spatiotemporal film thickness between a

bubble and mica surfaces with varying degrees of hydrophobicity in water[30]. The excellent agreement between theory and experimental results was reached with low driving velocity of bubble.

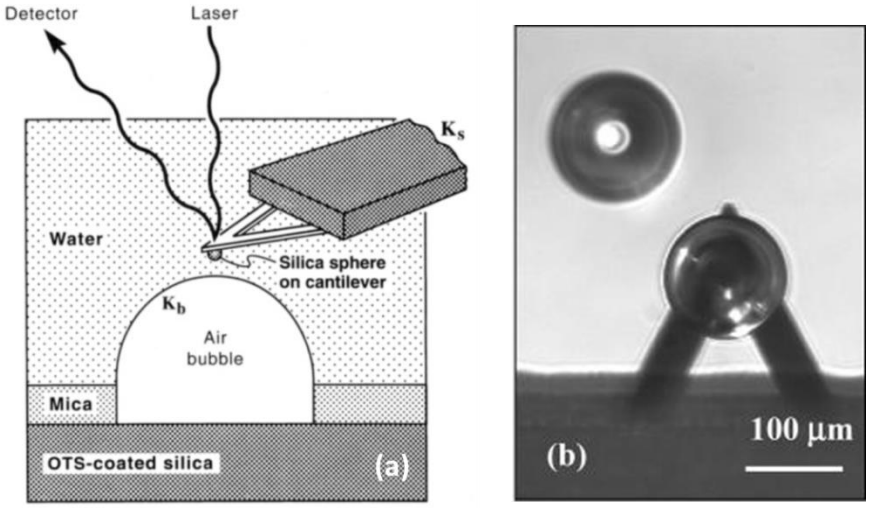

Figure 2-4. (a) Schematic figure of the experiment for measuring interaction forces between a silica particle and a sessile air bubble. (b) Optical microscopy image of a cantilever with an attached air bubble[19, 21].

2.2.5 Rising bubble method

Unlike other techniques that study the interaction between bubbles and solid surfaces with bubble driving velocity of a few µm/s, the rising bubble method has provided the measurement with the terminal velocity of the bubble in the order of cm/s. In this technique, a single air bubble with hundreds of micron to millimeter size is generated at the end of a syringe and freely rises under buoyancy force in aqueous solution towards a horizontal solid surface (Figure 2-5)[31]. The initial bubble–solid surface encounter was dominated by inertial effect. The trajectories of the bubbles were tracked in the presence of different surface active substances[32-33]. It was found that the velocity and deformation of the bubble

decreased with surfactant concentration as a result of retardation of fluidity of the liquid/gas interface by adsorption layer of surfactant molecules. The presence of surfactant and roughness of the solid surface increased probability of the bubble attachment to the solid surface. The study between a very small rising bubble in tens of micron size and solid surface allowed the investigation of surface forces between these two interfaces by excluding the necessity for complex hydrodynamic analysis[34-35]. The transition of bubble boundary condition from full-slip to no-slip during the rising process in the absence of surfactant was observed. The film drainage dynamics was dominated by the surface forces in such condition. Recently, the spatiotemporal film thickness of the trapped water film between rising bubble and glass plate was recorded by high-speed interferometry[36], which provides the possibility to capture the essential physics of the bubble impact process by appropriate model.

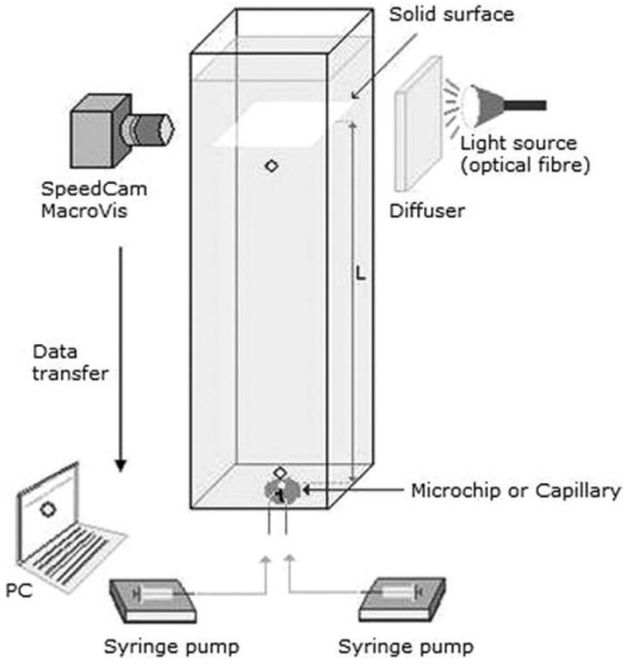

Figure 2-5. Experimental setup for monitoring rising bubble interacts with solid surfaces[31].

2.2.6 Integrated thin film drainage apparatus (ITFDA)

In AFM, due to the narrow range of approach speed of the probe (up to about 100 μm/s of micron size probes), the hydrodynamic condition is confined to the relatively low Reynolds number regime that characterizes the motion of the deformable surface ($<10^{-2}$). Similarly, hydrodynamic conditions covered by the experiments using the bubble expansion method, Scheludko cell and SFA are also within the low Reynolds number regime. At the other extreme, the free rising bubble method leads to drainage dynamics of the trapped thin aqueous film in a Reynolds number higher than 50. Therefore, there remains an unexplored domain defined from small to intermediate Reynolds number regime (10^{-2}-50). This experimental gap has been partially filled using the integrated thin film drainage apparatus (ITFDA)[37] developed recently in our group (Figure 2-6). The ITFDA is designed to measure the interaction force between a bubble/droplet and a solid sphere with milli-meter size range in different liquids. A bubble/droplet is generated using gas-tight microsyringe at the end of a glass capillary tube, which is connected to a speaker diaphragm. The speaker is used to drive the bubble/droplet towards the solid particle with well-controlled velocity in the range from 2 μm/s to 50 mm/s within the intermediate Reynolds number regime. The cameras in orthogonal directions provide the view to align the two interfaces, control the size of the bubble/droplet as well as the initial gap between the bubble/droplet and the solid particle. The time-dependent interaction force was measured when the capillary tube drives the bubble to approach or retract away from the solid sphere in well-controlled manner by using bimorph as a force sensor.

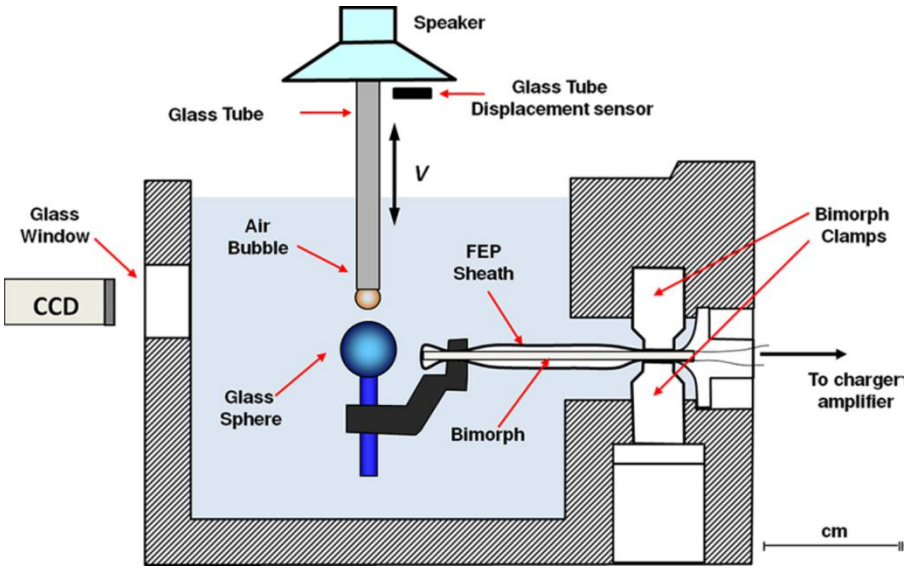

Figure 2-6. Schematic view of the integrated thin film drainage apparatus (ITFDA)[37].

In summary, each of the experimental methods described above suffers some inherent limitations although each has particular strength. The bubble expansion method, Scheludko cell, SFA and rising bubble method is mainly focus on measuring the film thickness during the drainage dynamics. On the other hand, the AFM and ITFDA are designed to measure interaction forces. Although the AFM has been modified to realize the coupling measurement of interaction force and film thickness, it's still under the very low Reynolds number regime. Thus, it is required to have some technique that is capable to measure the interaction force and film thickness simultaneously under the intermediate Reynolds number regime.

2.3 Theoretical studies

The experimental results need to be explained in depth by an applicable theory. The hydrodynamic fluid flow draining in the thin film trapped between deformable and solid surfaces can be described by lubrication theory under low Reynolds number regime. Within the axisymmetric film, the dominant velocity component is in the radial r-direction,

$u(r,z,t)$ and the pressure p only varies in the r-direction. Thus, the flow in the film is described by the radial component of the Stokes equations:

$$\mu \frac{\partial^2 u(r,z,t)}{\partial z^2} = \frac{\partial p(r,t)}{\partial r} \tag{2-1}$$

where μ is the viscosity of the continuous medium.

Integration of the continuity equation from $z = 0$ to $h(r,t)$ together with the kinematics condition on the film surface gives the equation for the time evolution of the film thickness:

$$\frac{\partial h(r,t)}{\partial t} = -\frac{1}{r}\frac{\partial}{\partial r}\left(r \int_0^{h(r,t)} u(r,z,t)dz\right) \tag{2-2}$$

If the hydrodynamic boundary conditions are specified at the film surface ($z = 0$ and $z = h$), $u(r,z,t)$ can be found by integrating eqn (2-1) with respect to z. Substitution of the solution into eqn (2-2) will give an equation relating $h(r,t)$ and $p(r,t)$, which provide a description of temporal evolution of the film thickness. Together with different models that describe the spatial film thickness, the physical essential in the dynamic drainage of the thin film trapped between deformable surfaces and solid surfaces can be elucidated in details.

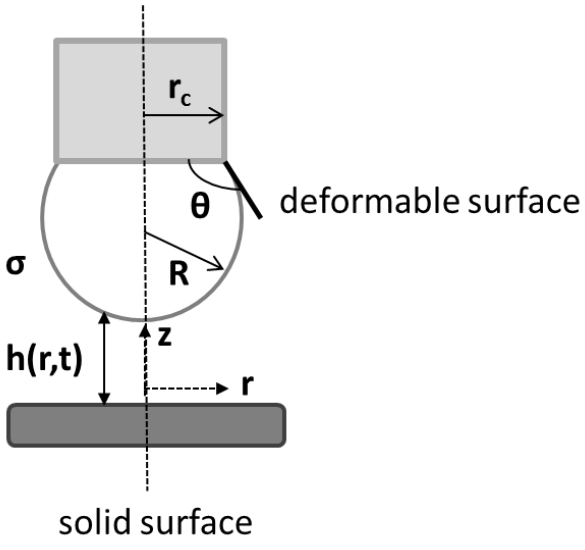

Figure 2-7. Schematic of deformable surface interacting with a solid surface.

2.3.1 Stefan–Reynolds model

The Stefan-Reynolds model is the first theoretical model of film drainage between a deformable surface and a flat solid surface[38]. In spite of the spatial film information, the deformation of the bubble/droplet was assumed to be a circular flat disk of some radius. Considering the no-slip boundary condition for the flat solid surface, the rate of the film thinning can be written as:

$$\frac{dh}{dt} = -\frac{\beta h^3 (p(r,t) - p_0)}{3\mu R_f} \tag{2-3}$$

where p_0 is the pressure in the bulk liquid. $\beta = 1$ if the flat surface of the bubble/droplet is tangentially immobile and $\beta = 4$ if the flat surface of the bubble/droplet is fully mobile. When the film radius is very small and the flat film formed, the Stefan-Reynolds model can be applied. However, the intervening film is usually not plane parallel but dimpled, especially for large film radius. For the case of the dimple formation, a few models were derived. One of the first models that consider dimple formation was elaborated by Frankel and Mysels[39]. In this model, the rate of the film thinning through the barrier rim was assumed to be independent on the film radius. The film thickness in the center of the dimple (h_0) and at the barrier rim (h_b) is written as follows:

$$h_0 = \left(\frac{0.0096\mu R_b^6}{\sigma R t}\right)^{1/4} \tag{2-4}$$

$$h_b = \left(\frac{0.009\mu R_b^2 R}{\sigma t}\right)^{1/2} \tag{2-5}$$

where R is the radius of the deformable surface. R_b is the radius of the barrier rim and σ is the surface tension of water. This model predicts that the shape of the dimple becomes more pronounced as the film drains, which is inconsistent with experimental observation[10].

Therefore, Hartland and Robinson[40] developed a model to approximate the shape of the dimple by three linked parabolas, which led to the following equations for the temporal film thickness:

$$h_0 = 0.117\left(\frac{2\pi\mu R_b^6}{\sigma R t}\right)^{1/4} \tag{2-6}$$

$$h_b = 0.370\left(\frac{\mu R_b^2 R}{2\pi\sigma t}\right)^{1/2} \tag{2-7}$$

Dimitrov and Ivanov[41] derived the film thickness as a function of time based on the assumption that the energy dissipation occurred at the barrier rim:

$$h_0 = \left(\frac{\mu R_b^2 R}{\sigma t}\right)^{1/2} \tag{2-8}$$

Later, Jain and Ivanov[42] introduced a "step" model for the film drainage and the film thickness at the barrier rim is given as:

$$h_b = 0.433\left(\frac{\mu R_b^2 R}{\sigma t}\right)^{1/2} \tag{2-9}$$

Although the above models for the dimple deformation complement the limitation of Stefan-Reynolds model, they only focus on the film thickness in the center and at the barrier rim rather than the whole profile of the film.

2.3.2 Stokes–Reynolds–Young–Laplace (SRYL) model

The prototype of this model was developed by Chan et al.[43] and Bhatt et al.[44] at the same time. In this model, the flow in the thin film trapped between the two interfaces is considered in the lubrication approximation because the film thickness is small compared to the lateral dimension of the film. Thus, dynamic drainage of the liquid film is described by Reynolds lubrication theory under Stokes flow, which has been discussed above. Instead of assuming uniform film thickness in the film, the deformation of the bubble/droplet is described by non-equilibrium Young–Laplace equation.

The assumption in this model is that the deformation is determined by the balance between the hydrodynamic pressure ($p(r,t)$) due to the liquid flow in the film, disjoining pressure ($\Pi(h)$) attribute to the surface forces that distort the shape of the bubble/droplet and capillary forces that tend to minimize the interfacial area. In addition, it is assumed that the bubble/droplet can adjust its shape immediately to accommodate changes in hydrodynamic and disjoining pressures based on the constant interfacial tension[45].

The equilibrium deformation of a bubble/droplet can be obtained by minimizing the Helmholtz surface energy of the system[25, 46-47]. Therefore, the Young-Laplace equation for the equilibrium film shape is given by:

$$\frac{\sigma}{r}\frac{\partial}{\partial r}\left(\frac{rh_r}{(1+{h_r}^2)^{\frac{1}{2}}}\right)=\frac{2\sigma}{R}-\Pi(h) \tag{2-10}$$

where $h_r=\frac{\partial h}{\partial r}$, R is the radius of the bubble/droplet. However, to describe dynamic deformations for which the energy minimization would not strictly apply, the influence of hydrodynamic pressure should be considered. With the above assumption that the response time of the bubble/droplet due to capillary action is much faster than characteristic times in the variation of the hydrodynamic pressure, the effects of the hydrodynamic pressure can be added to the effects of equilibrium disjoining pressure arising from surface forces. Thus the Young-Laplace equation for the non-equilibrium film shape can be written as:

$$\frac{\sigma}{r}\frac{\partial}{\partial r}\left(\frac{rh_r}{(1+{h_r}^2)^{\frac{1}{2}}}\right)=\frac{2\sigma}{R}-\Pi(h)-p(r,t) \tag{2-11}$$

For deformable surfaces interacting with flat solid surfaces, the bubble/droplet interface is relatively flat on the scale of the bubble/droplet size within the interaction zone, which results in the approximation that $\frac{\partial h}{\partial r}\ll 1$. So eqn (2-11) can be linearized to give the spatial

film thickness as:

$$\frac{\sigma}{r}\frac{\partial}{\partial r}\left(r\frac{\partial h}{\partial r}\right) = \frac{2\sigma}{R} - \Pi(h) - p(r,t) \tag{2-12}$$

If hydrodynamic boundary conditions are specified as $u = 0$ at $z = 0$ and $z = h$, eqns (2-1) and (2-2) can be solved to describe the film drainage as:

$$\frac{\partial h(r,t)}{\partial t} = \frac{1}{12\mu r}\frac{\partial}{\partial r}\left(rh^3\frac{\partial p}{\partial r}\right) \tag{2-13}$$

Eqns (2-12) and (2-13) are two governing equations in this model that provide a complete description of the spatial and temporal evolution of the film. The numerical solutions of the Stokes–Reynolds–Young–Laplace equations with appropriate initial and boundary conditions predict all detailed information about the dynamic film drainage involving deformable surfaces.

The initial shape of the bubble/droplet is assumed to be quadratic with the initial film thickness of the form:

$$h(r,0) = h_0 + \frac{r^2}{2R} \tag{2-14}$$

Since we consider axisymmetric system here, the symmetry boundary condition applied at $r = 0$:

$$\frac{\partial h}{\partial r} = 0 = \frac{\partial p}{\partial r} \tag{2-15}$$

In order to solve the whole profile of the film, we have to choose a domain size of $r = r_{max}$ that is in the outside interaction zone. As r approaches to r_{max}, the film thickness increases with a quadratic dependence in r which leads to a pressure that decays like r^{-4}. This asymptotic pressure behavior can be implemented as the boundary condition at $r = r_{max}$:

$$r\left(\frac{\partial p}{\partial r}\right) + 4p = 0 \tag{2-16}$$

To model the dynamic drainage process, we need one more boundary condition that specifies how the bubble/droplet is moved. Considering the velocity of the bubble/droplet $\frac{dX(t)}{dt}$, the deflection of the cantilever and the deformation of the bubble/droplet, the final boundary condition at $r = r_{max}$ is given by:

$$\frac{\partial h(r_{max},t)}{\partial t} = \frac{dX(t)}{dt} + \frac{1}{K}\frac{dF(t)}{dt} - \frac{1}{2\pi\sigma}\frac{dF(t)}{dt}\left\{\log\left(\frac{r_{max}}{2R}\right) + B(\theta)\right\} \quad (2\text{-}17)$$

where K is the spring constant of the cantilever. With pinned three phase contact line:

$$B(\theta) = 1 + \frac{1}{2}\log\left(\frac{1+cos\theta}{1-cos\theta}\right) \quad (2\text{-}18)$$

With constant contact angle θ:

$$B(\theta) = 1 + \frac{1}{2}\log\left(\frac{1+cos\theta}{1-cos\theta}\right) - \left(\frac{1}{2+cos\theta}\right) \quad (2\text{-}19)$$

The Stokes–Reynolds equation mentioned above is based on tangentially immobile boundaries at the interface. For completeness, if the interfaces obey Navier slip boundary condition with different slip length b_0 at $z = 0$ and b_h at $z = h$, the Stokes–Reynolds equation will change to the following form:

$$\frac{\partial h(r,t)}{\partial t} = \frac{1}{12\mu r}\frac{\partial}{\partial r}\left(rh^3\frac{\partial p}{\partial r}\right) + \frac{1}{4\mu r}\frac{\partial}{\partial r}\left(r\frac{(b_0+b_h)h^3+b_0b_hh^2}{h+b_0+b_h}\frac{\partial p}{\partial r}\right) \quad (2\text{-}20)$$

The SRYL model has been widely applied to understand the dynamic behavior in different types of non-equilibrium experiments. The non-equilibrium force involving deformable surfaces has been measured by AFM and modelled by SRYL model. Once the SRYL model is shown to be able to accurately predict the time variations of the non-equilibrium forces, the model can be confidently used to infer the spatial and temporal evolutions of the shape of the film between interacting drops, bubbles and solids, which overcomes one of the limitations of AFM that the film profile cannot be observed directly. It has been proved that the SRYL model is capable of providing accurate quantitative prediction of non-

equilibrium forces measured by AFM between drops in different background solution[25, 28], bubbles/droplets and solids with different hydrodynamic conditions[22, 48], and bubbles with different collision modes[49]. It can also correctly predict the coalescence time between bubbles.

In addition, the experiments that measure the non-equilibrium shapes of drops and bubbles during drop–drop, bubble–solid and drop–solid interactions are studied by SRYL model as well. The predicted film profiles by SRYL model were all shown to be in good quantitative agreement with experiments of two glycerol drops in silicone oil[50], a bubble against a hydrophilic quartz plate in aqueous electrolyte solution[51] and a mercury drop against a mica plate[52]. Therefore, the SRYL model gives a consistent account of dynamic interactions involving deformable surfaces which includes surface forces, hydrodynamic effects and surface deformations in an internally consistent way.

To compare the SRYL model with the Stefan-Reynolds model, the time variation of the ratio of the volume of water in the film in the absence of a disjoining pressure, $V(t,0)$, to that in the presence of a repulsive disjoining pressure, $V(t,\Pi)$ was compared (Figure 2-8). The Stefan-Reynolds model assumes that the film is flat and non-deformable and predicts that the repulsive disjoining pressure retards the drainage rate. On the other hand, the SRYL model predicts that in the presence of a repulsive disjoining pressure, the film will drain faster. The reason for this is that the additional repulsion increases the thickness at the barrier rim of the film and facilitates the faster film drainage through this bottleneck. The observed trend of bubble-solid experiments is in agreement with SRYL model and opposite to that predicted by Stefan-Reynolds model, which verifies the status of SRYL model as a viable quantitative and predictive theory for the future.

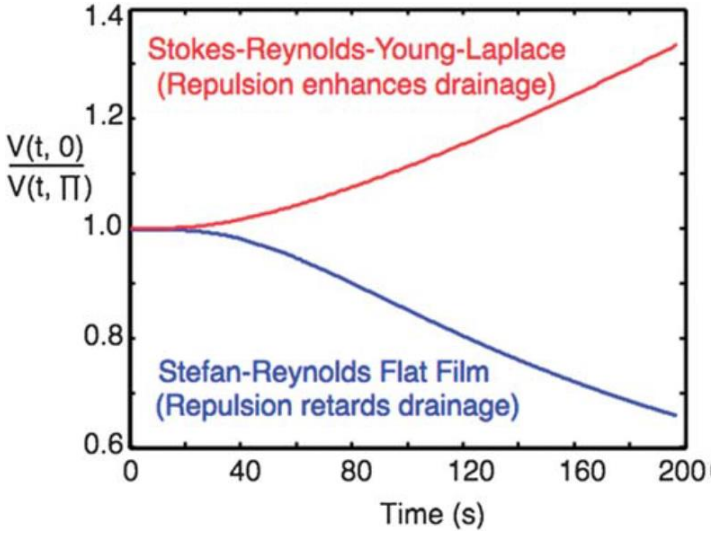

Figure 2-8. Comparison of relative changes in film volume with drainage time in the absence and presence of a repulsive disjoining pressure according to the SRYL model and the Stefan-Reynolds model[45].

2.4 Controversies

Although the dynamic drainage process of liquid films involving deformable surfaces has been studied for decades, some related questions are still under debate. In this section, two main controversial problems will be reviewed: the hydrodynamic boundary condition of liquid-solid interface and the origin of hydrophobic interaction.

2.4.1 Hydrodynamic boundary condition

When describing the film thinning process, the hydrodynamic boundary condition of the interface needs to be determined to choose the correct Stokes–Reynolds equation, from which the complete information of film drainage can be obtained. However, the hydrodynamic boundary condition of liquid-solid interface has been continuously studied since the beginning of the nineteenth century and remains elusive.

The main debate focuses on the no-slip and Navier slip boundary conditions. In the no-slip

boundary condition model, it assumes that the layer of liquid next to a solid surface moves with the same velocity as the surface and the velocity gradually varies when moving away from the surface into the fluid (Figure 2-9a). The physical origins of this boundary condition are believed to be the trapping of liquid in pockets on the solid surface and the attractive forces between the solid and liquid molecules. After investigation for almost two centuries, the no-slip boundary condition has been demonstrated by numerous macroscopic experiments and generally accepted for most continuum-based calculations[53]. Nevertheless, towards the end of last century, researchers began to cast doubt on the universality of the no-slip boundary condition and show that a liquid may slip on a solid surface under certain circumstances. Thus, the Navier slip model applied. In this model, the slip length, b, which is the distance beyond the liquid/solid interface at which the liquid velocity extrapolates to zero, is used to quantify the slip of a liquid at a solid interface (Figure 2-9b).

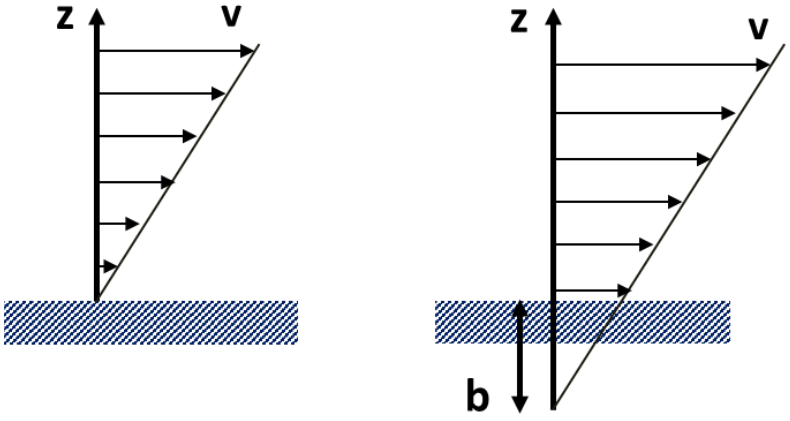

Figure 2-9. Schematic representation of (a) no-slip boundary condition and (b) slip boundary condition.

It is widely accepted that the no-slip boundary condition applied on hydrophilic surfaces so that the debate of slip boundary condition focuses on the hydrophobic surfaces. A high

contact angle is believed to be an indication of a weak interaction between liquid and solid that can be more easily overcome, causing the fluid molecules to slide across the solid surface. Thus, the surface wettability has a strong effect on the slip behavior. Many theoretical studies have confirmed the apparent slippage of liquid on poorly wetted surface[54-55]. For smooth surface, the slip length of more than 30 molecular diameters has been obtained by extensive molecular dynamics simulations[56]. However, this value is much smaller than those measured by physical experiments. The first direct experimental evidence of noticeable slip on the solid surface was conducted using total internal reflection – fluorescence recovery after photobleaching (TIR-FRAP). Slip length of the order of 400 nm were obtained for hexadecane on smooth lyophobic surfaces[57-58]. By using SFA, the slip length of glycerol on thiol surface was determined to be about 65 times the glycerol molecular size[59]. The slip length of water flow on hydrophobic surface has been mostly reported to be below 100 nm. Cottin-Bizonne et al.[60] has investigated the hydrodynamic boundary condition of water on smooth silanized glass surface using a dynamic surface force apparatus equipped with two independent sub-nanometer resolution sensor. The slip length was observed to be 20 nm by measuring the oscillating forces between two surfaces. AFM was also adapted to study the hydrodynamic boundary condition between two smooth hydrophobic surfaces by measuring the hydrodynamic forces. It was revealed that the partially boundary slip occurred on smooth hydrophobic surface and the slip length was found to be less than 20 nm[61]. Using particle image velocimetry combined with a nanopositioning system, the velocity profiles of water flow on smooth slianized glass surface were measured and the slip length was determined to be less than 100 nm[62]. Applying similar method, Lasne et al. reported a slip length of 45 nm on smooth

hydrophobic surface[63]. Nevertheless, Tretheway et al.[64] observed an apparent slip length as large as 1 μm for water flowing through a microchannel coated with a 2.3 nm thick monolayer of hydrophobic octadecyltrichlorosilane (OTS), which might arise from a depleted water region or vapor layer near a hydrophobic surface suggested by following work[65].

Since few surfaces are smooth on a molecular level, knowledge of the relationship between surface roughness and the degree of boundary slip is significant. The first experiment on how surface roughness influences the boundary slip was done by Zhu and Granick[66]. The surface roughness was varied systematically at nanometer level by collapsed polymers. They demonstrated that the degree of the boundary slip decreased as the surface roughness increased in the presence of polymer film. Bonaccurso et al. [67]showed completely different results when studying the influence of surface roughness on boundary slip using chemically etched silica surfaces that were completely water wettable. They found the boundary slip increased with increased surface roughness. These two studies were both focus on the surfaces with nano scale roughness. However, it is more complex and interesting to explore the hydrodynamic boundary condition on surfaces with micro scale roughness, especially patterned superhydrophobic surfaces. It is widely accepted that the structure of the superhydrophobic surface minimizes the liquid-solid contact area so that the liquid flows mainly over a layer of air. Thus, the enhanced liquid slippage on these kind of surfaces has been reported both experimentally[68-69] and theoretically[70-71] in recent years. The measured effective slip length varies in a wide range from a few microns[72] to tens and hundred microns[73-75] and was found to closely depend on the geometrical characteristics of the engineered superhydrophobic surfaces. The effective slip length usually has a linear

relationship with lateral roughness scale and disappears when the surface turns to Wenzel state. In general, the current experimental and theoretical studies use an isotropic slip length that is called effective slip length to represent the global slippage of superhydrophobic surface, which ignores the complicated nature of the surface. Recently, Schäffel et al.[76] performed a detailed measurement of local slip length for water on a microstructured superhydrophobic surface using fluorescence correlation spectroscopy. They showed that the local slip length has a finite, position-dependent, and anisotropic distribution. Therefore, the study of boundary slip at superhydrophobic surface needs to be more careful and systematical.

Besides the surface wettability and roughness, shear rate is another parameter that could has effect on liquid slippage. Its influence is still a controversial element under debate. The molecular dynamics simulations have seen a general nonlinear relationship between the amount of slip and the local shear rate at a solid surface[77]. The critical shear rate at which the slip length began to change was quite high that was hard to be achieved in a laboratory. However, the shear-dependent boundary slip has been observed in relatively low shear rate range in AFM experiments[61, 78]. The slip length of up to 20 nm was found to increase with increasing shear rate. Unlike previous results, Zhu et al.[79] presented an opposite shear-dependent slip that the slip length decreased with increasing shear rate. They attributed the previous findings of increasing slip with increased shear rate to an imprecise prediction of the variable drag force on the AFM cantilever. A large shear-dependent slip with a few microns was also measured by AFM[80]. A model motivated by the observation of nanobubbles on hydrophobic surface demonstrated that the air layer on the surface created the large shear-dependent slip by “leaking mattress” effect, where surface bubbles grow in

response to an oscillatory interaction by rectified diffusion[81].

2.4.2 Hydrophobic interaction

The hydrophobic interaction is a significant participant in many biological and colloidal systems. Although there is a great deal of study over past thirty years since the first direct measurement of the attraction between two nominally hydrophobic surfaces[82], no single theory can be used to account for all observed experimental behaviors.

The "intrinsic" hydrophobic interaction is believed to be due to the orientation of water molecules at hydrophobic surface. In order to minimize the contact area between water molecules and non-polar surfaces, water will specifically orient near the surface so that water configurational entropy increases[83], which leads to an attractive force between two approaching hydrophobic surfaces. This kind of hydrophobic interaction is commonly accepted as a very short range force with a decay length in the range of 0.3-1 nm that has been strongly verified[84-87]. The change of structure and viscosity of water confined in extended nanospace should also be considered when the studied system falls into nanoscale[88-89].

The hottest debate focuses on the existence and origin of "long-range" hydrophobic interaction. There are just few researchers who believe the existence of true "long-range" hydrophobic interaction. The Yoon group has published several works illustrating the presence of monotonic attractive forces between hydrophobic surfaces in pure water[90-92]. They reported strong and long-ranged hydrophobic interaction with a decay length up to 50 nm on thiolated gold and OTS coated silica surfaces. They demonstrated that the measured forces were functions of temperature and claimed that the long-ranged attractive forces resulted from structural changes of water molecules. They added the hydrophobic

interaction as an extra term to DLVO theory and combined hydrophobic interaction constants in the same manner as Hamaker constant.

On the other side, the "long-range" hydrophobic interaction was believed to be other existent forces that are mistaken for a hydrophobic force. One possible mechanism of the long range attraction is electrostatic charge or correlated dipole–dipole interactions. Tsao et al.[93] first measured the strong temperature-dependent long range hydrophobic interaction between hydrophobized mica surfaces absorbed by monolayer surfactants. They stated in a subsequent work that the long range attraction was due to the in-plane polarized domain of the monolayers[94]. Following their work, numerous experiments have been conducted to confirm this mechanism of long-range hydrophobic interaction[95-96]. Meyer et al.[97] investigated the interaction between a hydrophobized surface with double-chained surfactant absorption and a hydrophilic surface. The stronger and longer range hydrophobic interaction was measured than that of two hydrophobic surfaces. They claimed that the surface contain large micrometer-sized regions of positive charges and negative charges while remaining overall neutral, which resulted in electrostatic attraction when the two surfaces approach to each other. Another explanation of the long-range hydrophobic interaction is the separation induced cavitation. Christension et al.[98-99] measured the very long-range hydrophobic interaction with a decay length of 13-16 nm between uncharged hydrophobic surfaces. They speculated that the attractive interaction was caused by the vapor cavities on the surface. It has been witnessed recently in many literatures of forces measured between hydrophobic surfaces that nanobubbles play a central role in the observed forces, causing capillary type bringing between hydrophobized solid surfaces out to hundreds of nanometers[100-103]. Although the existence of nanobubbles on hydrophobic

surfaces has been visualized and probed by AFM imaging[104], Small-Angle X-ray Scattering (SAXS)[102], and Total Internal Reflection Fluorescence microscopy (TIRF)[105], the mechanism of the remarkable stability of such nanobubbles is still elusive. Several studies have purposefully generated nanobubbles on hydrophobic surfaces by solvent-exchange method to investigate the effect of nanobubbles on hydrophobic interaction. The increased amount of gas present on the surface has been found to increase the long-range attraction[106-107]. The degassing experiments confirmed and emphasized the role of nanobubbles and dissolved gas on long-range hydrophobic interactions[108-109].

In summary, the two controversies discussed above are the bone of contention for the past several decades and will be continuously debated in the future. More precise techniques are required to further refine our understanding of these vital and physical problems.

2.5 References

1. Ralston, J.; Fornasiero, D.; Hayes, R., Bubble-Particle Attachment and Detachment in Flotation. *Int J Miner Process* **1999**, *56*, 133-164.

2. Nguyen, A. V.; Ralston, J.; Schulze, H. J., On Modelling of Bubble-Particle Attachment Probability in Flotation. *Int J Miner Process* **1998**, *53*, 225-249.

3. Nonaka, M., A Waste-Water Treatment System Applying Aeration-Cavitation Flotation Mechanism. *Sep Sci Technol* **1986**, *21*, 457-474.

4. Chen, J.; Gomez, J. A.; Hoffner, K.; Barton, P. I.; Henson, M. A., Metabolic Modeling of Synthesis Gas Fermentation in Bubble Column Reactors. *Biotechnol Biofuels* **2015**, *8*, 89.

5. Chuang, E. Y.; Lin, K. J.; Lin, P. Y.; Chen, H. L.; Wey, S. P.; Mi, F. L.; Hsiao, H. C.;

Chen, C. T.; Sung, H. W., Self-Assembling Bubble Carriers for Oral Protein Delivery. *Biomaterials* **2015**, *64*, 115-124.

6. Derjaguin, B.; Kussakov, M., Anomalousproperties of Thin Polymolecular Films V. An Experimental Investigation of Polymolecular Solvate (Adsorbed) Films as Applied to the Development of a Mathematical Theory of the Stability of Colloids. *Acta Physicochim Urs* **1939**, *10*, 25-44.

7. Fisher, L. R.; Mitchell, E. E.; Hewitt, D.; Ralston, J.; Wolfe, J., The Drainage of a Thin Aqueous Film between a Solid-Surface and an Approaching Gas Bubble. *Colloids Surf* **1991**, *52*, 163-174.

8. Fisher, L. R.; Hewitt, D.; Mitchell, E. E.; Ralston, J.; Wolfe, J., The Drainage of an Aqueous Film between a Solid Plane and an Air Bubble. *Adv Colloid Interface Sci* **1992**, *39*, 397-416.

9. Hewitt, D.; Fornasiero, D.; Ralston, J.; Fisher, L. R., Aqueous Film Drainage at the Quartz Water Air Interface. *J Chem Soc Faraday T* **1993**, *89*, 817-822.

10. Platikanov, D., Experimental Investigation on Dimpling of Thin Liquid Films. *J Phys Chem-Us* **1964**, *68*, 3619-3624.

11. Nedyalkov, M.; Alexandrova, L.; Platikanov, D.; Levecke, B.; Tadros, T., Wetting Films on a Hydrophilic Silica Surface Obtained from Aqueous Solutions of Hydrophobically Modified Inulin Polymeric Surfactant. *Colloid Polym Sci* **2007**, *285*, 1713-1717.

12. Kolarov, T.; Zorin, Z.; Platikanov, D., Profile of the Transition Region between Aqueous Wetting Films on Quartz and the Adjacent Meniscus. *Colloids Surf* **1990**, *51*, 37-47.

13. Zorin, Z.; Platikanov, D.; Kolarov, T., The Transition Region between Aqueous Wetting Films on Quartz and the Adjacent Meniscus. *Colloids Surf* **1987**, *22*, 147-159.

14. Israelachvili, J., et al., Recent Advances in the Surface Forces Apparatus (SFA) Technique. *Rep Prog Phys* **2010**, *73*, 036601.

15. Connor, J. N.; Horn, R. G., The Influence of Surface Forces on Thin Film Drainage between a Fluid Drop and a Flat Solid. *Faraday Discuss* **2003**, *123*, 193-206.

16. Horn, R. G.; Asadullah, M.; Connor, J. N., Thin Film Drainage: Hydrodynamic and Disjoining Pressures Determined from Experimental Measurements of the Shape of a Fluid Drop Approaching a Solid Wall. *Langmuir* **2006**, *22*, 2610-2619.

17. Pushkarova, R. A.; Horn, R. G., Bubble-Solid Interactions in Water and Electrolyte Solutions. *Langmuir* **2008**, *24*, 8726-8734.

18. Ducker, W. A.; Senden, T. J.; Pashley, R. M., Direct Measurement of Colloidal Forces Using an Atomic Force Microscope. *Nature* **1991**, *353*, 239-241.

19. Ducker, W. A.; Xu, Z. G.; Israelachvili, J. N., Measurements of Hydrophobic and DLVO Forces in Bubble-Surface Interactions in Aqueous-Solutions. *Langmuir* **1994**, *10*, 3279-3289.

20. Butt, H. J., A Technique for Measuring the Force between a Colloidal Particle in Water and a Bubble. *J Colloid Interf Sci* **1994**, *166*, 109-117.

21. Vakarelski, I. U.; Lee, J.; Dagastine, R. R.; Chan, D. Y. C.; Stevens, G. W.; Grieser, F., Bubble Colloidal Afm Probes Formed from Ultrasonically Generated Bubbles. *Langmuir* **2008**, *24*, 603-605.

22. Manor, O.; Vakarelski, I. U.; Stevens, G. W.; Grieser, F.; Dagastine, R. R.; Chan, D. Y. C., Dynamic Forces between Bubbles and Surfaces and Hydrodynamic Boundary

Conditions. *Langmuir* **2008**, *24*, 11533-11543.

23. Manor, O.; Vakarelski, I. U.; Tang, X. S.; O'Shea, S. J.; Stevens, G. W.; Grieser, F.; Dagastine, R. R.; Chan, D. Y. C., Hydrodynamic Boundary Conditions and Dynamic Forces between Bubbles and Surfaces. *Phys Rev Lett* **2008**, *101*, 024501.

24. Tabor, R. F.; Manica, R.; Chan, D. Y. C.; Grieser, F.; Dagastine, R. R., Repulsive Van Der Waals Forces in Soft Matter: Why Bubbles Do Not Stick to Walls. *Phys Rev Lett* **2011**, *106*, 064501.

25. Dagastine, R. R.; Manica, R.; Carnie, S. L.; Chan, D. Y. C.; Stevens, G. W.; Grieser, F., Dynamic Forces between Two Deformable Oil Droplets in Water. *Science* **2006**, *313*, 210-213.

26. Tabor, R. F.; Chan, D. Y. C.; Grieser, F.; Dagastine, R. R., Anomalous Stability of Carbon Dioxide in PH-Controlled Bubble Coalescence. *Angew Chem Int Edit* **2011**, *50*, 3454-3456.

27. Browne, C.; Tabor, R. F.; Chan, D. Y. C.; Dagastine, R. R.; Ashokkumar, M.; Grieser, F., Bubble Coalescence During Acoustic Cavitation in Aqueous Electrolyte Solutions. *Langmuir* **2011**, *27*, 12025-12032.

28. Lockie, H. J.; Manica, R.; Stevens, G. W.; Grieser, F.; Chan, D. Y. C.; Dagastine, R. R., Precision Afm Measurements of Dynamic Interactions between Deformable Drops in Aqueous Surfactant and Surfactant-Free Solutions. *Langmuir* **2011**, *27*, 2676-2685.

29. Tabor, R. F.; Lockie, H.; Mair, D.; Manica, R.; Chan, D. Y. C.; Grieser, F.; Dagastine, R. R., Combined AFM-Confocal Microscopy of Oil Droplets: Absolute Separations and Forces in Nanofilms. *J Phys Chem Lett* **2011**, *2*, 961-965.

30. Shi, C.; Cui, X.; Xie, L.; Liu, Q. X.; Chan, D. Y. C.; Israelachvili, J. N.; Zeng, H.

B., Measuring Forces and Spatiotemporal Evolution of Thin Water Films between an Air Bubble and Solid Surfaces of Different Hydrophobicity. *Acs Nano* **2015**, *9*, 95-104.

31. Niecikowska, A.; Krasowska, M.; Ralston, J.; Malysa, K., Role of Surface Charge and Hydrophobicity in the Three-Phase Contact Formation and Wetting Film Stability under Dynamic Conditions. *J Phys Chem C* **2012**, *116*, 3071-3078.

32. Kosior, D.; Zawala, J.; Krasowska, M.; Malysa, K., Influence of N-Octanol and Alpha-Terpineol on Thin Film Stability and Bubble Attachment to Hydrophobic Surface. *Phys Chem Chem Phys* **2013**, *15*, 2586-2595.

33. Malysa, K.; Krasowska, M.; Krzan, M., Influence of Surface Active Substances on Bubble Motion and Collision with Various Interfaces. *Adv Colloid Interface Sci* **2005**, *114*, 205-225.

34. Parkinson, L.; Ralston, J., The Interaction between a Very Small Rising Bubble and a Hydrophilic Titania Surface. *J Phys Chem C* **2010**, *114*, 2273-2281.

35. Manica, R.; Parkinson, L.; Ralston, J.; Chan, D. Y. C., Interpreting the Dynamic Interaction between a Very Small Rising Bubble and a Hydrophilic Titania Surface. *J Phys Chem C* **2010**, *114*, 1942-1946.

36. Hendrix, M. H. W.; Manica, R.; Klaseboer, E.; Chan, D. Y. C.; Ohl, C. D., Spatiotemporal Evolution of Thin Liquid Films During Impact of Water Bubbles on Glass on a Micrometer to Nanometer Scale. *Phys Rev Lett* **2012**, *108*, 247803.

37. Wang, L. X.; Sharp, D.; Masliyah, J.; Xu, Z. H., Measurement of Interactions between Solid Particles, Liquid Droplets, and/or Gas Bubbles in a Liquid Using an Integrated Thin Film Drainage Apparatus. *Langmuir* **2013**, *29*, 3594-3603.

38. Krasowska, M.; Malysa, K., Wetting Films in Attachment of the Colliding Bubble.

Adv Colloid Interface Sci **2007**, *134-35*, 138-150.

39. Frankel, S. P.; Mysels, K. J., On Dimpling During Approach of Two Interfaces. *J Phys Chem-Us* **1962**, *66*, 190-191.

40. Hartland, S.; Robinson, J. D., Model for an Axisymmetric Dimpled Draining Film. *J Colloid Interf Sci* **1977**, *60*, 72-81.

41. Dimitrov, D. S.; Ivanov, I. B., Hydrodynamics of Thin Liquid-Films - Rate of Thinning of Microscopic Films with Deformable Interfaces. *J Colloid Interf Sci* **1978**, *64*, 97-106.

42. Jain, R. K.; Ivanov, I. B., Thinning and Rupture of Ring-Shaped Films. *J Chem Soc Farad T 2* **1980**, *76*, 250-266.

43. Chan, D. Y. C.; Dagastine, R. R.; White, L. R., Forces between a Rigid Probe Particle and a Liquid Interface - I. The Repulsive Case. *J Colloid Interf Sci* **2001**, *236*, 141-154.

44. Bhatt, D.; Newman, J.; Radke, C. J., Equilibrium Force Isotherms of a Deformable Bubble/Drop Interacting with a Solid Particle across a Thin Liquid Film. *Langmuir* **2001**, *17*, 116-130.

45. Chan, D. Y. C.; Klaseboer, E.; Manica, R., Film Drainage and Coalescence between Deformable Drops and Bubbles. *Soft Matter* **2011**, *7*, 2235-2264.

46. Chan, D. Y. C.; Klaseboer, E.; Manica, R., Theory of Non-Equilibrium Force Measurements Involving Deformable Drops and Bubbles. *Adv Colloid Interface Sci* **2011**, *165*, 70-90.

47. Carnie, S. L.; Chan, D. Y. C.; Lewis, C.; Manica, R.; Dagastine, R. R., Measurement of Dynamical Forces between Deformable Drops Using the Atomic Force Microscope. I.

Theory. *Langmuir* **2005**, *21*, 2912-2922.

48. Webber, G. B.; Manica, R.; Edwards, S. A.; Carnie, S. L.; Stevens, G. W.; Grieser, F.; Dagastine, R. R.; Chan, D. Y. C., Dynamic Forces between a Moving Particle and a Deformable Drop. *J Phys Chem C* **2008**, *112*, 567-574.

49. Vakarelski, I. U.; Manica, R.; Tang, X. S.; O'Shea, S. J.; Stevens, G. W.; Grieser, F.; Dagastine, R. R.; Chan, D. Y. C., Dynamic Interactions between Microbubbles in Water. *P Natl Acad Sci USA* **2010**, *107*, 11177-11182.

50. Chan, D. Y. C.; Klaseboer, E.; Manica, R., Dynamic Interactions between Deformable Drops in the Hele-Shaw Geometry. *Soft Matter* **2010**, *6*, 1809-1815.

51. Manica, R.; Chan, D. Y. C., Drainage of the Air-Water-Quartz Film: Experiments and Theory. *Phys Chem Chem Phys* **2011**, *13*, 1434-1439.

52. Manica, R.; Connor, J. N.; Carnie, S. L.; Horn, R. G.; Chan, D. Y. C., Dynamics of Interactions Involving Deformable Drops: Hydrodynamic Dimpling under Attractive and Repulsive Electrical Double Layer Interactions. *Langmuir* **2007**, *23*, 626-637.

53. Neto, C.; Evans, D. R.; Bonaccurso, E.; Butt, H. J.; Craig, V. S. J., Boundary Slip in Newtonian Liquids: A Review of Experimental Studies. *Rep Prog Phys* **2005**, *68*, 2859-2897.

54. Vinogradova, O. I., Drainage of a Thin Liquid-Film Confined between Hydrophobic Surfaces. *Langmuir* **1995**, *11*, 2213-2220.

55. Vinogradova, O. I., Slippage of Water over Hydrophobic Surfaces. *Int J Miner Process* **1999**, *56*, 31-60.

56. Barrat, J. L.; Bocquet, L., Large Slip Effect at a Nonwetting Fluid-Solid Interface. *Phys Rev Lett* **1999**, *82*, 4671-4674.

57. Pit, R.; Hervet, H.; Leger, L., Friction and Slip of a Simple Liquid at a Solid Surface. *Tribol Lett.* **1999**, *7*, 147-152.

58. Pit, R.; Hervet, H.; Leger, L., Direct Experimental Evidence of Slip in Hexadecane: Solid Interfaces. *Phys Rev Lett* **2000**, *85*, 980-983.

59. Baudry, J.; Charlaix, E.; Tonck, A.; Mazuyer, D., Experimental Evidence for a Large Slip Effect at a Nonwetting Fluid-Solid Interface. *Langmuir* **2001**, *17*, 5232-5236.

60. Cottin-Bizonne, C.; Cross, B.; Steinberger, A.; Charlaix, E., Boundary Slip on Smooth Hydrophobic Surfaces: Intrinsic Effects and Possible Artifacts. *Phys Rev Lett* **2005**, *94*, 056102.

61. Craig, V. S. J.; Neto, C.; Williams, D. R. M., Shear-Dependent Boundary Slip in an Aqueous Newtonian Liquid. *Phys Rev Lett* **2001**, *87*, 054504.

62. Joseph, P.; Tabeling, P., Direct Measurement of the Apparent Slip Length. *Phys Rev E* **2005**, *71*, 035303.

63. Lasne, D.; Maali, A.; Amarouchene, Y.; Cognet, L.; Lounis, B.; Kellay, H., Velocity Profiles of Water Flowing Past Solid Glass Surfaces Using Fluorescent Nanoparticles and Molecules as Velocity Probes. *Phys Rev Lett* **2008**, *100*, 214502.

64. Tretheway, D. C.; Meinhart, C. D., Apparent Fluid Slip at Hydrophobic Microchannel Walls. *Phys Fluids* **2002**, *14*, L9-L12.

65. Tretheway, D. C.; Meinhart, C. D., A Generating Mechanism for Apparent Fluid Slip in Hydrophobic Microchannels. *Phys Fluids* **2004**, *16*, 1509-1515.

66. Zhu, Y. X.; Granick, S., Limits of the Hydrodynamic No-Slip Boundary Condition. *Phys Rev Lett* **2002**, *88*, 106102.

67. Bonaccurso, E.; Butt, H. J.; Craig, V. S. J., Surface Roughness and Hydrodynamic

Boundary Slip of a Newtonian Fluid in a Completely Wetting System. *Phys Rev Lett* **2003**, *90*, 144501.

68. Choi, C. H.; Ulmanella, U.; Kim, J.; Ho, C. M.; Kim, C. J., Effective Slip and Friction Reduction in Nanograted Superhydrophobic Microchannels. *Phys Fluids* **2006**, *18*, 087105.

69. Lee, D. J.; Cho, K. Y.; Jang, S.; Song, Y. S.; Youn, J. R., Liquid Slip on a Nanostructured Surface. *Langmuir* **2012**, *28*, 10488-10494.

70. Cottin-Bizonne, C.; Barrat, J. L.; Bocquet, L.; Charlaix, E., Low-Friction Flows of Liquid at Nanopatterned Interfaces. *Nat Mater* **2003**, *2*, 237-240.

71. Ybert, C.; Barentin, C.; Cottin-Bizonne, C.; Joseph, P.; Bocquet, L., Achieving Large Slip with Superhydrophobic Surfaces: Scaling Laws for Generic Geometries. *Phys Fluids* **2007**, *19*, 123601.

72. Joseph, P.; Cottin-Bizonne, C.; Benoit, J. M.; Ybert, C.; Journet, C.; Tabeling, P.; Bocquet, L., Slippage of Water Past Superhydrophobic Carbon Nanotube Forests in Microchannels. *Phys Rev Lett* **2006**, *97*, 156104.

73. Choi, C. H.; Kim, C. J., Large Slip of Aqueous Liquid Flow over a Nanoengineered Superhydrophobic Surface. *Phys Rev Lett* **2006**, *96*, 066001.

74. Lee, C.; Choi, C. H.; Kim, C. J., Structured Surfaces for a Giant Liquid Slip. *Phys Rev Lett* **2008**, *101*, 064501.

75. Lee, C.; Kim, C. J., Influence of Surface Hierarchy of Superhydrophobic Surfaces on Liquid Slip. *Langmuir* **2011**, *27*, 4243-4248.

76. Schaffel, D.; Koynov, K.; Vollmer, D.; Butt, H. J.; Schonecker, C., Local Flow Field and Slip Length of Superhydrophobic Surfaces. *Phys Rev Lett* **2016**, *116*, 134501.

77. Thompson, P. A.; Troian, S. M., A General Boundary Condition for Liquid Flow at Solid Surfaces. *Nature* **1997**, *389*, 360-362.

78. Neto, C.; Craig, V. S. J.; Williams, D. R. M., Evidence of Shear-Dependent Boundary Slip in Newtonian Liquids. *Eur Phys J E* **2003**, *12*, S71-S74.

79. Zhu, L. W.; Neto, C.; Attard, P., Reliable Measurements of Interfacial Slip by Colloid Probe Atomic Force Microscopy. Iii. Shear-Rate-Dependent Slip. *Langmuir* **2012**, *28*, 3465-3473.

80. Zhu, Y. X.; Granick, S., Rate-Dependent Slip of Newtonian Liquid at Smooth Surfaces. *Phys Rev Lett* **2001**, *87*, 096105.

81. Lauga, E.; Brenner, M. P., Dynamic Mechanisms for Apparent Slip on Hydrophobic Surfaces. *Phys Rev E* **2004**, *70*, 026311.

82. Israelachvili, J.; Pashley, R., The Hydrophobic Interaction Is Long-Range, Decaying Exponentially with Distance. *Nature* **1982**, *300*, 341-342.

83. Djikaev, Y. S.; Ruckenstein, E., A Probabilistic Approach to the Effect of Hydrogen Bonding on the Hydrophobic Attraction. *J Chem Phys* **2009**, *130*, 124713.

84. Tabor, R. F.; Wu, C.; Grieser, F.; Dagastine, R. R.; Chan, D. Y. C., Measurement of the Hydrophobic Force in a Soft Matter System. *J Phys Chem Lett* **2013**, *4*, 3872-3877.

85. Kaggwa, G. B.; Nalam, P. C.; Kilpatrick, J. I.; Spencer, N. D.; Jarvis, S. P., Impact of Hydrophilic/Hydrophobic Surface Chemistry on Hydration Forces in the Absence of Confinement. *Langmuir* **2012**, *28*, 6589-6594.

86. Tabor, R. F.; Grieser, F.; Dagastine, R. R.; Chan, D. Y. C., The Hydrophobic Force: Measurements and Methods. *Phys Chem Chem Phys* **2014**, *16*, 18065-18075.

87. Shi, C.; Chan, D. Y. C.; Liu, Q. X.; Zeng, H. B., Probing the Hydrophobic

Interaction between Air Bubbles and Partially Hydrophobic Surfaces Using Atomic Force Microscopy. *J Phys Chem C* **2014**, *118*, 25000-25008.

88. Tsukahara, T.; Hibara, A.; Ikeda, Y.; Kitamori, T., NMR Study of Water Molecules Confined in Extended Nanospaces. *Angew Chem Int Edit* **2007**, *46*, 1180-1183.

89. Li, L. X.; Kazoe, Y.; Mawatari, K.; Sugii, Y.; Kitamori, T., Viscosity and Wetting Property of Water Confined in Extended Nanospace Simultaneously Measured from Highly-Pressurized Meniscus Motion. *J Phys Chem Lett* **2012**, *3*, 2447-2452.

90. Wang, J. L.; Yoon, R. H.; Eriksson, J. C., Excess Thermodynamic Properties of Thin Water Films Confined between Hydrophobized Gold Surfaces. *J Colloid Interf Sci* **2011**, *364*, 257-263.

91. Li, Z. L.; Yoon, R. H., Thermodynamics of Hydrophobic Interaction between Silica Surfaces Coated with Octadecyltrichlorosilane. *J Colloid Interf Sci* **2013**, *392*, 369-375.

92. Pan, L.; Jung, S.; Yoon, R. H., Effect of Hydrophobicity on the Stability of the Wetting Films of Water Formed on Gold Surfaces. *J Colloid Interf Sci* **2011**, *361*, 321-330.

93. Tsao, Y. H.; Yang, S. X.; Evans, D. F.; Wennerstrom, H., Interactions between Hydrophobic Surfaces - Dependence on Temperature and Alkyl Chain-Length. *Langmuir* **1991**, *7*, 3154-3159.

94. Tsao, Y. H.; Evans, D. F.; Wennerstrom, H., Long-Range Attractive Force between Hydrophobic Surfaces Observed by Atomic-Force Microscopy. *Science* **1993**, *262*, 547-550.

95. Rabinovich, Y. I.; Guzonas, D. A.; Yoon, R. H., Role of Chain Order in the Long-Range Attractive Force between Hydrophobic Surfaces. *Langmuir* **1993**, *9*, 1168-1170.

96. Miklavic, S. J.; Chan, D. Y. C.; White, L. R.; Healy, T. W., Double-Layer Forces

between Heterogeneous Charged Surfaces. *J Phys Chem-Us* **1994**, *98*, 9022-9032.

97. Meyer, E. E.; Lin, Q.; Hassenkam, T.; Oroudjev, E.; Israelachvili, J. N., Origin of the Long-Range Attraction between Surfactant-Coated Surfaces. *P Natl Acad Sci USA* **2005**, *102*, 6839-6842.

98. Christenson, H. K.; Claesson, P. M., Cavitation and the Interaction between Macroscopic Hydrophobic Surfaces. *Science* **1988**, *239*, 390-392.

99. Claesson, P. M.; Christenson, H. K., Very Long-Range Attractive Forces between Uncharged Hydrocarbon and Fluorocarbon Surfaces in Water. *J Phys Chem-Us* **1988**, *92*, 1650-1655.

100. Ishida, N.; Sakamoto, M.; Miyahara, M.; Higashitani, K., Attraction between Hydrophobic Surfaces with and without Gas Phase. *Langmuir* **2000**, *16*, 5681-5687.

101. Attard, P., Nanobubbles and the Hydrophobic Attraction. *Adv Colloid Interface Sci* **2003**, *104*, 75-91.

102. Palmer, L. A.; Cookson, D.; Lamb, R. N., The Relationship between Nanobubbles and the Hydrophobic Force. *Langmuir* **2011**, *27*, 144-147.

103. Hampton, M. A.; Nguyen, A. V., Nanobubbles and the Nanobubble Bridging Capillary Force. *Adv Colloid Interface Sci* **2010**, *154*, 30-55.

104. Ishida, N.; Inoue, T.; Miyahara, M.; Higashitani, K., Nano Bubbles on a Hydrophobic Surface in Water Observed by Tapping-Mode Atomic Force Microscopy. *Langmuir* **2000**, *16*, 6377-6380.

105. Chan, C. U.; Ohl, C. D., Total-Internal-Reflection-Fluorescence Microscopy for the Study of Nanobubble Dynamics. *Phys Rev Lett* **2012**, *109*, 174501.

106. Hampton, M. A.; Donose, B. C.; Nguyen, A. V., Effect of Alcohol-Water Exchange

and Surface Scanning on Nanobubbles and the Attraction between Hydrophobic Surfaces. *J Colloid Interf Sci* **2008**, *325*, 267-274.

107. Zhang, X. H.; Kumar, A.; Scales, P. J., Effects of Solvency and Interfacial Nanobubbles on Surface Forces and Bubble Attachment at Solid Surfaces. *Langmuir* **2011**, *27*, 2484-2491.

108. Zhang, X. H.; Zhang, X. D.; Lou, S. T.; Zhang, Z. X.; Sun, J. L.; Hu, J., Degassing and Temperature Effects on the Formation of Nanobubbles at the Mica/Water Interface. *Langmuir* **2004**, *20*, 3813-3815.

109. Ishida, N.; Kusaka, Y.; Ushijima, H., Hydrophobic Attraction between Silanated Silica Surfaces in the Absence of Bridging Bubbles. *Langmuir* **2012**, *28*, 13952-13959.

Chapter 3 Integrated thin liquid film force apparatus (ITLFFA)

3.1 Introduction

Interactions between deformable droplets or bubbles and rigid solid surfaces in an aqueous medium are of paramount importance as they are essential elements in the life sciences as well as diverse technologies such as mineral flotation[1-2], wastewater treatment[3], bioprocessing[4] and drug delivery[5]. An excellent control of interactions in these systems requires us to have a complete and deep understanding of the drainage dynamic and stability of thin liquid films through which two dispersed phases (bubbles/droplets and solids) interact with each other. Although the dynamic drainage process of liquid films has attracted a great deal of scientific interest since the first qualitative experimental investigation between an air bubble and a flat glass plate by Derjaguin and Kussakov[6], some related questions remain unexplained even after decades of systematic research.

Due to the intrinsic hydrophobic property of bubbles or oil droplets, interactions involving deformable surfaces are regarded as appropriate systems for studying hydrophobic interaction that affects the thermodynamic properties of common processes such as protein folding and the formation of micelles and cellular membranes[7]. Although quantitative force measurements of hydrophobic interactions have been conducted by atomic force microscope (AFM) and surface force apparatus (SFA)[8-10] for decades, the physical origin and nature of the hydrophobic interaction remain elusive. Moreover, interactions involving deformable surfaces further complicate the study of hydrophobic interaction because of the complex coupling of interaction forces and surface deformation. The hydrodynamic boundary condition of a liquid-solid interface is another unsolved critical fundamental question that has significant implications for controversial hydrophobic interaction. The slip boundary condition at the liquid-solid interface enables drag reduction of fluid flow on

solid surfaces, which may reduce fuel consumption for marine vessels and improve the efficiencies of diagnostic microchips, and membrane separation for water purification or desalination[11]. To date, however, the existence and degree of slip of liquid on solid surfaces remains a subject of controversy[12-13], especially for the hydrophobic surface[14-15]. When considering the interactions between deformable and solid surfaces, the hydrodynamic boundary condition of the liquid-solid interface is also revealed by the combination of forces and surface deformation. Therefore, to achieve deep understanding of the two fundamental questions concerning the nature of hydrophobic interaction and the hydrodynamic boundary condition of a liquid-solid interface, it is vital to realize simultaneous measurement of interaction forces and spatiotemporal film thickness during the dynamic drainage process. Currently, the AFM focuses mainly on direct force measurement between deformable and solid surfaces[16-17], while Scheludko cell[18-21], bubble expansion method[22-23], surface force apparatus (SFA)[24-25] and free rising bubble method[26-29] only quantify the film thickness of the confined liquid film. We note that AFM has been recently modified to perform the simultaneous measurement mentioned above[30], yet it has limitation on the investigation of hydrodynamic conditions. As the two interacting surfaces are in relative motion, hydrodynamic condition (e.g. the speed and trajectory of moving one of the surfaces) is one of the most important parameters affecting the dynamic drainage process between deformable and solid surfaces. Studying such interactions over a wide range of hydrodynamic conditions is highly preferred since it covers many practical problems in industrial processes and life sciences. In AFM, due to the narrow range of approach speed of the probe (up to about 100 μm/s of micron size probes)[31-33], the hydrodynamic condition is confined to relatively low Reynolds number regime that

characterizes the motion of the deformable surface ($<10^{-2}$). Similarly, hydrodynamic conditions covered by the experiments using the Scheludko cell, bubble expansion method and SFA are also within a low Reynolds number regime. At the other extreme, varying the size and hence the terminal velocity of the bubble in the order of cm/s in free rising bubble method leads to drainage dynamics of the thin aqueous film trapped in Reynolds number higher than 50. To the best of our knowledge, there remains a gap in studying thin liquid film drainage dynamics in systems of small to intermediate Reynolds number (10^{-2}-50) due to the inherent limitations of current techniques. This experimental gap has been partially filled by the integrated thin film drainage apparatus (ITFDA)[34] developed recently by our group. The ITFDA allows direct measurement of interaction forces under a wide range of bubble approach velocities while the advancing and receding contact angle is obtained simultaneously in a single experiment to link the measured force profiles to the wettability of solids. However, the fundamental coupling between interaction forces and spatiotemporal film thickness cannot be resolved by ITFDA[35].

Here we report a new instrument called integrated thin liquid film force apparatus (ITLFFA). Using a millimeter-size air bubble as a representative deformable surface, we demonstrate its capability of simultaneously: i) measure the time-dependent interaction forces; ii) determine the spatiotemporal film thickness (i.e. temporal bubble/droplet profiles); and iii) control the precise displacement of bubble/droplet over a wide range of velocities. For systems where adhesion occurs, the corresponding advancing and receding contact angles as well as the speed of contact line spreading can be measured to characterize the solid surfaces. This instrument could measure a few key physical parameters that link the measured results in a single experiment to provide scientific

insights/mechanisms without reconciling experimental results obtained using different instruments and/or from different laboratories, which is often extremely challenging by using current techniques.

3.2 Instrumentation

3.2.1 Instrument design

As illustrated in Figure 3-1, the ITLFFA consists of a stainless steel chamber placed on the stage of an inverted Axiovert 100 Carl Zeiss microscope. The chamber has two glass windows: one on the side for observation of size, motion and deformation of the bubble, and the other at the bottom allowing the simultaneous observation of interference fringes that is used for film thickness calculation. The interference fringes are recorded by a charge-coupled device (CCD) camera (20 fps) or high speed camera (Photron SA4, 60 fps～500000 fps) attached to the inverted microscope. For accurate control of the size and initial position of the bubble, a CCD camera (15 fps) mounted on the side records the approach and retract process of the bubble from which dynamic advancing and receding contact angles are determined. Inside the chamber, a transparent solid disc is attached at the free end of the bimorph enclosed by a fluorinated ethylene propylene (FEP) sheath. The bimorph is used to directly measure interaction forces between the bubble and the solid plate in a liquid medium of interest.

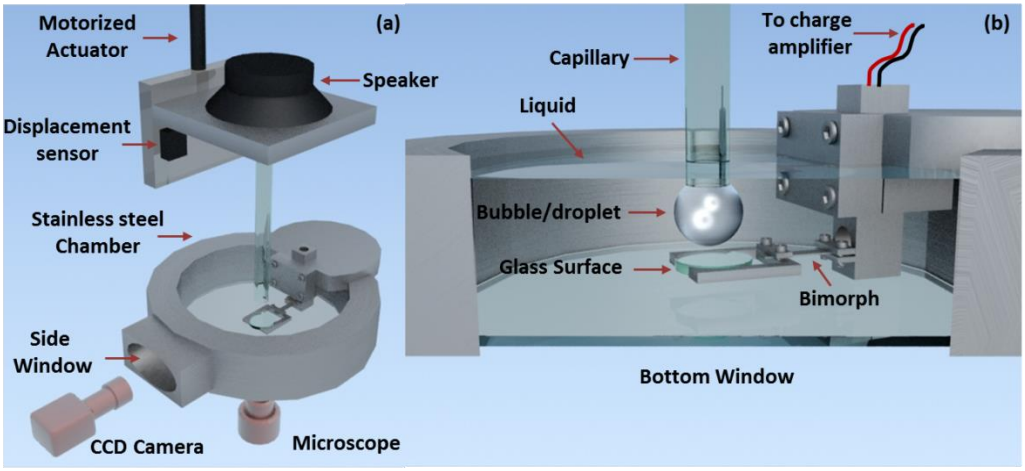

Figure 3-1. (a) Schematic illustration of the ITLFFA and (b) Enlarged image of stainless steel chamber filled with liquid.

Above the chamber is a driving system consisting of a speaker diaphragm, motorized actuator (THORLABS, Z825B), two displacement sensors, and a glass capillary with a micro-syringe for generation of a single bubble at the capillary orifice. The radius of the bubble was controlled by the gas-tight micro-syringe during the experiments, which can be observed by the camera on the side. The advantage of using the speaker diaphragm as one of driving mechanisms has been described in detail elsewhere[34]. The addition of a motorized actuator provides a more precise and slower displacement while allowing the bubble to be held stable at a desired position for a longer period of time without any drift. The speaker diaphragm and motorized actuator can be used independently to control the approach and retract velocity of the bubble, the range of the bubble displacement, and the duration of contact between the bubble and solid surface. Hence, various modes of motion can be achieved according to the experimental design. In addition, the displacement of the bubble can be independently tracked by the two displacement sensors with a sensitivity of 5 μm. This signal is highly valuable to obtain the real-time velocity of the bubble that is essential in the theoretical model, particularly when modeling the dynamic drainage

process under a relatively high bubble approach velocity. The combination of speaker diaphragm and motorized actuator covers a wide range of bubble displacement velocities from 2 μm/s to 50 mm/s. This is especially valuable for systematic study over a wide range of hydrodynamic conditions, which is not possible with any other current techniques.

3.2.2 Force measurement

The mechanism of measuring the force using the bimorph is the same as that in the ITFDA, which was explained previously[34]. The dimension of the bimorph is 20 mm × 3 mm × 0.3 mm (Fuji Ceramics Corp.) with a capacitance of 20 nF. The bimorph used here is a piezoelectric device which exhibits a reversible piezoelectric effect: the generation of electric charge in response to applied mechanical stress or vice visa. When a force (F) is applied on the free end of the bimorph, a deformation along the central axis at the end of bimorph (Figure 3-2), y is produced, which results in the generation of accumulated charge (Q) at the bimorph surface. The charge can be calculated by:

$$Q = \frac{3}{2} F \frac{L^2}{t^2} d_{13} \tag{3-1}$$

where d_{13} is the piezo material charge constant. The bimorph is considered as a cantilever beam. Therefore the applied force at the free end of the bimorph can be written as:

$$F = \frac{3EI}{L^3} y \tag{3-2}$$

where E and I are Young's Modulus and moment of inertia of the bimorph, respectively. According to eqn (3-2), the deformation of the bimorph is proportional to the applied force, leading to a linear relationship between the generated charge and the applied force. Hence, the applied force can be obtained by measuring the accumulated charge on the bimorph surface. The change of accumulated charge on the bimorph can be recorded by a high input impedance charge amplifier with different proportional gains. Several small pieces of

platinum wires with various weights were placed at the end of bimorph to calibrate the bimorph after each experiment. Figure 3-3a shows one example of the calibration results at the proportional gain of 125. The excellent linear relationship between the charge and the applied force verifies the mechanism of force measurement. The obtained slope that is referred as bimorph constant in Figure 3-3a can be used to convert the bimorph signal into interaction force. Since this constant is related to the clamp position, the calibration needs to be repeated once the bimorph is disassembled from the chamber.

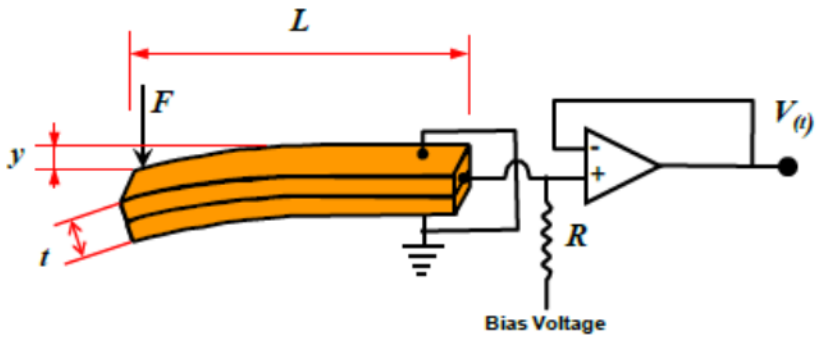

Figure 3-2. Schematic view of the bimorph and a high input impedance charge amplifier.

The spring constant of the bimorph was determined by applying known displacement on the free end of the bimorph. The relationship between the bimorph signal and displacement is shown in Figure 3-3b. The spring constant was 105 N/m at a proportional gain of 125 by using the obtained slope combined with the bimorph constant mentioned above.

The sensitivity of the bimorph depends on the used proportional gain. The charge range that the bimorph is able to measure is -8 to 8 V. Thus, the maximum force that the bimorph can measure varies with different proportional gains. For proportional gain of 125, the maximum measured force is about 465 μN. The appropriate proportional gain should be chosen for specific experiments.

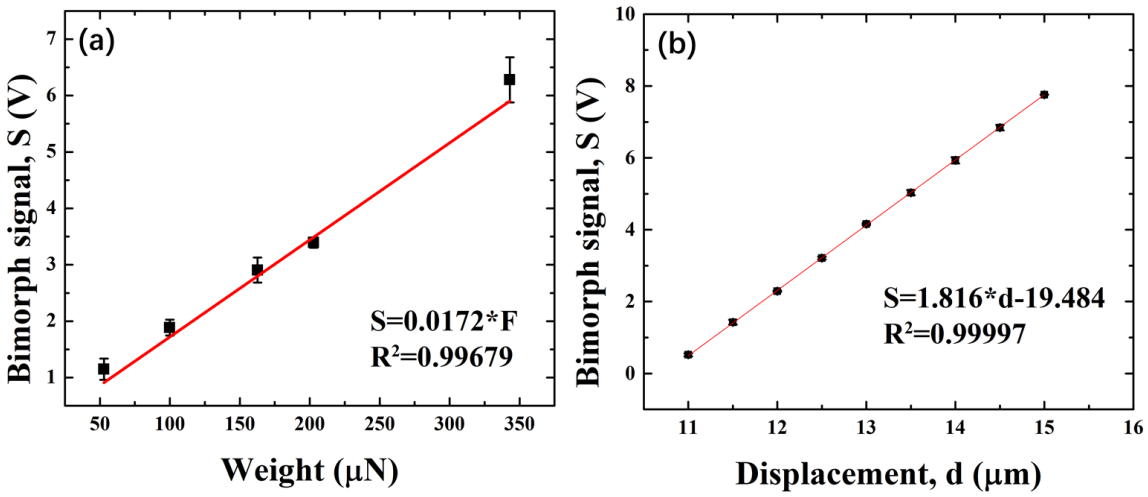

Figure 3-3. (a) Calibration of bimorph with proportional gain of 125. (b) Bimorph signal as a function of displacement.

3.2.3 Film thickness measurement

To acquire the film thickness and profile, videos of spatial and temporal interference fringes obtained by the high speed camera attached to the inverted microscope are analyzed frame by frame using a custom-written Matlab code. The time-dependent film thickness *h(r,t)* is calculated via the method adopted by Scheludko and Platikanov[36].

Figure 3-4 shows an example of how to convert the image of interference rings from the camera attached to the microscope to the film profile. For each experiment, two types of videos of interference rings were recorded separately with monochromatic interference band-pass filters (IF) with peak intensity at two wavelengths: λ=436 nm and 546 nm. From these two types of videos, the interference order of the equilibrium film was determined so that the absolute film thickness of the equilibrium film was known using the Dual-Wavelength technique[37]. Then we counted back to obtain the interference order at the rim of the film for the preceding images attained with monochromatic IF with peak intensity at 546 nm. With this method, the interference order of the ring at the barrier of the film in

Figure 3-4a is identified and the interference orders of other rings in the film are confirmed accordingly. The images were converted to grayscale intensity images and the intensity of film across one diameter (horizontal line in Figure 3-4a) was extracted through the Matlab code as shown in Figure 3-4b. With the interference order and intensity, the film thickness of each point across the horizontal line in Figure 3-4a could be calculated by the following equations:

$$h(r,t) = \frac{\lambda}{2\pi n_2}\left(\frac{2m+1}{2}\pi \pm arcsin\sqrt{\frac{\Delta}{1+4(1-\Delta)\frac{\sqrt{R_{12}R_{23}}}{\left(1-\sqrt{R_{12}R_{23}}\right)^2}}}\right) \tag{3-3}$$

$$\Delta = \frac{I(r,t)-I_{min}}{I_{max}-I_{min}} \tag{3-4}$$

$$R_{12} = \frac{(n_1-n_2)^2}{(n_1+n_2)^2} \text{ and } R_{23} = \frac{(n_2-n_3)^2}{(n_2+n_3)^2} \tag{3-5}$$

where $I(r,t)$ is the instantaneous light intensity, I_{max} and I_{min} are the maximum and minimum light intensity, respectively, λ is the wavelength of monochromatic light, m is the order of interference (m=0,1,2,…), n_1, n_2 and n_3 is the refractive index of the bubble, liquid and solid, respectively. The film profile was obtained as shown in Figure 3-4c.

By analyzing the image of other experimental times using the same procedure described above, the spatiotemporal evolution of the film profile during the whole drainage process can be attained. The interference rings were circular for the entire process indicating axisymmetric drainage of the thin liquid film.

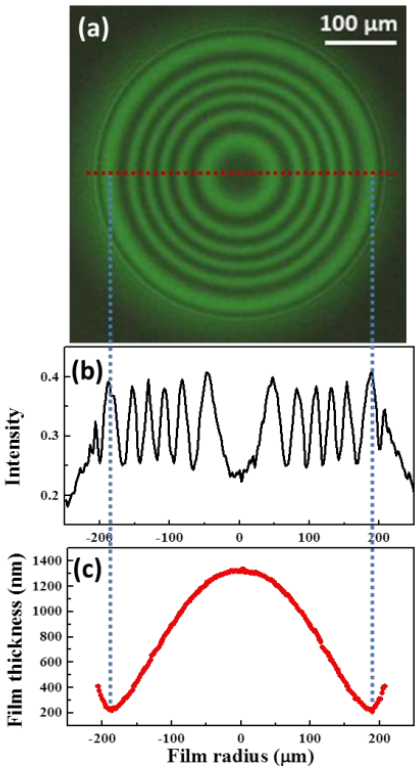

Figure 3-4. (a) An image of interference rings with IF that has a peak wavelength of 546 nm when a bubble interacts with a silica surface (contact angle~0^{o}) in Milli-Q water. (b) Instantaneous light intensity of the horizontal line in (a) as a function of film radius. (c) Corresponding film profile of (a).

3.2.4 Driving system

As mentioned above, the motorized actuator and the speaker diaphragm were used separately to drive the bubble approaching the solid surface. The maximum and minimum velocity of the motorized actuator is 2.3 mm/s and 2 µm/s, respectively. The maximum displacement of the motorized actuator is 25 mm. The setting parameters of the motorized actuator are displacement, acceleration and velocity. Since the motorized actuator needs some displacement to travel for acceleration and deceleration, one should make sure that the setting displacement is enough to reach the setting velocity. The minimum displacements for the motorized actuator to travel to reach the desired velocities are listed

in Table 3-1.

Table 3-1. Minimum displacements with corresponding velocity for motorized actuator.

Minimum displacement (mm)	Max velocity (mm/s)
0.1	0.62
0.2	0.90
0.3	1.13
0.4	1.30
0.5	1.48
0.6	1.62
0.7	1.72
0.8	1.81
0.9	1.94
1	2.08
1.1	2.22
1.2	2.29

For the speaker, the voltage is applied to drive the capillary to move. The applied voltages for the corresponding displacements are illustrated in Figure 3-5. The motion of the speaker can be regarded as uniform movement as the speaker needs little time to accelerate and

decelerate. The velocity of the speaker can go as high as 50 mm/s, which is faster than that of the motorized actuator.

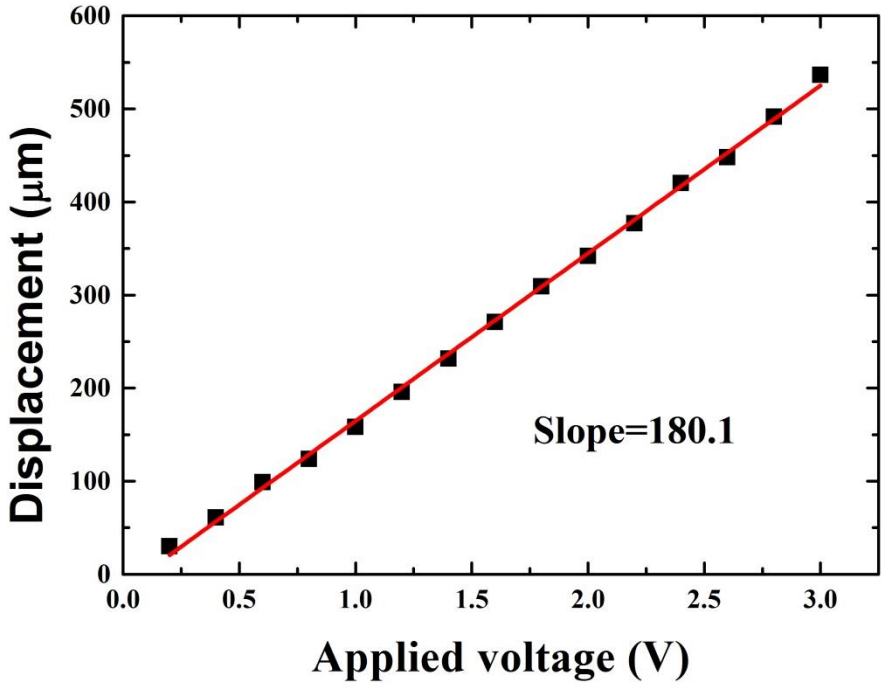

Figure 3-5. Applied voltage on the speaker with corresponding displacement.

The two displacement sensors in the driving system are used to track the real-time motion of the capillary. The signal of these displacement sensors are also voltage that needs to be converted to displacement. The calibration of the displacement sensor was conducted by moving motorized actuator with some displacement and recording the signal from the displacement sensor. As shown in Figure 3-6, the displacement sensor has the limitation for tracking the movement of the motorized actuator or speaker. It will exceed the measurement range of the displacement sensor if the total displacement is larger than 1.6 mm. The obtained slope is used to convert the signal into displacement.

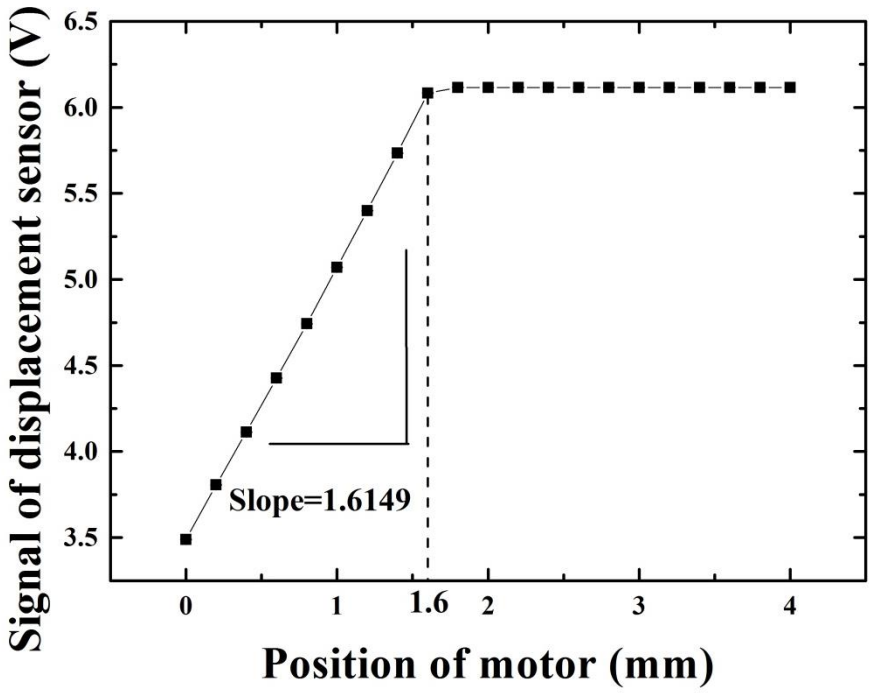

Figure 3-6. Calibration results of displacement sensor. The points are experimental data and the line is only for guiding the eye.

3.3 Operation and results

In a single cycle of measurement using the ITLFFA, the signals from the bimorph and displacement sensor are recorded as a function of time, while the entire moving process of the bubble and change of the interference fringes are recorded in real time by the two cameras described above. All signals and videos are synchronized through a user-developed program interfaced with LabVIEW 8.0. Processing the recorded data allows accurate determination of the force and spatiotemporal film thickness during the dynamic drainage process of the liquid film between the bubble and the solid surface.

3.3.1 Materials and method

The water used in the experiments was Milli-Q purified water with a resistivity of 18.2 MΩ cm at 25 ºC. Dimethyldichlorosilane (DMDCS, 99+%) was purchased from Acros

Organics. Heptane (HPLC grade) and sulfuric acid (ACS Plus) were supplied by Fisher Scientific. Hydrogen peroxide aqueous solution (30% w/w, ACS grade) was obtained from the Ricca Chemical Company. Anhydrous ethyl alcohol was acquired from Commercial Alcohols. All the chemicals mentioned above were used as received. The studied solid surfaces were 1 wave fused silica windows purchased from Edmund Optics. The diameter of the surfaces was 10 mm and the thickness was 1 mm. The capillary was obtained from Fisher Scientific with an inner diameter of 1.10±0.05 mm. One end of the capillary was smoothed by sand paper first and then heated with a butane flame to facilitate reproducible generation of bubbles. The capillary was cleaned with freshly prepared piranha solution (H_2SO_4 : H_2O_2= 3:1 by volume) for one hour and rinsed with Milli-Q water before using.

For preparing the hydrophilic surface, the received glass surface was soaked in freshly prepared piranha solution (H_2SO_4 : H_2O_2= 3:1 by volume) for one hour and rinsed with a large amount of Milli-Q water to eliminate any contamination. Consequently, the treated surface is completely water-wettable (contact angle ~0^o).

To hydrophobize the glass surface by silanation reaction, 0.824 mmol/L DMDCS in heptane solutions were prepared. The cleaned surfaces were immersed into 0.824 mmol/L DMDCS solution and then rinsed with heptane, anhydrous ethyl alcohol and water in sequence to remove the residual DMDCS. The smooth surface with designed hydrophobicity was successfully prepared after drying with nitrogen flow.

3.3.2 Hydrophilic surface

Examples of experimental data obtained when an air bubble with 1.2 mm radius approaches a hydrophilic fused silica surface at different velocities in Milli-Q water are shown in Figures 3-7 and 3-8. The initial separation between the bubble and solid surface was fixed

to 300 μm and the total displacement of the bubble was 400 μm. Thus, the film radius was controlled to be around 200 μm at the end of bubble displacement. Since ITLFFA provides a wide range of approach velocities, the results of two approach velocities with two orders of magnitude difference are compared here as an example. To better interpret the temporal film profiles of these two cases, the corresponding displacement signals of the capillary tube are plotted as a function of measurement time in Figures. 3-7B and 3-8B. By taking the derivative of these displacement signals with respect to the measurement time, bubble approach velocity profiles for the entire process are obtained as shown in Figures. 3-7C and 3-8C. The corresponding forces measured from the bimorph response are shown as black solid curves in Figures. 3-7D and 3-8D for these two drastically different approach velocities, respectively. The movement of the bubble includes the approaching and holding phases.

When the approach velocity was set to 1 mm/s (the corresponding Reynolds number is 2.7), the motion of the bubble and the dynamic drainage of the thin aqueous film in Figure. 3-7 can be described as follows:

(1) From 0 s to 0.330 s, the bubble began to move down towards the solid surface and reached the displacement of 300 μm set as the initial gap between the bubble and surface. During this period, the bubble went through an acceleration motion from 0 to 1 mm/s (Figure. 3-7B). In this region, the distance between the bubble and surface was so large that no interference fringes could be observed. Therefore, there is no information on the film profile in Figure. 3-7A during this period. Correspondingly, there is no measurable net interaction force acting upon the two surfaces, shown as a flat baseline with noise in Figure. 3-7D.

(2) The bubble started to deform at 0.330 s and reached the set displacement of 400 μm at 0.540 s. The velocity of the bubble decelerated from 1 mm/s to zero over this period. The evolution of the film profile is shown from curve *a* to curve *e* in Figure. 3-7A. At the beginning of this period, the bubble became slightly flattened. After profile *a*, a dimple appeared and became increasingly more pronounced as the bubble further approached the solid surface, accompanied by a gradual increase in film radius. Once the dimple formed, the film thickness at the barrier rim decreased continuously while the film thickness at the center increased slightly. This phenomenon was caused by the rapid movement of the bubble in such a way that the drainage of the liquid in the center of the film could not catch up with the rapid movement of the bubble. As a result, the film thickness at the center increased from 1900 nm to 2100 nm as the barrier rim became thinner towards the solid surface. This "central bounce" was also observed by Connor and Horn[25] when they studied the interactions between a mercury droplet and a mica surface in aqueous electrolyte solutions. At the same time, a repulsive force was detected at profile *a*, represented by the positive bimorph response in Figure. 3-7D. The repulsive force continued to increase until profile *e*, which was caused by increasing film radius during the movement of the bubble.

(3) The bubble stopped moving at 0.540 s and was held at this position. Although the movement of the bubble ended at the beginning of this period, the liquid film continued to drain as shown from profiles *e-i* in Figure. 3-7A. As seen in profile *e*, the thickness in the center of the film kept increasing to 2200 nm when the bubble stopped moving. After profile *e*, the film thickness decreased monotonically at both the center and barrier rim. Eventually at 97.67 s (profile *i*), the liquid film at the center and barrier rim met together to produce a flat equilibrium film with the thickness of 115±2 nm, which matches the value

calculated by DLVO theory (see Appendix A). Although the film profile kept changing during this period, the net interaction force remained constant around 15 μN, shown as a horizontal line with noise in Figure. 3-7D. During the holding period, thermal fluctuation resulted in a slight change in the film radius.

For the bubble approach velocity set at 0.01 mm/s (the corresponding Reynolds number is 0.027), the evolution of the liquid film profile (Figure. 3-8A) was significantly different from that shown in Figure. 3-7A corresponding to the bubble approach velocity set at 1 mm/s. The bubble became flattened with a very small dimple after 33.883 s (profile *j* in Figure. 3-8A), when the bubble was still moving with a constant velocity of 0.01 mm/s. In this case, the difference in the film thickness between the center and the barrier rim was only 10 nm. As the bubble continued moving towards the solid surface, the film radius increased continuously, accompanied by a continuous decrease in the film thickness across the entire film. After the bubble stopped moving at 46.150 s (profile *o*), the entire flat (parallel) liquid film continued to drain to a stable equilibrium film thickness of 112±2 nm at 61.150 s (profile *p*). Considering the experimental error, this equilibrium film thickness can be regarded the same as that in the case of 1 mm/s approach velocity, indicating that the equilibrium film thickness is independent of approach velocity. A gradual increment of repulsive force was also detected during the movement of the bubble. When the bubble stopped moving, the repulsive force reached a maximum of about 15 μN and remained almost constant for the holding period.

The effect of bubble approach velocity on the film drainage process shown in Figures 3-7 and 3-8 can be summarized as follows: (1) Film thickness at the first occurrence of dimple formation is highly dependent on bubble approach velocity. The dimple formation

happened at the film thickness around 2000 nm when the bubble approach velocity was set to 1 mm/s, while it appeared at about 200 nm when the approach velocity decreased to 0.01 mm/s. (2) The film profile exhibited more pronounced dimple that the difference of film thickness between the center and barrier rim could be as great as 1500 nm when the approach velocity was set at 1 mm/s. The formation of a dimple is due to the hydrodynamic pressure that becomes larger than the internal pressure of the bubble that inverts the curvature of the bubble surface and makes it locally concave[38]. The more pronounced dimple at high bubble approach velocity indicates a higher hydrodynamic pressure inside the film. The theoretical model that could explain how the bubble approach velocity influences the drainage of the intervening liquid film between bubbles and solid surfaces over a wide range of approach velocities will be discussed in more detail in next chapter.

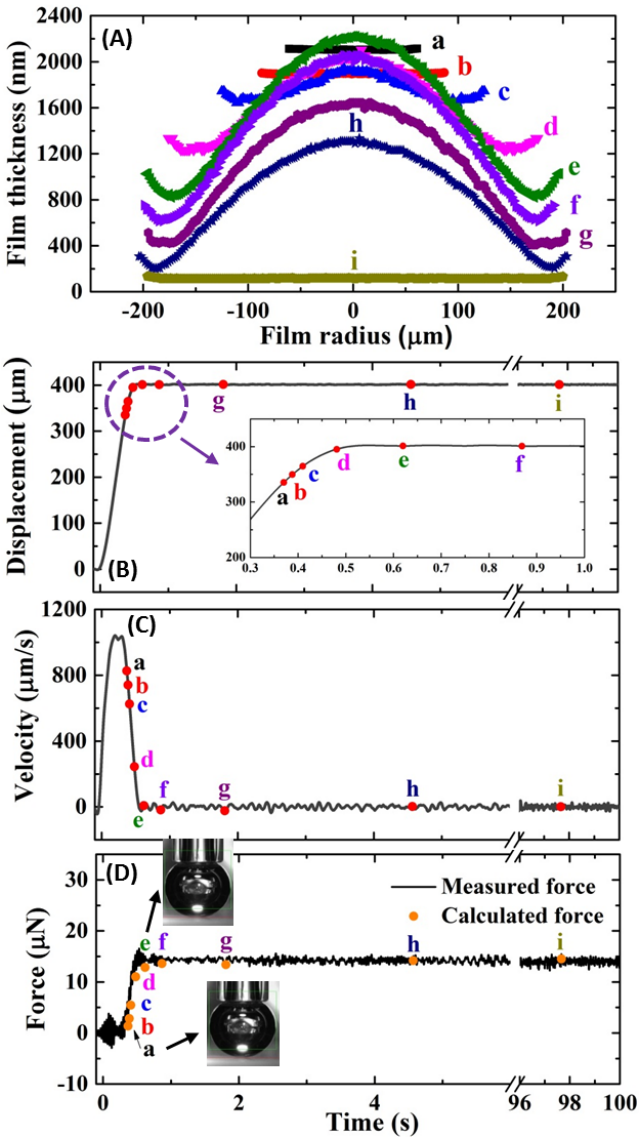

Figure 3-7. Experimentally measured film profiles (A) and corresponding displacement signal (B), velocity profile (C) and force profile (solid curve in D) for an air bubble interacting with a hydrophilic silica surface in Milli-Q water. The approach velocity was set to 1 mm/s. The measurement time of profiles *a*, *b*, *c*, *d*, *e*, *f*, *g*, *h* and *i* was 0.370 s, 0.388 s, 0.410 s, 0.481 s, 0.620 s, 0.869 s, 1.809 s, 4.567 s and 97.67 s, respectively, corresponding to the points in (B) and (C). The points on the force profile (D) were calculated forces by integrating the measured film profiles in (A). Images inserted in (D) are side views of the bubble at points *a* and *e* on the force profile.

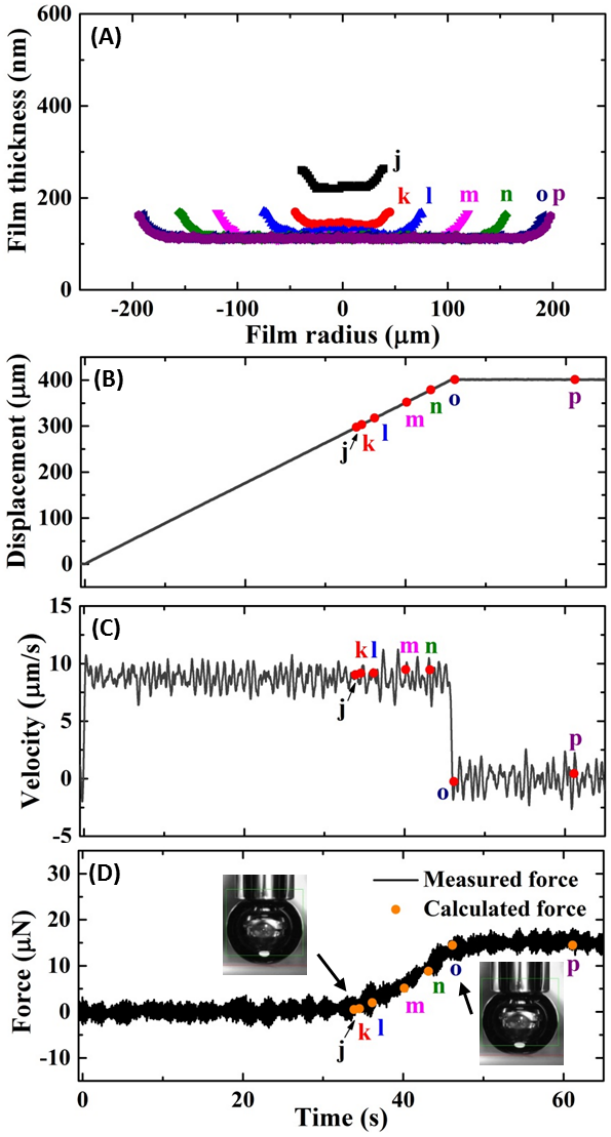

Figure 3-8. Evolution of film profile (A) between an air bubble and a hydrophilic silica surface in Milli-Q water at the bubble approach velocity of 0.01 mm/s. The corresponding measurement time of profiles *j*, *k*, *l*, *m*, *n*, *o* and *p* were 33.883 s, 34.533 s, 36.150 s, 40.150 s, 43.150 s, 46.150 s and 61.150 s, respectively. The displacement signal (B), velocity profile (C) and typical force profile (solid curve in D) as a function of measurement time were obtained simultaneously, along with the film profile. The points on the force profile were calculated by integrating the film profiles in (A). Still images of the bubble at *j* and *o* of force profile are from the side view.

3.3.3 Hydrophobic surface

The ITLFFA not only has the ability to measure the drainage process that produces stable film with a hydrophilic surface, but, with the help of high speed camera, it is also capable of providing dynamic information when a bubble interacts with a partially hydrophobic surface. The evolution of the film profile and force curve of a bubble (with 1.2 mm radius) approaching a partially hydrophobic surface (water contact angle = 62.5°) in Milli-Q water at an approach velocity of 1 mm/s is shown in Figure 3-9. The initial gap and total displacement are 300 μm and 400 μm, respectively, which are the same as in the case of hydrophilic surface. The movement of the bubble in this experiment had three phases: approaching phase, holding phase and retracting phase. During approaching, the bubble began to deform at 0.33 s and produced a small flat film at 0.3565 s as shown by profile *a* in Figure 3-9A, resulting in the detection of a repulsive force at point A in Figure 3-9B. A dimple appeared at a film thickness around 980 nm (profile *b*), which was much thinner compared to the hydrophilic case (Figure 3-7). The film drained from profiles *b* to *g*, accompanied by a gradual increase in film radius, which in turn caused a continuous increase in the repulsive interaction force. Since the bubble was moving so fast that the liquid inside the film did not have sufficient time to drain out, the thickness of the center film stayed around 900 nm as the thickness of the barrier rim continued to decrease, forming a more pronounced dimple.

The bubble stopped moving at 0.53 s. After profile *h*, the thickness of both the center of the film and barrier rim started to decrease without a change in film radius, leading to a constant repulsive force of 15 μN. Right after 0.6 s (profile *i*), only 70 ms after the bubble stopped moving, the film ruptured at one point of the barrier rim, creating a three phase

contact (TPC) line which expanded and displaced the liquid that was in the film resulting in an adhesion between the bubble and surface. In this case, the solid surface was pulled up to the bubble surface, shown as a large attractive force of 94.9 μN (point C in Figure 3-9B). The bubble was held from points C to D with constant interaction force.

As the bubble retracted from the hydrophobic surface at point D, the TPC line pinned on the surface initially until it reached the receding contact angle. Then the TPC line began to slide on the surface, exhibiting a gradual increase in the attractive force. The attractive force reached a maximum of 205.5 μN at point E and decreased as the bubble continued to retract. After detachment of the bubble from the solid surface at point F, the bimorph response returned to zero, representing no net interaction force as anticipated. Compared to the results of hydrophilic surface with the same approach velocity of 1 mm/s (Figure 3-7), the surface hydrophobicity is clearly playing an essential role in determining the film thickness of the first dimple and the shape of the film. The significant impact of surface hydrophobicity on the thickness of the dimple formation and the shape of the bubbles at a given bubble approach velocity suggests the change in hydrodynamic boundary condition of the liquid/solid interface by changing surface wettability, which remains a subject of controversy[15, 39].

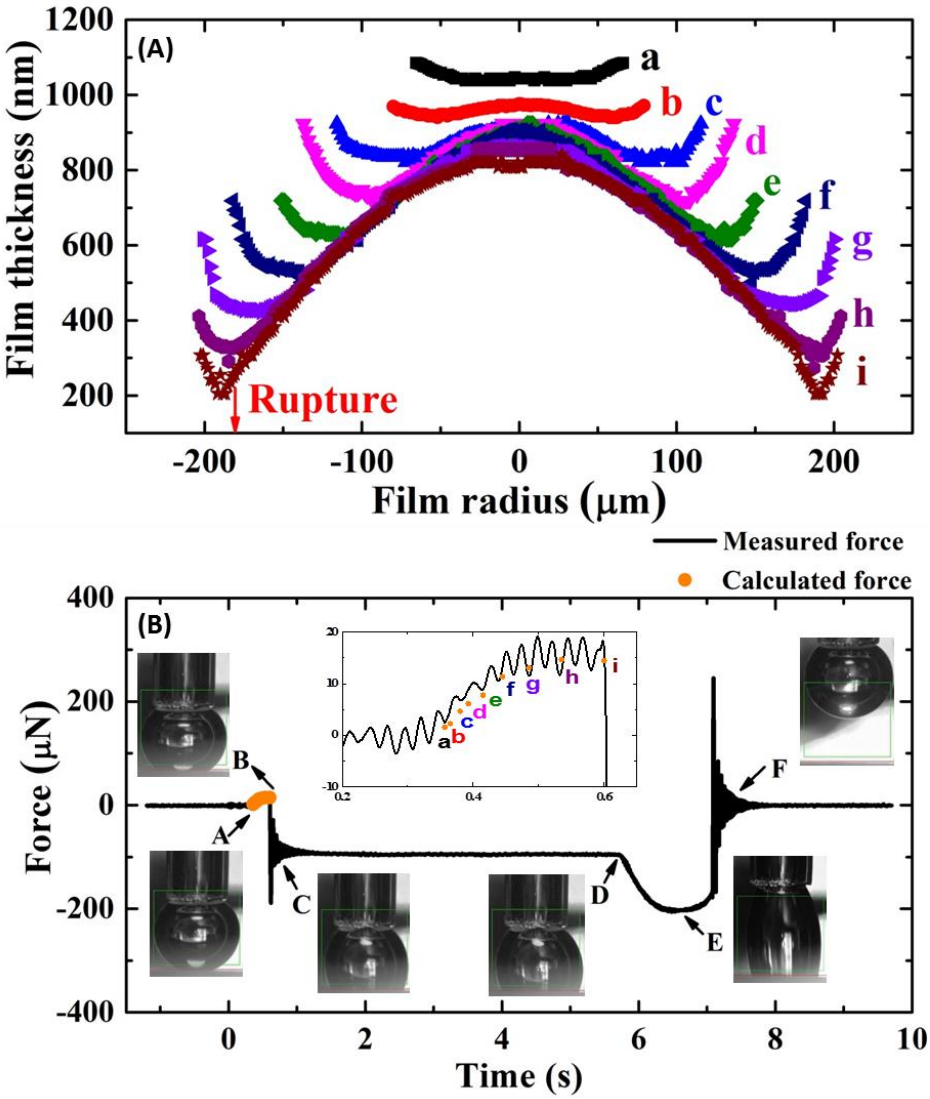

Figure 3-9. Evolution of film profile (A) and force curve (B) during interaction between an air bubble and a surface with a water contact angle of 62.5° in Milli-Q water. The approach velocity was set to 1 mm/s. The experimental time of profiles *a*, *b*, *c*, *d*, *e*, *f*, *g*, *h* and *i* were 0.3565 s, 0.365 s, 0.3800 s, 0.3925 s, 0.4150 s, 0.4450 s, 0.4850 s, 0.5350 s and 0.6000 s, respectively. The inset in (B) is the enlarged force curve between point A and point B. The still images at various locations in (B) are obtained from the side camera to help interpret the force curve.

3.4 Validation of instrument feasibility

Due to the accurate determination of spatiotemporal film thickness by the ITLFFA, the net interaction force could be extracted from the measured film profile. To check the accuracy of the synchronous measurement of dynamic forces and spatiotemporal film thickness by the ITLFFA, the interaction force was calculated from the spatiotemporal film profiles and the results were compared with the forces measured directly by the bimorph.

Inspired by the pioneering work of Horn et al.[38, 40], the interaction force was calculated on the basis of the measured film profile using a simple model as follows: The deformation of the bubble is well known to be the result of the total film pressure (p) acting on the air-liquid interface. When an axisymmetric bubble of constant surface tension (γ), approaches a flat solid surface, the augmented Young–Laplace equation can relate the pressure difference across the curved air-liquid interface to the interfacial tension and film shape by[41]:

$$\frac{\gamma}{r}\frac{\partial}{\partial r}\left(\frac{rh_r}{(1+{h_r}^2)^{\frac{1}{2}}}\right) = \frac{2\gamma}{R_0} - p(r,t) \tag{3-6}$$

where $h_r = \frac{\partial h}{\partial r}$, h is the time dependent film thickness, r is the film radius, and R_0 is the radius of the bubble when it is not distorted by any interaction with other surfaces. Within the interaction zone, the bubble shape is relatively flat such that the deformation of bubble is small (typically in nanometers) compared to the scale of bubble size (millimeters). As a result, the approximation of $\frac{\partial h}{\partial r} \ll 1$ applies and the augmented Young–Laplace equation (eqn (3-6)) is linearized as:

$$\frac{\gamma}{r}\frac{\partial}{\partial r}\left(r\frac{\partial h}{\partial r}\right) = \gamma\left(\frac{1}{r}\frac{\partial h}{\partial r} + \frac{\partial^2 h}{\partial r^2}\right) = \frac{2\gamma}{R_0} - p(r,t) \tag{3-7}$$

This expression is used to calculate total pressure in the film $p(r,t)$ on the basis of the first and second derivatives of measured film profile at each time step. In our experiments, the surface tension of the bubble in an aqueous solution was 72 mN/m and the radius of the undisturbed bubble (R_0) was 1.2 mm. Therefore, the pressure inside the bubble ($\frac{2\gamma}{R_0}$) was 120 Pa. Since finding derivatives by directly taking differences between serial data points results in large scatter, the fifth-ordered Savitzky-Golay function[42] was adopted to smooth the raw profile data to achieve the first derivative. The Savitzky-Golay method performs a local polynomial regression around each point and is therefore superior to the simple adjacent averaging because it preserves features of the original data. Then the first derivative was further smoothed by the same function to get the second derivative. The large number of raw data points in the film profile guaranteed the reliability of this method. As a result, the total pressure in the film as a function of *r* can be obtained using eqn 3-7 for each time (An example of calculating total pressure from the film profile is given in Appendix A). The total interaction force was calculated by taking the integral of total pressure in the film with respect to *r*:

$$\mathrm{F(t)} = 2\pi \int_0^\infty p(r,t)\mathrm{rdr} \tag{3-8}$$

In practice, it is impossible to integrate from 0 to infinity as the film thickness far from the interaction zone cannot be measured. Since the disjoining pressure and hydrodynamic pressure are negligible outside the interaction zone, in our data processing, the upper limit of the integral was set to 20 μm beyond the barrier rim of the film to represent the total interaction force. This approximation was sufficient as the difference by extending the integration further was negligible.

The integrated forces from each film profile at a specific time of the same experiments in

Figure 3-7A and 3-8A are shown as dots in Figure 3-7D and 3-8D, respectively. The excellent agreement between the integrated and measured force proves the feasibility of using the ITLFFA for the synchronous measurement of film profile and the corresponding interaction force.

The same comparison between the measured force and calculated force based on the film profile was also carried out when the bubble interacts with partially hydrophobic surface before film rupture. The integrated interaction force from each profile of Figure 3-9A is represented as dots in the inserted graph in Figure 3-9B. Before the film became unstable and ruptured, the integrated force agreed well with the measured repulsive force, proving that the measured film profile is a valid indicator of the interaction force. The accurate comparison in both cases indicates the feasibility of detecting weak forces by using the bubble deformation as a force sensor, with the sensitivity of nN being adjustable by changing the surface tension of the liquids and the extent of deformation. More importantly, although the interaction force as a function of separation distance involving deformable surfaces has been measured using other techniques such as AFM[9, 43-44], our results show that it is not accurate to use one separation distance to represent the film thickness across the entire film, since the film thickness is not uniform across the whole profile (See example of quantification of different approaches in Ref 41). As a result, it is necessary to state the location of film thickness when plotting the relationship between interaction forces and separation distance in studying dynamic thin film drainage involving deformable surfaces.

The ITLFFA can also precisely calculate the capillary force in the TPC region (point C to point F) by the geometric properties of the interface obtained from the side camera using

the method described in a previous paper[34] and compared with the forces measured directly by the bimorph force sensor, which can be linked to the dynamic advancing and receding contact angles measured in the same system.

The capillary force, F_C, which is the main contribution to the adhesion force between the bubble and solid surface after TPC can be calculated by

$$F_c = \pi r_c^2 \cdot \Delta P - 2\pi r_c \gamma sin\theta \tag{3-9}$$

where r_c is the radius of contact area, γ is the interfacial tension of liquid-air interface, θ is the contact angle of the bubble on the flat surface, measured through the aqueous solution. The determination of contact angle is illustrated in Figure 3-10. ΔP is the Laplace pressure which can be calculated according to the toroidal approximation as:

$$\Delta P = \gamma \cdot (\frac{1}{R} + \frac{1}{l}) \tag{3-10}$$

Where R and l are the principal radii of the capillary bridge and can be determined using the vision analysis program (Figure 3-10). The good agreement between the calculated and measured capillary force is shown in Figure 3-10.

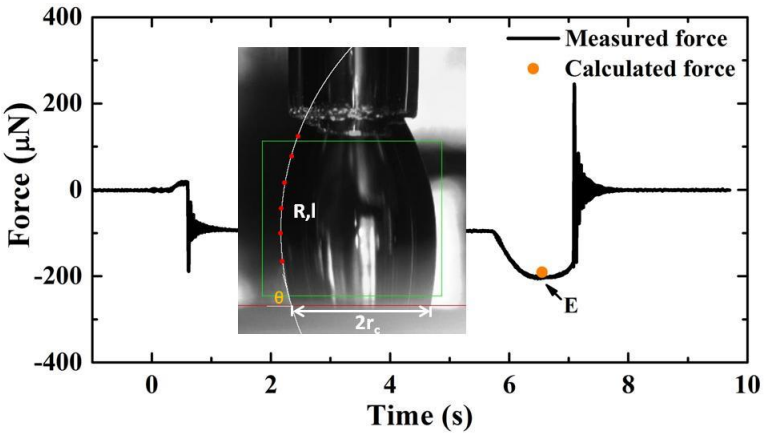

Figure 3-10. Schematic diagram of imaging analysis to determine contact angle to calculate capillary force and its comparison with measured force.

3.5 Conclusions

In this work, we developed the device ITLFFA that allows experimental measurements over a wide range of hydrodynamic conditions that is not available using current techniques. It performs the simultaneous measurement of dynamic forces and spatiotemporal film thickness during thin liquid film drainage between deformable and solid surfaces. The comparison of the integrated force extracted from the measured film profile with that measured directly by the bimorph sensor supported the self-consistent quantitative study of dynamic thin liquid film drainage process by the ITLFFA. It also presents the potential to extend the dynamic interaction measurement to a variety of complex systems of scientific and practical importance.

Furthermore, our data indicate that the high approach velocity of deformable surface and low surface hydrophobicity results in the formation of a more pronounced dimple and larger film thickness at the appearance of the first dimple. These results point to the importance of a systematic study of the effect of approach velocity and surface hydrophobicity on the drainage dynamics of thin liquid films, which appealed us to consider them as crucial parameters in a theoretical model that may shed light on the nature of the hydrophobic interaction.

3.6 References

1. Ralston, J.; Fornasiero, D.; Hayes, R., Bubble-Particle Attachment and Detachment in Flotation. *Int J Miner Process* **1999**, *56*, 133-164.

2. Nguyen, A. V.; Ralston, J.; Schulze, H. J., On Modelling of Bubble-Particle Attachment Probability in Flotation. *Int J Miner Process* **1998**, *53*, 225-249.

3. Nonaka, M., A Waste-Water Treatment System Applying Aeration-Cavitation Flotation Mechanism. *Sep Sci Technol* **1986**, *21*, 457-474.

4. Chen, J.; Gomez, J. A.; Hoeffner, K.; Barton, P. I.; Henson, M. A., Metabolic Modeling of Synthesis Gas Fermentation in Bubble Column Reactors. *Biotechnol Biofuels* **2015**, *8*, 89.

5. Chuang, E. Y.; Lin, K. J.; Lin, P. Y.; Chen, H. L.; Wey, S. P.; Mi, F. L.; Hsiao, H. C.; Chen, C. T.; Sung, H. W., Self-Assembling Bubble Carriers for Oral Protein Delivery. *Biomaterials* **2015**, *64*, 115-124.

6. Derjaguin, B.; Kussakov, M., Anomalousproperties of Thin Polymolecular Films V. An Experimental Investigation of Polymolecular Solvate (Adsorbed) Films as Applied to the Development of a Mathematical Theory of the Stability of Colloids. *Acta Physicochim Urs* **1939**, *10*, 25-44.

7. Tabor, R. F.; Grieser, F.; Dagastine, R. R.; Chan, D. Y. C., The Hydrophobic Force: Measurements and Methods. *Phys Chem Chem Phys* **2014**, *16*, 18065-18075.

8. Israelachvili, J.; Pashley, R., The Hydrophobic Interaction Is Long-Range, Decaying Exponentially with Distance. *Nature* **1982**, *300*, 341-342.

9. Ducker, W. A.; Xu, Z. G.; Israelachvili, J. N., Measurements of Hydrophobic and Dlvo Forces in Bubble-Surface Interactions in Aqueous-Solutions. *Langmuir* **1994**, *10*, 3279-3289.

10. Mastropietro, D. J.; Ducker, W. A., Forces between Hydrophobic Solids in Concentrated Aqueous Salt Solution. *Phys Rev Lett* **2012**, *108*, 106101.

11. Majumder, M.; Chopra, N.; Andrews, R.; Hinds, B. J., Nanoscale Hydrodynamics: Enhanced Flow in Carbon Nanotubes. *Nature* **2005**, *438*, 930-930.

12. Bonaccurso, E.; Kappl, M.; Butt, H. J., Hydrodynamic Force Measurements: Boundary Slip of Water on Hydrophilic Surfaces and Electrokinetic Effects. *Phys Rev Lett* **2002**, *88*, 076103.

13. Ho, T. A.; Papavassiliou, D. V.; Lee, L. L.; Striolo, A., Liquid Water Can Slip on a Hydrophilic Surface. *P Natl Acad Sci USA* **2011**, *108*, 16170-16175.

14. Schaeffel, D.; Yordanov, S.; Schmelzeisen, M.; Yamamoto, T.; Kappl, M.; Schmitz, R.; Duenweg, B.; Butt, H.-J.; Koynov, K., Hydrodynamic Boundary Condition of Water on Hydrophobic Surfaces. *Phys Rev E* **2013**, *87*, 051001.

15. Cottin-Bizonne, C.; Cross, B.; Steinberger, A.; Charlaix, E., Boundary Slip on Smooth Hydrophobic Surfaces: Intrinsic Effects and Possible Artifacts. *Phys Rev Lett* **2005**, *94*, 056102.

16. Manor, O.; Vakarelski, I. U.; Stevens, G. W.; Grieser, F.; Dagastine, R. R.; Chan, D. Y. C., Dynamic Forces between Bubbles and Surfaces and Hydrodynamic Boundary Conditions. *Langmuir* **2008**, *24*, 11533-11543.

17. Manor, O.; Vakarelski, I. U.; Tang, X.; O'Shea, S. J.; Stevens, G. W.; Grieser, F.; Dagastine, R. R.; Chan, D. Y. C., Hydrodynamic Boundary Conditions and Dynamic Forces between Bubbles and Surfaces. *Phys Rev Lett* **2008**, *101*, 024501.

18. Platikanov, D., Experimental Investigation on Dimpling of Thin Liquid Films. *J Phys Chem-Us* **1964**, *68*, 3619-3624.

19. Platikanov, D.; Exerowa, D., Thin Liquid Films. In *Fundamentals of Interface and Colloid Science, Vol 5: Soft Colloids*, 2005.

20. Nedyalkov, M.; Alexandrova, L.; Platikanov, D.; Levecke, B.; Tadros, T., Wetting Films on a Hydrophilic Silica Surface Obtained from Aqueous Solutions of

Hydrophobically Modified Inulin Polymeric Surfactant. *Colloid Polym Sci* **2007**, *285*, 1713-1717.

21. Pan, L.; Jung, S.; Yoon, R. H., Effect of Hydrophobicity on the Stability of the Wetting Films of Water Formed on Gold Surfaces. *J Colloid Interf Sci* **2011**, *361*, 321-330.

22. Fisher, L. R.; Mitchell, E. E.; Hewitt, D.; Ralston, J.; Wolfe, J., The Drainage of a Thin Aqueous Film between a Solid-Surface and an Approaching Gas Bubble. *Colloids Surf* **1991**, *52*, 163-174.

23. Hewitt, D.; Fornasiero, D.; Ralston, J.; Fisher, L. R., Aqueous Film Drainage at the Quartz Water Air Interface. *J Chem Soc Faraday T* **1993**, *89*, 817-822.

24. Pushkarova, R. A.; Horn, R. G., Bubble-Solid Interactions in Water and Electrolyte Solutions. *Langmuir* **2008**, *24*, 8726-8734.

25. Connor, J. N.; Horn, R. G., The Influence of Surface Forces on Thin Film Drainage between a Fluid Drop and a Flat Solid. *Faraday Discuss* **2003**, *123*, 193-206.

26. Manica, R.; Klaseboer, E.; Chan, D. Y. C., The Hydrodynamics of Bubble Rise and Impact with Solid Surfaces. *Adv Colloid Interface Sci* **2016**, *235*, 214-232.

27. Hendrix, M. H. W.; Manica, R.; Klaseboer, E.; Chan, D. Y. C.; Ohl, C.-D., Spatiotemporal Evolution of Thin Liquid Films During Impact of Water Bubbles on Glass on a Micrometer to Nanometer Scale. *Phys Rev Lett* **2012**, *108*, 247803.

28. Manica, R.; Klaseboer, E.; Chan, D. Y. C., Force Balance Model for Bubble Rise, Impact, and Bounce from Solid Surfaces. *Langmuir* **2015**, *31*, 6763-6772.

29. Tsao, H. K.; Koch, D. L., Observations of High Reynolds Number Bubbles Interacting with a Rigid Wall. *Phys Fluids* **1997**, *9*, 44-56.

30. Shi, C.; Cui, X.; Xie, L.; Liu, Q. X.; Chan, D. Y. C.; Israelachvili, J. N.; Zeng, H.

B., Measuring Forces and Spatiotemporal Evolution of Thin Water Films between an Air Bubble and Solid Surfaces of Different Hydrophobicity. *Acs Nano* **2015**, *9*, 95-104.

31. Lockie, H. J.; Manica, R.; Stevens, G. W.; Grieser, F.; Chan, D. Y. C.; Dagastine, R. R., Precision AFM Measurements of Dynamic Interactions between Deformable Drops in Aqueous Surfactant and Surfactant-Free Solutions. *Langmuir* **2011**, *27*, 2676-2685.

32. Vakarelski, I. U.; Manica, R.; Tang, X.; O'Shea, S. J.; Stevens, G. W.; Grieser, F.; Dagastine, R. R.; Chan, D. Y. C., Dynamic Interactions between Microbubbles in Water. *P Natl Acad Sci USA* **2010**, *107*, 11177-11182.

33. Dagastine, R. R.; Manica, R.; Carnie, S. L.; Chan, D. Y. C.; Stevens, G. W.; Grieser, F., Dynamic Forces between Two Deformable Oil Droplets in Water. *Science* **2006**, *313*, 210-213.

34. Wang, L. X.; Sharp, D.; Masliyah, J.; Xu, Z. H., Measurement of Interactions between Solid Particles, Liquid Droplets, and/or Gas Bubbles in a Liquid Using an Integrated Thin Film Drainage Apparatus. *Langmuir* **2013**, *29*, 3594-3603.

35. Shahalami, M.; Wang, L.; Wu, C.; Masliyah, J. H.; Xu, Z.; Chan, D. Y. C., Measurement and Modeling on Hydrodynamic Forces and Deformation of an Air Bubble Approaching a Solid Sphere in Liquids. *Adv Colloid Interface Sci* **2015**, *217*, 31-42.

36. Scheludko, A.; Platikanowa, D., Untersuchung Dunner Flussiger Schichten Auf Quecksilber. *Kolloid Z Z Polym* **1961**, *175*, 150-158.

37. Schilling, J.; Sengupta, K.; Goennenwein, S.; Bausch, A. R.; Sackmann, E., Absolute Interfacial Distance Measurements by Dual-Wavelength Reflection Interference Contrast Microscopy. *Phys Rev E* **2004**, *69*, 021901.

38. Horn, R. G.; Asadullah, M.; Connor, J. N., Thin Film Drainage: Hydrodynamic and

Disjoining Pressures Determined from Experimental Measurements of the Shape of a Fluid Drop Approaching a Solid Wall. *Langmuir* **2006**, *22*, 2610-2619.

39. Vinogradova, O. I.; Koynov, K.; Best, A.; Feuillebois, F., Direct Measurements of Hydrophobic Slippage Using Double-Focus Fluorescence Cross-Correlation. *Phys Rev Lett* **2009**, *102*, 118302.

40. Pushkarova, R. A.; Horn, R. G., Surface Forces Measured between an Air Bubble and a Solid Surface in Water. *Colloid Surface A* **2005**, *261*, 147-152.

41. Chan, D. Y. C.; Klaseboer, E.; Manica, R., Film Drainage and Coalescence between Deformable Drops and Bubbles. *Soft Matter* **2011**, *7*, 2235-2264.

42. Savitzky, A.; Golay, M. J. E., Smoothing and Differentiation of Data by Simplified Least Squares Procedures. *Anal Chem* **1964**, *36*, 1627-1639.

43. Preuss, M.; Butt, H. J., Direct Measurement of Particle-Bubble Interactions in Aqueous Electrolyte: Dependence on Surfactant. *Langmuir* **1998**, *14*, 3164-3174.

44. Bonaccurso, E.; Kappl, M.; Butt, H.-J., Thin Liquid Films Studied by Atomic Force Microscopy. *Curr Opin Colloid Interface Sci* **2008**, *13*, 107-119.

Chapter 4 Study of interactions between air-bubble and hydrophilic flat solid surface using an integrated thin liquid film force apparatus (ITLFFA)

4.1 Introduction

Understanding the dynamic and velocity-dependent interactions between an air bubble and a solid surface is of great importance in fundamental scientific problems, which are of interest to many industrial processes, such as mineral flotation[1-3], foam formation[4], micro- and nano-fluidic engineering[5-6] and biomedical engineering[7-9]. To properly predict and manipulate these processes, the nature of liquid film drainage that influences the interaction must be completely studied. Such drainage process depends critically on the relative velocity of the moving bubble and solid surface. At different velocities, the hydrodynamic condition in the thin liquid film between the bubble and the solid surface provides a major contribution to the interfacial deformation of the bubble and determines the magnitude of the interaction force. However, quantification of the interaction between an air bubble and a solid surface over a wide range of velocities remains elusive.

Over the past few years, the atomic force microscope (AFM) has been widely deployed to make direct measurement of the interaction forces between deformable and solid surfaces by colloidal probe technique. In the initial studies, the typical velocity of the colloidal probe was less than 1 μm/s corresponding to equilibrium force measurement[10-13]. Recently, there have been a number of reports measuring non-equilibrium, velocity-dependent dynamic force between drops[14-16], bubbles[17-18] and between a bubble and a solid surface[19-22] using AFM. In these studies, the velocity of the probe is in the range of 1-50 μm/s. Also, a modified AFM that allows simultaneous measurement of dynamic force and spatiotemporal film thickness provides probe velocity up to 30 μm/s[23-24]. In these non-equilibrium studies, the radius of the bubble or drop is within 100 μm, resulting in small deformation of the bubble or drop. Combining with the narrow range of probe velocity, the

hydrodynamic condition falls in the regime of very low Reynolds number ($Re = 2\rho RV/\mu$ <10^{-2}, where R is the bubble/drop radius, V is the approach velocity of the bubble/drop, ρ and μ are the density and dynamic viscosity of water, respectively). The Cantilevered-Capillary Force Apparatus[25] was developed to measure interaction forces for particles ranging in size from 10 μm to 1 mm in diameter. Due to the low velocity that was less than 100 μm/s, it still falls in the low Reynolds number regime. For the measurement of spatiotemporal film thickness, prior experiments were performed by Derjaguin & Kussakov[26] and Fisher et al.[27] using bubble expansion method without controlling the velocity of bubble. The surface force apparatus (SFA)[28-29] and Scheludko cell[30-31] were also used to measure spatiotemporal film thickness during the drainage process within a low Reynolds number regime restricting quantitative velocity-dependent investigation.

On the other hand, measurements in the regime of Re>50 have been conducted by the rising bubble method through controlling the size and the terminal velocity of the bubble[32]. Generally, the velocity of the bubble is in the order of cm/s. The influence of the impact velocity of a bubble colliding with solid and air-liquid interface has been studied by Malysa et al.[33-34]. It was shown that higher impact velocity led to larger deformation of the bubble and increased the coalescence time from the results of bubble trajectory and bouncing, but the information of liquid film drainage was not provided. With the use of interferometry technique, the spatiotemporal evolution of the thin liquid film during impact of bubble on various surfaces has been further studied experimentally and theoretically[32, 35-36]. However, there are still limited measurements of coupling the interaction force with spatiotemporal film thickness.

The current techniques mentioned above allow the measurements of dynamic film drainage under low Reynolds number (Re <10^{-2}) and high Reynolds number (Re >50) regime. Therefore, an intermediate regime between them remains to be explored. Although the integrated thin film drainage apparatus (ITFDA)[37] previously developed by our group has addressed this problem, it only measures the interaction force without spatiotemporal film thickness. The recently reported integrated thin liquid film force apparatus (ITLFFA)[38] not only bridges the knowledge gap in the field of dynamic film drainage between two surfaces, but also provides the coupling of dynamic force and spatiotemporal film thickness and covers bubble displacement velocity in the intermediate range from 2 μm/s to 50 mm/s. Here, we use the ITLFFA to do systematic study and gain insights of the interaction between a bubble and a hydrophilic surface at different salt concentrations over a wide range of hydrodynamic conditions over four orders of magnitude. The global Reynolds number varies from 0.027 to 37.75 by controlling the bubble displacement velocity from 0.01 mm/s to 14 mm/s while other parameters are kept constant and controlled accurately.

4.2 Experimental section

4.2.1 Materials

The water used in the experiments was Milli-Q purified water with a resistivity of 18.2 MΩ cm at 25 ºC and the viscosity (μ) is 0.89 mPa·s. Sulfuric acid (ACS Plus) was supplied by Fisher Scientific. Hydrogen peroxide aqueous solution (30% w/w, ACS grade) was obtained by Ricca Chemical Company. All the chemicals mentioned above were used as received. Potassium chloride (KCl) of ACS grade, purchased from Fisher Scientific was

recrystallized and then calcined in an oven at 550 ºC for 8 h to remove any impurities. The studied solid surfaces were 1λ fused silica windows purchased from Edmund Optics.

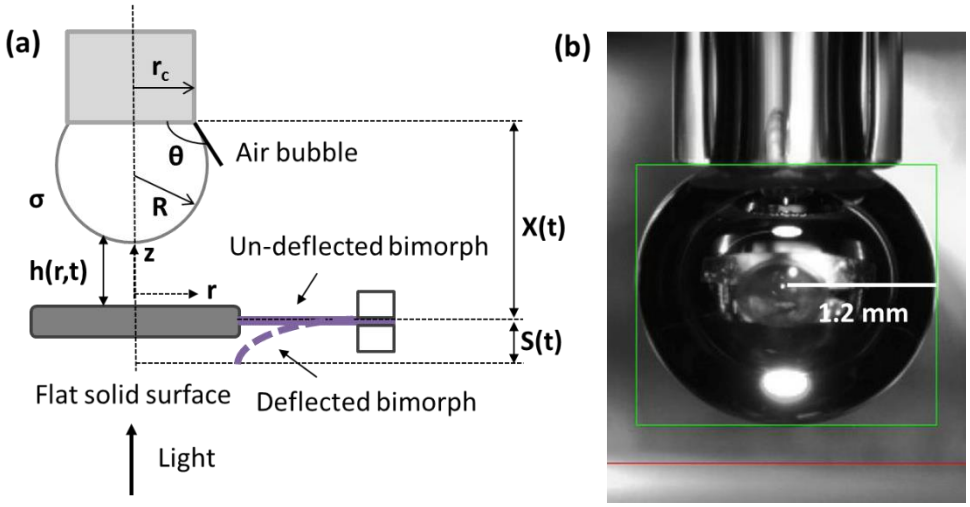

Figure 4-1. (a) Schematic diagram of an air bubble approaching a flat solid surface where main parameters are defined. σ: interfacial tension of air-water interface (σ = 72.0 ± 0.3 mN/m); r_c: the inner radius of the capillary; θ: the angle that the bubble makes with the capillary at r_c (θ = 147 ± 3°); R: the radius of un-deformed air bubble (R = 1.20 ± 0.01 mm); X(t): the distance between the end of the capillary and the un-deflected bimorph; S(t): the deflection of the bimorph. (b) Side view image of the bubble at the end of the capillary above the flat solid surface in test liquid. The horizontal line locates the position of the flat solid surface and the square is drawn to control the size of the bubble.

4.2.2 Bubble generation and flat solid surfaces

An air bubble with the desired radius of 1.20 ± 0.01 mm was generated at the end of the glass capillary using a gastight micro-syringe (Figure 4-1b). Generally, one end of the capillary with an inner diameter of 1.10 ± 0.05 mm was smoothed by sand paper and then heated with a butane flame to ensure a uniform geometric symmetry at the end of the capillary tube, which is appropriate for reproducible generation of bubbles. The generation

process of the bubble and its size was monitored by the real-time camera through the side window.

The investigated solid surface was fused silica glass with a diameter of 10 ± 0.2 mm and thickness of 1 ± 0.38 mm. The surface is quite smooth with a root mean square (RMS) roughness less than 1nm characterized by AFM imaging.

Both the capillary and the solid surface were cleaned with freshly prepared piranha solution (H_2SO_4 : H_2O_2= 3:1 by volume) for one hour and rinsed with Milli-Q water before experiments. Thus, the solid surface is completely water-wettable (contact angle ≈ 0º).

4.2.3 Displacement and approach velocity control

In order to study the effect of approach velocity on thin liquid film drainage between a bubble and a solid surface, the air bubble is driven towards the lower flat solid surface in a desired manner by a motorized actuator or a speaker diaphragm. Approach velocities of 0.01, 0.1 and 1 mm/s were accomplished by motorized actuator including acceleration and deceleration. The initial separation between the bubble and the solid surface was kept to 300 μm for these three velocities. The total displacement was set to 400 μm to guarantee that the velocity of the bubble could reach the set velocity before it contacted with the solid surface. As a result, an overlap of 100 μm between the bubble and the solid surface was achieved resulting in the same deformation of the bubble and the same size of the liquid film for these three velocities. The detailed displacement trajectory and real-time velocity of these three cases are shown in Figure 4-2a, b and c. The displacement signals were independently measured by a displacement sensor (Black curves in Figure 4-2). Thus, the real-time velocity of the bubble can be calculated by smoothing and differentiating the

displacement signals as shown in blue curves in Figure 4-2. The time zero corresponds to the moment that the bubble starts moving.

When the approach velocity was set to 0.01 mm/s, the bubble underwent a short acceleration for 0.2 s followed by uniform motion with constant velocity of 0.01 mm/s until 46.05 s and stopped moving after a short deceleration (Figure 4-2a). The bubble started to deform at 34.16 s when the total displacement reached 300 μm. After 46.05 s, the bubble was held at this position allowing the film drainage process to complete.

When the approach velocity increased to 0.1 mm/s, the bubble completed the acceleration and reached the desired velocity at 0.5 s. Then, it moved uniformly at 0.1 mm/s till 3.82 s, decelerated until 4.45 s and entered the holding period afterwards. According to the displacement signal in Figure 4-2b, the deformation of the bubble started at 3.17 s so that the initial deformation process happened in the uniform motion and continued during the deceleration motion.

As shown in Figure 4-2c, the bubble accelerated from zero to 1 mm/s over a period of 0.2 s when the approach velocity is 1 mm/s. Since the total displacement is short for such high velocity, the bubble underwent a uniform motion for just 0.2 s until 0.35 s and decelerated until 0.6 s when the holding period started. The bubble began to deform at 0.35 s as well in this case, meaning that the whole film drainage process occurred during the deceleration and holding period rather than during uniform motion, as was for the above two cases.

To achieve bubble velocity over 10 mm/s, which is four orders of magnitude higher than the lowest approach velocity (0.01 mm/s), a speaker diaphragm was used to drive the bubble towards the solid surface. A computer generated waveform controlled the pattern of the displacement to realize the relatively high approach velocity of 14 mm/s. To obtain

the same deformation of the bubble and the same size of the film as that in the above three cases, the overlap between the bubble and the solid surface was fixed to be 100 μm. Because of the limitation in moving displacement of the speaker diaphragm compared to the motorized actuator, the initial gap between the bubble and the solid surface was set to be 30 μm and the total displacement was set to be 130 μm.

The displacement and corresponding velocity signal when the approach velocity is 14 mm/s are shown in Figure 4-2d. The speaker diaphragm has a response time of 5 ms so that the bubble started to move after 5 ms (inset in Figure 4-2d). It took less than 1 ms for the bubble to accelerate to the desired velocity of 14 mm/s. Then the bubble uniformly moved with 14 mm/s until it reached the maximum displacement of 130 μm at 15 ms. According to the displacement signal, the bubble began to deform at about 7 ms with the velocity of 14 mm/s, which remained constant during the further deformation of the bubble. After 15 ms, the bubble stopped moving and should be held at the same position for a period of time to allow the film to drain. However, there was further displacement from 130 μm to around 200 μm due to the relaxation of the speaker diaphragm after rapid movement, which resulted in the slower deceleration to zero and the observation of further increase of the film size. All the experiments mentioned above are conducted under room temperature of 22 ºC.

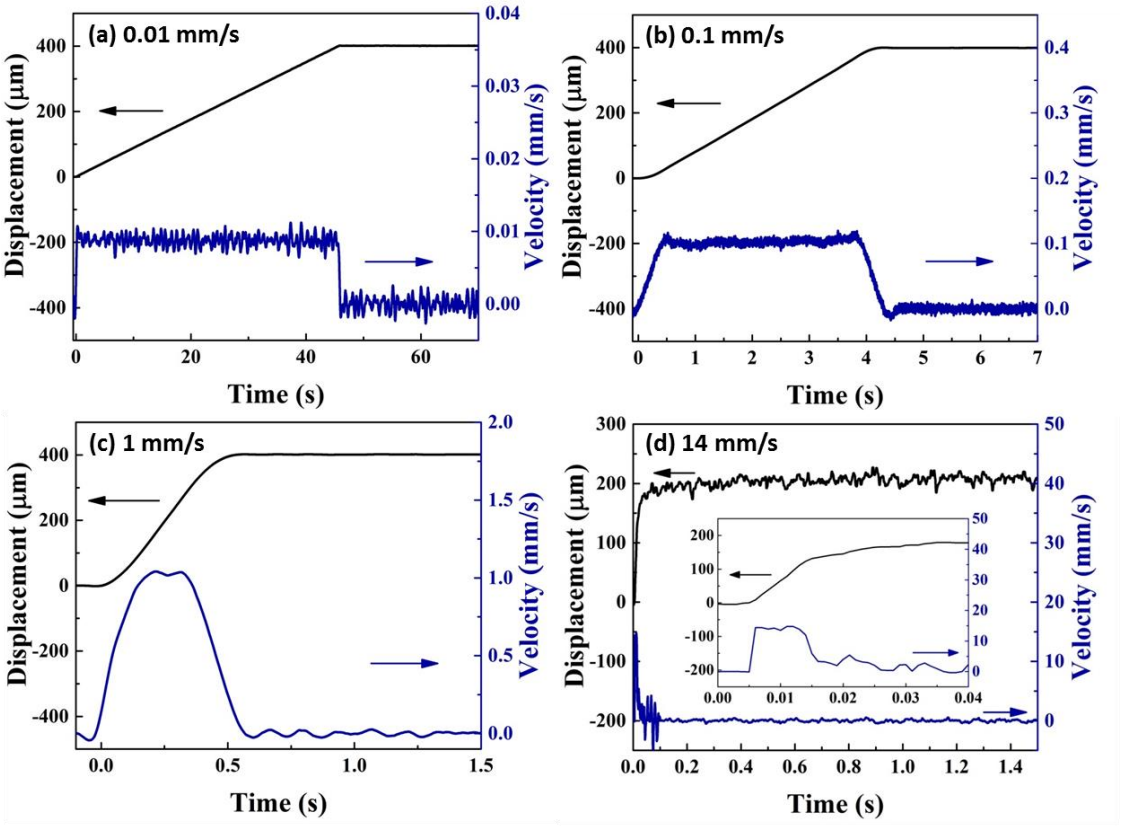

Figure 4-2. Displacement controlled by the motorized actuator or the speaker diaphragm and the real-time velocity of the bubble approaching the lower flat solid surface with the approach velocity: (a) 0.01 mm/s, (b) 0.1 mm/s, (c) 1 mm/s and (d) 14 mm/s, the inset is the enlarged plot of the first 40 ms.

4.3 Theoretical model

The experimental results are theoretically studied using the Stokes-Reynolds-Young-Laplace (SRYL) model that has been applied in the analysis of experimental measurements taken by AFM[19] and SFA[39]. In the ITLFFA, the large difference in length scale between the film width (~200 μm) and the thickness of the film (~1 μm) implies the small variation of the film thickness as a function of film radius. Thus, the dynamics of liquid film drainage

between the bubble and flat solid surface is described by the lubrication theory under Stokes flow. The deformation of the liquid-air interface is described by the augmented Young-Laplace equation with the reasonable assumption that the bubble can adjust its shape instantaneously to accommodate changes in the total film pressure. In addition, the bubble is considered to be at constant volume because the size of the bubble is well-controlled by the gastight micro-syringe.

Governing equations

In our experiments, a bubble with radius (R) of 1.2 mm was driven towards the surface with velocity V ranging from 0.01 mm/s to 14 mm/s, which gives global Reynolds numbers from 0.027 to 37.75. However, the film drainage process is characterized by the film Reynolds number $Re_f = \rho h_f V_f/\mu$, where h_f is the film thickness and V_f is the velocity of the air-water interface of the film. As h_f << R (~μm), Re_f <<1, it permits the quantitative analysis of the spatiotemporal film thickness $h(r,t)$ by lubrication theory. Therefore, the Stokes-Reynolds equation describes the film thinning process as[35]:

$$\frac{\partial h}{\partial t} = \frac{1}{12\mu r}\frac{\partial}{\partial r}\left(rh^3\frac{\partial p}{\partial r}\right) \tag{4-1}$$

where $p(r,t)$ is the excess hydrodynamic pressure in the film relative to the bulk liquid. In Eq. (1), the hydrodynamic boundary condition at the air-liquid interface is the tangentially immobile condition which is the same as that at the hydrophilic solid-liquid interface. The use of immobile boundary condition is justified based on the comparisons between theory and experimental results[21, 35]. Moreover, the obtained experimental results by the ITLFFA that will be shown in the results section support the immobile boundary condition rather than the mobile boundary condition at the air-liquid interface. In our system, extreme care has been taken to ensure the cleanliness, however, we still cannot completely rule out the

contamination of the solution as indicated by slightly lower surface tension value of aqueous phase (72.0 mN/m in our case vs 72.4 mN/m as reported for ultraclean systems, despite of great care that was given in purifying our water). The immobile boundary condition at the bubble surface is therefore attributed to the existence of a trace amount of surface active impurities[19-20, 40].

Assuming a bubble with constant interfacial tension, σ, the augmented Young-Laplace equation can be written as[41]:

$$\frac{\sigma}{r}\frac{\partial}{\partial r}\left(r\frac{\partial h}{\partial r}\right) = \frac{2\sigma}{R} - p - \Pi(h) \tag{4-2}$$

where $\Pi(h(r,t))$ is the disjoining pressure in the film. In our system, the disjoining pressure is defined as the sum of electrical double-layer interaction[42] Π_{edl} and van der Waals interaction[43-44] Π_{vdw}:

$$\Pi = \Pi_{edl} + \Pi_{vdw} = 64nkT * \tanh\left(\frac{ze\varphi_{sl}}{4kT}\right) * \tanh\left(\frac{ze\varphi_{bl}}{4kT}\right)\exp(-\kappa h) - \frac{A}{6\pi h^3} \tag{4-3}$$

where A is the Hamaker constant, n is the number of electrolyte ions per unit volume in the aqueous film, k is the Boltzmann constant, ze is the charge on the electrolyte ions, T is the absolute temperature and κ^{-1} is the Debye length. φ_{sl} and φ_{bl} are the surface potential of solid-liquid and bubble-liquid interface, respectively. The equation for calculating Π_{edl} is valid for $\kappa h \gg 1$ and no assumption was made regarding the magnitude of the surface potentials. In our experiments, two KCl concentrations (10^{-5} M and 0.1 M) were considered. The Hamaker constant A is -1.1×10^{-20} J according to the literatures[45-46]. The surface potentials of the solid-liquid interface were measured to be -111 mV in 10^{-5} M KCl solution and -32 mV in 0.1 M KCl solution. The surface potentials of the bubble-liquid interface under different conditions are taken from literature as -40 mV[47]. The disjoining pressures of different salt concentrations are plotted in Figure 4-3. In the case of low salt

concentration (10^{-5} M), the electrical double-layer interaction is dominant so that the van der Waals interaction becomes negligible. On the other hand, when the salt concentration increases to 0.1 M, the van der Waals interaction becomes dominant.

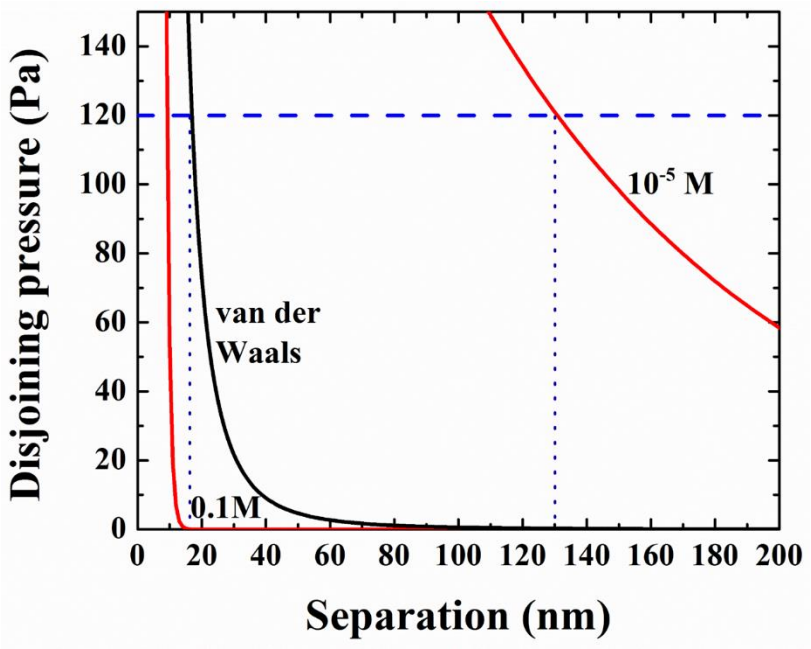

Figure 4-3. Disjoining pressure due to electrical double-layer interaction for different salt concentrations (red line) and van der Waals interaction (black line). The magnitude of the Laplace pressure inside the bubble (120 Pa) is indicated by the horizontal dashed line, while the equilibrium film thickness is given by the dotted line.

Initial and Boundary conditions

Eqns. (4-1) and (4-2) are solved numerically using suitable initial and boundary conditions within the domain $0<r<r_{max}$. The choice of r_{max} should be sufficiently large so that the numerical results are independent of r_{max}, but not too large. The initial condition must be consistent with eqn. (4-2) generating zero film pressure when the bubble is far from the

surface. The parabolic profile of the air-liquid interface meets the requirement to give initial condition as

$$h(r,0) = h_0 + \frac{r^2}{2R} \tag{4-4}$$

where h_0 is the initial separation between the bubble and the solid surface.

Since we are dealing with the axisymmetric interactions, symmetry conditions apply at r=0:

$$\frac{\partial h}{\partial r} = 0 \tag{4-5}$$

$$\frac{\partial p}{\partial r} = 0 \tag{4-6}$$

Outside the interaction region, the pressure decays like r^{-4}, so the pressure at $r=r_{max}$ can be implemented as[48]:

$$r\frac{\partial p}{\partial r} + 4p = 0 \tag{4-7}$$

The bubble is assumed to be pinned at the end of the capillary and the interaction happens at constant volume. Due to the deformation of the bubble caused by the force acting on it, the surface of the bubble outside the interaction region does not move at the same rate as the motion of the capillary tube. Thus, the boundary condition that takes these features into account at $r=r_{max}$ can be expressed as[41]:

$$\frac{\partial h(r_{max},t)}{\partial t} = \frac{dD(t)}{dt} - \frac{1}{2\pi\sigma}\frac{dF(t)}{dt}\left\{\log\left(\frac{r_{max}}{2R}\right) + 1 + \frac{1}{2}\log\left(\frac{1+cos\theta}{1-cos\theta}\right)\right\} \tag{4-8}$$

with $D(t) = S(t) + X(t) = \frac{F(t)}{K} + X(t)$

and we define the force $F(t)$ as the sum of contributions from hydrodynamic force (F_h) and disjoining force (F_Π) to facilitate the explanation in the next section:

$$F(t) = F_h + F_\Pi = 2\pi\int_0^\infty [p(r',t) + \Pi(h(r',t))]r'dr' \tag{4-9}$$

The detailed description of the numerical implementation in Matlab including scaling the governing equations can be found elsewhere[41] . Parameters used in the model were either

taken from independent measurements or literature (Table 4-1). A slightly lower surface tension value of 72.0 mN/m as compared with the reported value of 72.4 mN/m indicates the presence of a trace amount of surface active species in our aqueous systems. The presence of such surface active species appears to make the bubble surface immobile, a boundary condition that is needed to match the measured bubble profiles and interaction forces with that predicted by the SRYL model.

Table 4-1. Experimental and theoretical parameters of the bubble-silica system in ITLFFA

physical parameter	**experiment**	**theory**
bubble radius, R	1.20 ± 0.01 mm	1.2 mm
the angle that the bubble makes at the end of capillary, θ	147 ± 3°	147°
viscosity, μ	0.89 mPa·s	0.89 mPa·s
surface tension, σ	72.0 ± 0.3 mN/m	72 mN/m
initial separation, h_0	300 ± 10 μm 30 ± 10 μm	290-300 μm 40 μm
maximum displacement, ΔX	400 ± 10 μm 130 ± 10 μm	400 μm 130 μm

4.4 Results and discussion

In our experiments, the spatiotemporal film thickness and the interaction force were measured simultaneously when the bubble interacts with the hydrophilic silica surface using ITLFFA. Four different approach velocities, which are 0.01, 0.1, 1 and 14 mm/s, were studied under 10^{-5} M KCl solution to emphasize the significance of approach velocity. It is worth mentioning that the actual drive function of the bubble towards the solid surface

is not uniform motion as shown in Figure 4-2. The acceleration and deceleration ramp has a significant effect on the modeling results especially when the approach velocity is relatively high. Thus, the real-time velocity functions in Figure 4-2 are used as input in the model to achieve better agreement between theory and experiments. In addition, different salt concentrations were used as background solution with the same approach velocity (1 mm/s) to indicate the influence of surface forces on the initial film drainage and equilibrium film thickness.

4.4.1 Effect of approach velocity on film drainage

Typical experimental data of film profiles and temporal film thickness at the barrier rim and center of the film of the four approach velocities mentioned above are shown in Figures 4-4 and 4-5. Meanwhile, the results from the theoretical model are included for comparison. When the approach velocity was 0.01 mm/s that is within the available range of velocity of AFM and SFA, the deformation of the bubble is quite small as the film profile is almost flat shown in Figure 4-4a. The dimple formed at the film thickness of 209 nm. The difference of thickness between the center and the barrier rim of the film was only 10 nm (Figure 4-5a). The film drained to the equilibrium flat film with the thickness of 130±5 nm at the end, which agrees well with the prediction from the classical DLVO theory. The equilibrium film thickness was independent of approach velocity and stayed the same for all other cases.

Increasing the approach velocity of the bubble to 0.1 mm/s, the dimple formation could be clearly observed from the experimental film profile at the thickness of 652 nm (Figure 4-4b). As shown in Figure 4-4b, the thickness at the barrier rim gradually decreased when the film drained, while the thickness at the center remained at 600 nm first and then

decreased after the bubble stopped moving, which resulted in the formation of a pronounced dimple. The model quantitatively predicts the drainage behavior for the entire process except that the thickness at the center of the film shows slight difference from the experimental results (Figure 4-5b).

When the approach velocity increased to 1 mm/s, an even more pronounced dimple formed at a higher thickness of 2074 nm, which resulted in a difference of 1500 nm between the center and the barrier rim of the film (Figure 4-4c). During the deceleration period of the bubble motion, the dimple became more and more pronounced as the thickness of the film at the barrier rim decreased continuously while the thickness at the center of the film remained almost constant. After the bubble stopped, the thickness at the center of the film increased slightly from 1920 nm to 1945 nm while the thickness at the barrier rim decreased, which might be the consequence of the discontinuity in acceleration as the bubble stopped. Then the liquid film continued to drain without changing the film width. In Figure 4-4c, the shape of the bubble was predicted very well by the theoretical model. The "central bounce" phenomenon was qualitatively predicted by the model as well. In spite of the little variation of the thickness at the center of the film in the early stage caused by the rapid movement, the theoretical temporal film thickness at both the center and the barrier rim of the film provided good agreement with the experimental data (Figure 4-5c).

In the case of 14 mm/s approach velocity, the speaker diaphragm was used leading to shorter displacement and initial gap compared to the above three cases. Thus, the head of the bubble "bounced" for 3-4 times even after the capillary stopped moving until around 0.1 s. This bouncing behavior made a slightly asymmetric film and the start of dimple formation could not be tracked. Therefore, Figure 4-4d only displays film profiles when a

dimple had already formed. During the evolution of the dimple, the film thickness at the barrier rim monotonically decreased while the thickness at the center decreased following an initial bounce. The continuous increase of the film width was attributed to the relaxation of the speaker as mentioned in the last section. The slight difference between the experimental and theoretical film profile at the center of the film was due to the rapid motion mode of the bubble. A comparison of the variation of observed and theoretical film thickness with time at the center and barrier rim of the dimple is given in Figure 4-5d. The theory agrees with the experiments except for the central bounce behavior at the initial stage of the process.

The corresponding interaction forces for these four different approach velocities were measured simultaneously and compared with the theory as shown in Figure 4-6. As mentioned above, the bimorph is quite stiff and the deformation of the bubble is small compared to the size of the bubble. So fluctuations existed in the force measurement causing the noise in the measured force curves. In all cases, the force started to increase from zero as the bubble began to deform. The force continued increasing when the film size became larger until the bubble stopped moving. In the holding period, the force remained constant around 15 μN for all the cases shown as the flat line with noise even when the film still drained. The initial jump of the force in the case of 14 mm/s approach velocity is the consequence of close initial separation between the bubble and the surface (Figure 4-6d). From the comparison, the theoretical interaction force has an excellent agreement with the measured force.

For the four different approach velocities, the theory provides reasonable qualitative and quantitative prediction on the evolution of the spatiotemporal film thickness and

corresponding interaction forces. The good agreement between the experiments and the theory guarantees the further quantitative analysis of the physical parameters that influence the dynamic drainage process, which helps us explain the observed phenomenon in the above four cases.

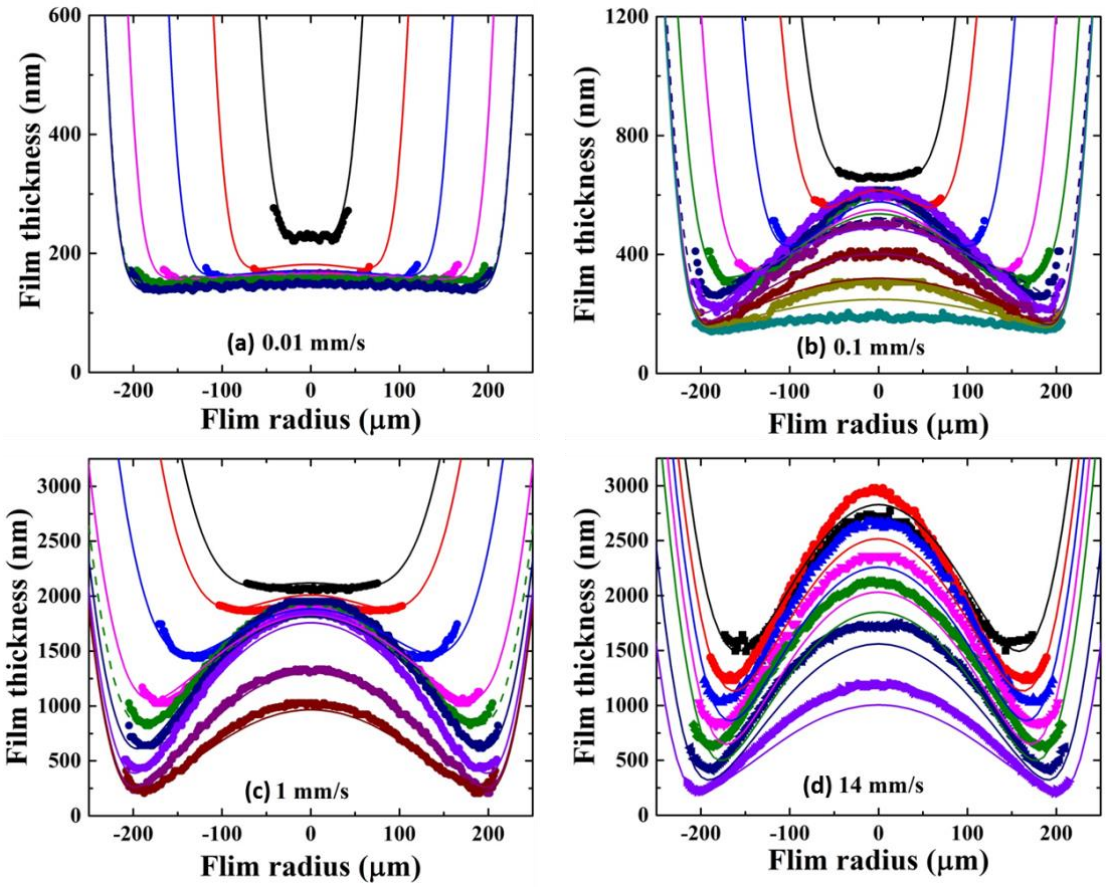

Figure 4-4. Comparison between theoretical model (lines) and experimental results (points) of spatiotemporal film thickness for a bubble interacting with a flat hydrophilic surface in 10^{-5} M KCl solution with different approach velocities. The dashed lines indicate the moment that the bubble stopped moving. The measured time of profiles from top to bottom is: (a) 34.982, 37.018, 40.117, 43.745, 46.964 and 66.887 s. (b) 3.311, 3.399, 3.620, 3.930, 4.151, 4.461, 5.345, 10.478, 15.834, 23.669 and 39.685 s. (c) 0.377, 0.392, 0.437, 0.507,

0.567, 0.687, 1.197, 4.542 and 9.075 s. (d) 0.126, 0.189, 0.286, 0.444, 0.671, 1.423 and 6.791 s.

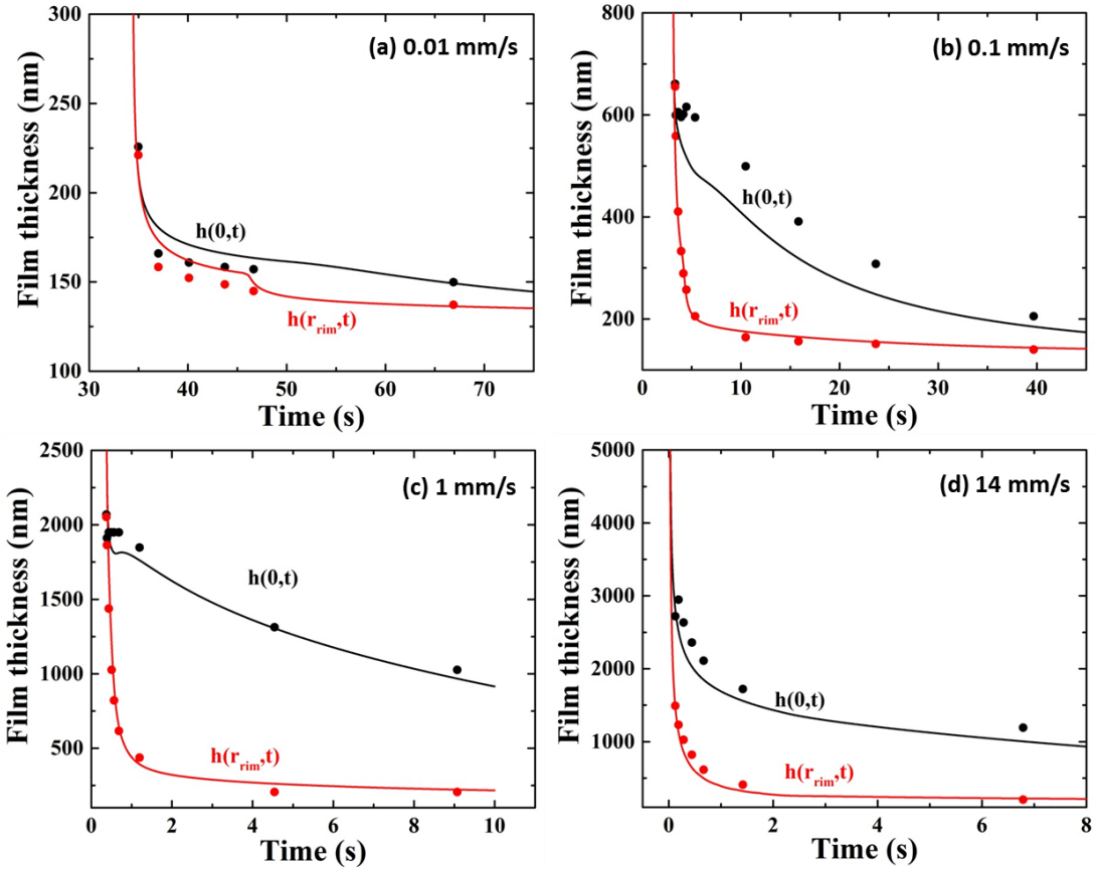

Figure 4-5. Film thickness at the center h(0,t) and at the barrier rim h(r_{rim},t) as a function of time with different approach velocities. The solid lines are the theoretical results from the model while the points are experimental data.

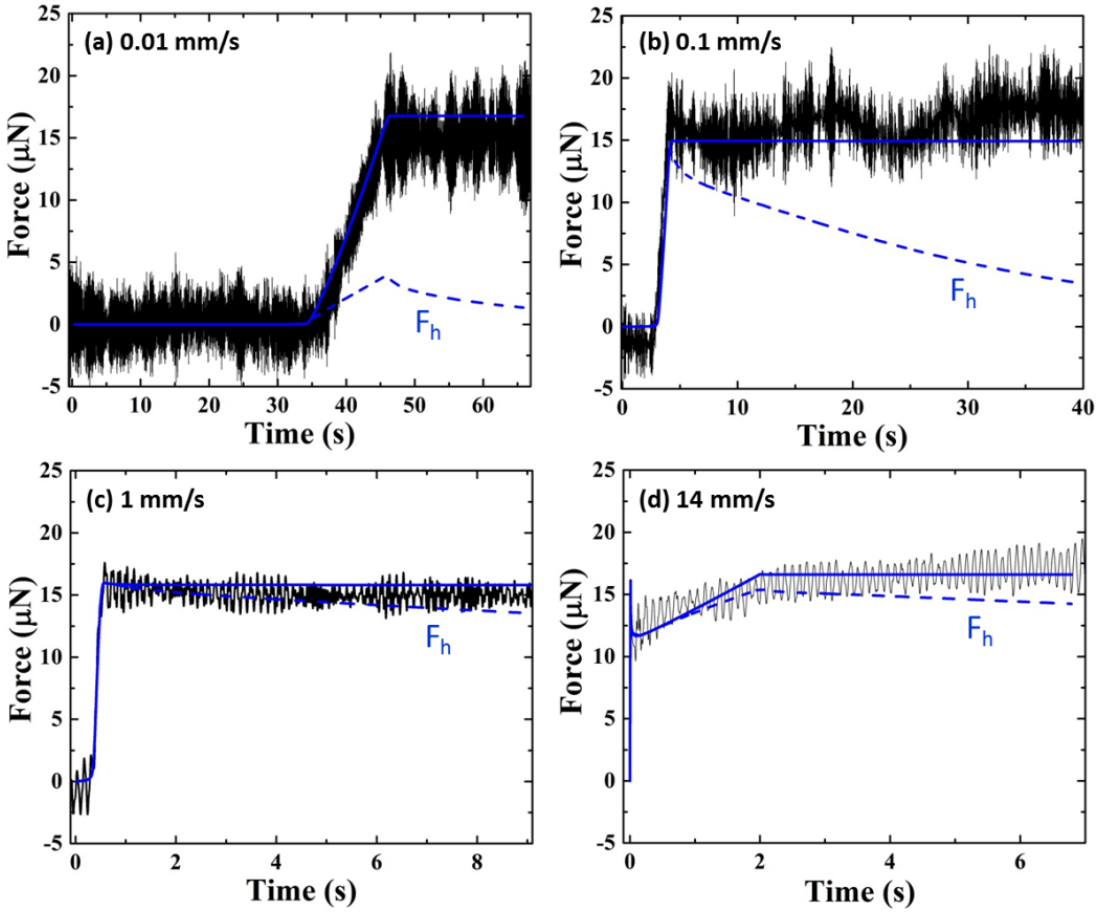

Figure 4-6. Comparison between measured force (black solid line) and theoretical force (blue solid line) of the bubble interacting with a flat hydrophilic surface in 10^{-5} M KCl solution with different approach velocities. The dashed lines are the hydrodynamic force calculated from the model (See F_h in eqn. (4-9)).

4.4.2 Hydrodynamic effects on film drainage

The formation of dimple mostly results from the larger hydrodynamic pressure that exceeds the pressure inside the bubble, which inverts the curvature of the air-liquid interface. For the air bubble interacting with the hydrophilic silica surface during the approaching period in our system, the hydrodynamic pressure is dominant as the larger film thickness results in negligible disjoining pressure. As the film drains, the hydrodynamic pressure eventually decays to zero and the film becomes flat due to electrostatic repulsion. As shown in the

previous section, the theoretical model predicted the experimental spatiotemporal film thickness and interaction forces consistently, therefore can be used to quantitatively extract the contributions of hydrodynamic and disjoining pressure, which are not available experimentally. The hydrodynamic pressures for the film profiles in Figure 4-4 were calculated from the model and shown in Figure 4-7. In our experiments, the pressure inside the bubble is $\frac{2\sigma}{R} = 120\ Pa$. In Figure 4-7, we scaled the pressure by $\frac{\sigma}{R}$, so the pressure becomes 2 in non-dimensional units. By integrating the hydrodynamic pressures in Figure 4-7, the temporal hydrodynamic force was obtained for each case as shown in Figure 4-6. When the approach velocity was 0.01 mm/s, the total hydrodynamic force in the film began to increase from zero to the maximum as the bubble stopped moving (Figure 4-6a). The maximum hydrodynamic force is only one third of the total force as the disjoining pressure became important early in this case. In Figure 4-7a, the hydrodynamic pressures across the film were all much less than 2 and the hydrodynamic pressure difference between the center of the film and the barrier rim was quite small. Therefore, the dimple appeared at lower film thickness and a negligible dimple formed.

Increasing the approach velocity to 0.1 mm/s, only the hydrodynamic force existed in the film initially and gradually increased before the bubble stopped moving (Figure 4-6b). The maximum hydrodynamic force was just a little smaller than the maximum total force (15μN). As the time progressed, the hydrodynamic force decreased and the disjoining pressure became dominant. The scaled hydrodynamic pressure at the center was larger than 2 before the bubble stopped moving and lower than 2 afterwards (Figure 4-7b). Consequently, the more pronounced dimple formed at higher film thickness compared to

the case of 0.01 mm/s. The dimple became more and more obvious before the bubble stopped moving and was flattened afterwards.

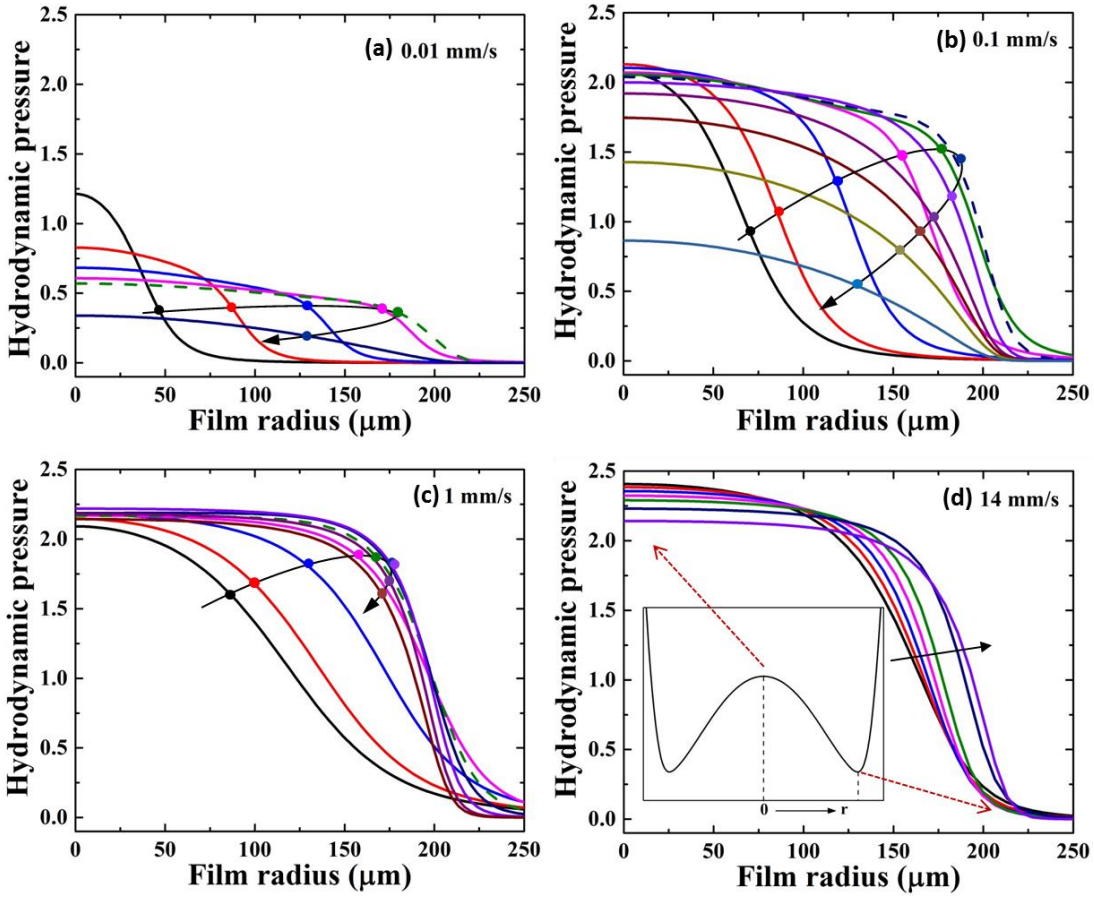

Figure 4-7. Comparison of scaled hydrodynamic pressure for different approach velocities. Every pressure profiles correspond to the film profiles in Figure 4-4. The arrows indicate increasing time. The dashed lines indicate the time that the bubble stopped moving. The inset of (d) is an example of film profile that helps indicate the center and the barrier rim of the film.

When the approach velocity increased to 1 mm/s, the maximum hydrodynamic force reached the same value around 15μN as the total force when the bubble stopped moving (Figure 4-6c). After this, the hydrodynamic force decreased as well. Nevertheless, the decreasing rate was much lower than the above two cases indicating that the hydrodynamic

force was still dominant after the bubble stopped moving. The hydrodynamic pressure at the center remained higher than 2 in the holding period and slightly increased leading to the appearance of "central bounce" phenomenon (Figure 4-7c). The pressure gradient between the center and the barrier rim of the film increased compared to the cases of lower approach velocity. Thus, the dimple first formed at a film thickness as high as 2000 nm and became even more pronounced a few milliseconds after the bubble entered the holding period.

Further increasing the approach velocity to 14 mm/s, the hydrodynamic force was dominant for a long time during the drainage process (Figure 4-6d). The decreasing rate of the hydrodynamic force was the lowest among these four approach velocity cases. In this case, all the film profiles shown in Figure 4d were in the holding period. The hydrodynamic pressure at the center for these film profiles was larger than the above three cases (Figure 4-7d). As a result, the dimple formation occurred at the highest film thickness among these four approach velocities.

From the model, the shear rate can be evaluated at the bubble-liquid interface for these four cases that gives insight into details of fluid flow within the draining film. On the basis of lubrication theory, the velocity of the liquid film between the bubble and the solid surface during the drainage process is parabolic which is given by $u = \frac{1}{\mu}\frac{\partial p}{\partial r}(\frac{z^2}{2} - \frac{hz}{2})$. Therefore, the shear rate ($\dot{\gamma}$) at the bubble-liquid interface ($z = h$) can be expressed as[41]:

$$\dot{\gamma} = -\frac{du}{dz} = -\frac{h}{2\mu}\frac{\partial p}{\partial r} \tag{4-10}$$

From Figure 4-8, we observe that the shear rate is almost zero at the center of the film and increases to maximum value around the barrier rim. Also, the shear rate initially increased when the bubble was approaching and decreased as the film drained for all cases. For the

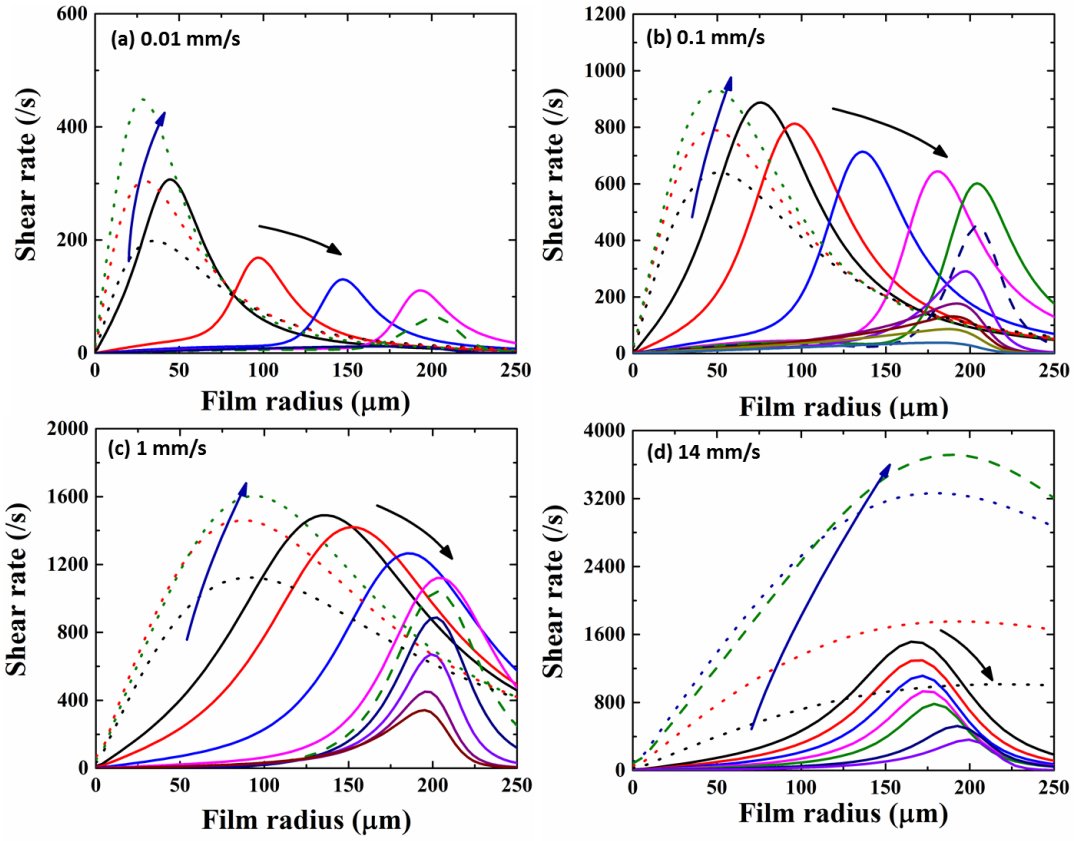

Figure 4-8. Shear rate at the bubble/electrolyte interface for different approach velocities. The solid lines correspond to the bubble profiles in Figure 4-4. The dashed lines indicate the time that the bubble stopped moving. The dotted lines represent times before the first film profile observed in Figure 4-4. The arrows indicate increasing time.

first three cases with lower approach velocities, the shear rate reached a maximum value before the bubble began to deform. When the approach velocity increased to 14 mm/s, the maximum shear rate occurred at the moment that the bubble stopped moving in which the bubble had already deformed. Furthermore, the maximum shear rate increased with increasing approach velocity. When the approach velocity increased tenfold, the maximum shear rate only increased twofold because the bubble could deform itself to accommodate the large shear in the film. When the bubble stopped moving, the shear rate was 40 times

larger in the case of 14 mm/s approach velocity than that with the approach velocity of 0.01 mm/s. Thus, the bubble deformed more to form a pronounced dimple in the case of high approach velocity resulting in longer drainage process.

4.4.3 Effect of salt concentration on film drainage

In order to study the influence of surface forces on the drainage process, the concentration of the background solution was varied. As mentioned above, in 10^{-5} M KCl solution, the large repulsive force is mainly contributed by the electrical double-layer interaction while the van der Waals interaction is negligible. Therefore, as comparison, a high salt concentration resulting in negligible electrical double-layer interaction and dominant repulsive van der Waals interaction was studied.

Using the same model, the film profile of high salt concentration (0.1 M) can be predicted well as shown in Figure 4-9a. Compared with the case of 10^{-5} M salt concentration (Figure 4-4c), the film thickness of dimple formation remained the same. In the initial drainage process (<1 s), the two cases of different salt concentrations had the same drainage rate as the surface force is negligible at large film thickness. As the film continued draining, the film thickness at the barrier rim of 0.1 M salt concentration quickly reached a smaller value than that of 10^{-5} M salt concentration due to the less repulsive electrical double-layer interaction. Thus, there was a narrow channel at the barrier rim for the liquid inside the film to drain out in the case of 0.1 M KCl solution, leading to a slower drainage rate at the center of the film (Figure 4-9b). As a result, it took about 30 min for the film to reach stable equilibrium state while it took only about 2 min in the case of low salt concentration. Besides, the equilibrium film thickness was just 17 nm in 0.1 M KCl solution, which was much smaller than that in 10^{-5} M KCl solution (130 nm).

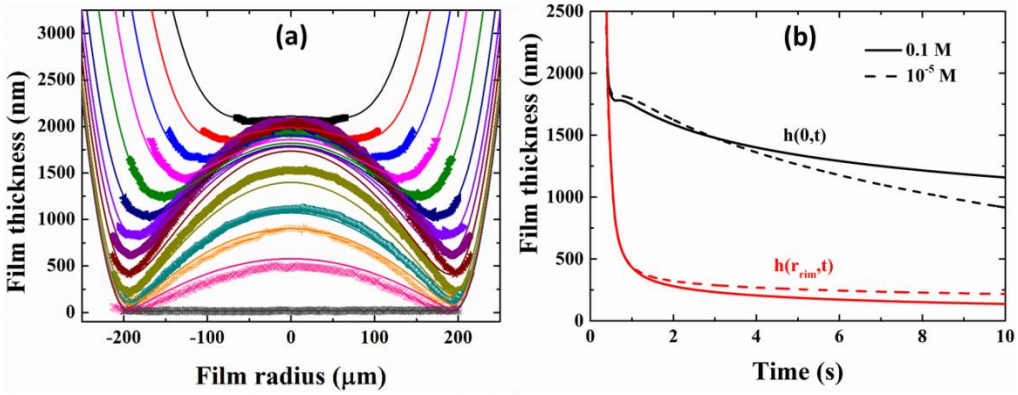

Figure 4-9. (a) Film profile of a bubble interacting with a hydrophilic surface in 0.1 M KCl solution with 1 mm/s approach velocity. The points indicate the experimental film profiles while the solid lines show the theoretical results from the model. (b) Theoretical film thickness at the center h(0,t) (black) and at the barrier rim $h(r_{rim},t)$ (red) as a function of time in 10^{-5} M (dashed line) and 0.1 M (solid line) KCl solution.

4.4.4 Film thickness of dimple formation

Considering a bubble with immobile boundary condition, the first occurrence of the dimple formation h_d can be expressed as[41]:

$$h_d = cR\sqrt{Ca} \tag{4-11}$$

In eqn. (4-11), Ca is the capillay number which can be written as $Ca = \mu V/\sigma$. The constant c ranges from 0.4-0.7[49] depending on Ca and the angle that the bubble makes at the end of the capillary. Therefore, by determining the constant c, the height of dimple formation can be obtained for different bubble approach velocities. From our experimental results, the thickness where the dimple develops can be obtained for approach velocities of 0.01, 0.1 and 1 mm/s, respectively. Due to the initial bubble bouncing behavior and the corresponding asymmetric film profile, the h_d of the case of 14 mm/s approach velocity is difficult to be obtained from the experiment. As shown in Figure 4-10, the experimental

h_d (filled circles) of these three approach velocities follows the relationship in eqn. (4-11) with the capillary number and the bubble approach velocity as well. By fitting these experimental data (solid line in Figure 4-10), the value of the constant c is determined to be 0.49. This result can be used to predict the first occurrence of dimple formation for other approach velocities in our system without conducting any experiment. For example, the h_d of 14 mm/s approach velocity is estimated to be 7.7 μm according to eqn. (4-11).

The behavior of the dimple formation described by eqn. (4-11) is universal for other experimental systems described in the literature[50]: mercury drop in water against a mica surface[29] (open stars in Figure 4-10), bubble rising in water against a glass plate[35, 51] (open squares), and two drops in immiscible liquid[52] (open triangles). The film thickness at which a dimple first develops all follows the scaling law as $Ca^{1/2}$ with different values of constant c in these experimental systems depending on whether the bubble or drop interacts with a solid or deformable surface. However, for ethanol drops falling against a glass surface in air, the h_d scales with the velocity as $V^{-1/2}$ in the high-velocity regime when the inertia is dominant[53]. The difference of constant c is caused by the different angles that the bubble/drop makes at the end of the capillary. In our experiments, the bubble was pinned at the end of the capillary with larger angle compared to experiments by other researchers. In addition, from Figure 4-10, our experimental results fill the velocity gap with other techniques for deformable-solid surface interactions in aqueous system.

As the film thickness of dimple formation determines the drainage time, the correlation shown in Figure 4-10 can potentially be extended to show the relationship between drainage time and Ca (Appendix B Figure B1) to study collison stability of colloid particles, which is similar to experiments that try to correlate bubble coalescence time to the force[54].

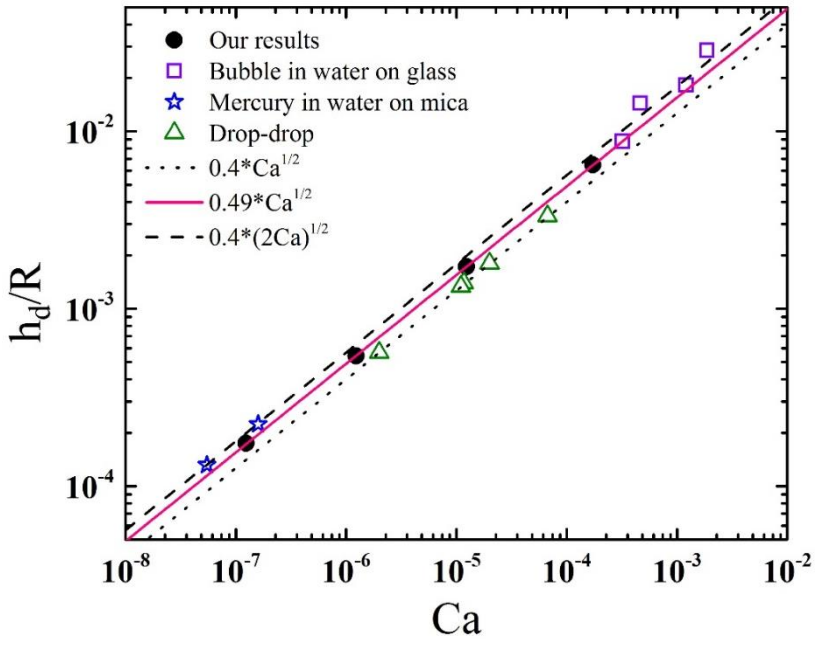

Figure 4-10. Variation of the height of dimple formation with capillary number for different systems. The filled points are from experimental measurements in this work while the open symbols are from experiments conducted by other researchers[29, 35, 51-52]. The lines are the theoretical results.

4.5 Conclusions

With the ability to measure interaction forces and spatiotemporal film thickness simultaneously under a wide range of hydrodynamic conditions that are not available in similar experimental work, the ITLFFA allows the systematic study of the effect of bubble approach velocity and salt concentration on the drainage of thin liquid film trapped between an air bubble and a solid silica surface. The first occurrence of dimple formation is a function of bubble approach velocity and independent of salt concentration. The bubble approach velocity determines the shape of the film profile, therefore, influencing the dynamics of the drainage process, which indicates that the global Reynolds number plays

a role in the initial film drainage process that is characterized by the film Reynolds number. The salt concentration mainly affects the drainage time and equilibrium film thickness. The agreement between the experiment and theory demonstrates that the SRYL model can be applied to the system with a wider range of global Reynolds number as long as the film Reynolds number is small. Such a good agreement also allows us to use the model to infer quantitative information about the distribution of the film pressure and the details of the fluid flow within the liquid film, which cannot be directly measured. It helps us have deep understanding of the effects of bubble approach velocity and salt concentration on the drainage process of the liquid film. In addition, the relationship between the bubble approach velocity and the experimental thickness of the development of first dimple guarantees the accurate prediction of the first occurrence of dimple formation using the analytical solution. In summary, without reconciling experimental results obtained using different instruments and/or from different laboratories, the systematic qualitative and quantitative study of thin liquid film drainage under a wide range of hydrodynamic conditions can be realized by a single device-ITLFFA. This study has practical implications in a number of industrial processes in which the hydrodynamic condition is a key parameter.

4.6 References

1. Ralston, J.; Fornasiero, D.; Hayes, R., Bubble-Particle Attachment and Detachment in Flotation. *Int J Miner Process* **1999**, *56*, 133-164.

2. Nguyen, A. V.; Schulze, H. J.; Ralston, J., Elementary Steps in Particle-Bubble Attachment. *Int J Miner Process* **1997**, *51*, 183-195.

3. Nguyen, A. V., Particle-Bubble Interaction in Flotation. *Prog Colloid Interf* **2011**,

2, 351-383.

4. Durian, D. J.; Weitz, D. A.; Pine, D. J., Multiple Light-Scattering Probes of Foam Structure and Dynamics. *Science* **1991**, *252*, 686-688.

5. Whitesides, G. M., The Origins and the Future of Microfluidics. *Nature* **2006**, *442*, 368-373.

6. Prakash, M.; Gershenfeld, N., Microfluidic Bubble Logic. *Science* **2007**, *315*, 832-835.

7. Taylor, C. A.; Draney, M. T., Experimental and Computational Methods in Cardiovascular Fluid Mechanics. *Annu Rev Fluid Mech* **2004**, *36*, 197-231.

8. Lohse, D., Bubble Puzzles. *Phys Today* **2003**, *56*, 36-41.

9. Chen, K. J., et al., Hyperthermia-Mediated Local Drug Delivery by a Bubble-Generating Liposomal System for Tumor-Specific Chemotherapy. *Acs Nano* **2014**, *8*, 5105-5115.

10. Preuss, M.; Butt, H. J., Direct Measurement of Particle-Bubble Interactions in Aqueous Electrolyte: Dependence on Surfactant. *Langmuir* **1998**, *14*, 3164-3174.

11. Ducker, W. A.; Xu, Z. G.; Israelachvili, J. N., Measurements of Hydrophobic and DLVO Forces in Bubble-Surface Interactions in Aqueous-Solutions. *Langmuir* **1994**, *10*, 3279-3289.

12. Preuss, M.; Butt, H. J., Direct Measurement of Forces between Particles and Bubbles. *Int J Miner Process* **1999**, *56*, 99-115.

13. Butt, H. J., A Technique for Measuring the Force between a Colloidal Particle in Water and a Bubble. *J Colloid Interf Sci* **1994**, *166*, 109-117.

14. Webber, G. B.; Edwards, S. A.; Stevens, G. W.; Grieser, F.; Dagastine, R. R.; Chan,

D. Y. C., Measurements of Dynamic Forces between Drops with the AFM: Novel Considerations in Comparisons between Experiment and Theory. *Soft Matter* **2008**, *4*, 1270-1278.

15. Edwards, S. A.; Carnie, S. L.; Manor, O.; Chan, D. Y. C., Effects of Internal Flow and Viscosity Ratio on Measurements of Dynamic Forces between Deformable Drops. *Langmuir* **2009**, *25*, 3352-3355.

16. Webber, G. B.; Manica, R.; Edwards, S. A.; Carnie, S. L.; Stevens, G. W.; Grieser, F.; Dagastine, R. R.; Chan, D. Y. C., Dynamic Forces between a Moving Particle and a Deformable Drop. *J Phys Chem C* **2008**, *112*, 567-574.

17. Tabor, R. F.; Grieser, F.; Dagastine, R. R.; Chan, D. Y. C., Measurement and Analysis of Forces in Bubble and Droplet Systems Using Afm. *J Colloid Interface Sci* **2012**, *371*, 1-14.

18. Vakarelski, I. U.; Lee, J.; Dagastine, R. R.; Chan, D. Y. C.; Stevens, G. W.; Grieser, F., Bubble Colloidal AFM Probes Formed from Ultrasonically Generated Bubbles. *Langmuir* **2008**, *24*, 603-605.

19. Manor, O.; Vakarelski, I. U.; Stevens, G. W.; Grieser, F.; Dagastine, R. R.; Chan, D. Y. C., Dynamic Forces between Bubbles and Surfaces and Hydrodynamic Boundary Conditions. *Langmuir* **2008**, *24*, 11533-11543.

20. Manor, O.; Vakarelski, I. U.; Tang, X.; O'Shea, S. J.; Stevens, G. W.; Grieser, F.; Dagastine, R. R.; Chan, D. Y. C., Hydrodynamic Boundary Conditions and Dynamic Forces between Bubbles and Surfaces. *Phys Rev Lett* **2008**, *101,* 024501.

21. Tabor, R. F.; Manica, R.; Chan, D. Y. C.; Grieser, F.; Dagastine, R. R., Repulsive van Der Waals Forces in Soft Matter: Why Bubbles Do Not Stick to Walls. *Phys Rev Lett*

2011, *106,* 064501.

22. Krasowska, M.; Carnie, S. L.; Fornasiero, D.; Ralston, J., Ultrathin Wetting Films on Hydrophilic Titania Surfaces: Equilibrium and Dynamic Behavior. *J Phys Chem C* **2011**, *115*, 11065-11076.

23. Shi, C.; Cui, X.; Xie, L.; Liu, Q. X.; Chan, D. Y. C.; Israelachvili, J. N.; Zeng, H. B., Measuring Forces and Spatiotemporal Evolution of Thin Water Films between an Air Bubble and Solid Surfaces of Different Hydrophobicity. *Acs Nano* **2015**, *9*, 95-104.

24. Tabor, R. F.; Lockie, H.; Mair, D.; Manica, R.; Chan, D. Y. C.; Grieser, F.; Dagastine, R. R., Combined AFM-Confocal Microscopy of Oil Droplets: Absolute Separations and Forces in Nanofilms. *J Phys Chem Lett* **2011**, *2*, 961-965.

25. Frostad, J. M.; Collins, M. C.; Leal, L. G., Cantilevered-Capillary Force Apparatus for Measuring Multiphase Fluid Interactions. *Langmuir* **2013**, *29*, 4715-4725.

26. Derjaguin, B.; Kussakov, M., Anomalous Properties of Thin Polymolecular - Films V an Experimental Investigation of Polymolecular Solvate (Adsorbed) Films as Applied to the Development of a Mathematical Theory of the Stability of Colloids. *Acta Physicochim Urs* **1939**, *10*, 153-174.

27. Fisher, L. R.; Mitchell, E. E.; Hewitt, D.; Ralston, J.; Wolfe, J., The Drainage of a Thin Aqueous Film between a Solid-Surface and an Approaching Gas Bubble. *Colloids Surf* **1991**, *52*, 163-174.

28. Pushkarova, R. A.; Horn, R. G., Bubble-Solid Interactions in Water and Electrolyte Solutions. *Langmuir* **2008**, *24*, 8726-8734.

29. Connor, J. N.; Horn, R. G., The Influence of Surface Forces on Thin Film Drainage between a Fluid Drop and a Flat Solid. *Faraday Discuss* **2003**, *123*, 193-206.

30. Platikanov, D., Experimental Investigation on Dimpling of Thin Liquid Films. *J Phys Chem-Us* **1964**, *68*, 3619-3624.

31. Pan, L.; Jung, S.; Yoon, R. H., Effect of Hydrophobicity on the Stability of the Wetting Films of Water Formed on Gold Surfaces. *J Colloid Interf Sci* **2011**, *361*, 321-330.

32. Niecikowska, A.; Krasowska, M.; Ralston, J.; Malysa, K., Role of Surface Charge and Hydrophobicity in the Three-Phase Contact Formation and Wetting Film Stability under Dynamic Conditions. *J Phys Chem C* **2012**, *116*, 3071-3078.

33. Malysa, K.; Krasowska, M.; Krzan, M., Influence of Surface Active Substances on Bubble Motion and Collision with Various Interfaces. *Adv Colloid Interface Sci* **2005**, *114*, 205-225.

34. Zawala, J.; Malysa, K., Influence of the Impact Velocity and Size of the Film Formed on Bubble Coalescence Time at Water Surface. *Langmuir* **2011**, *27*, 2250-2257.

35. Hendrix, M. H. W.; Manica, R.; Klaseboer, E.; Chan, D. Y. C.; Ohl, C. D., Spatiotemporal Evolution of Thin Liquid Films During Impact of Water Bubbles on Glass on a Micrometer to Nanometer Scale. *Phys Rev Lett* **2012**, *108,* 247803.

36. Manica, R.; Klaseboer, E.; Chan, D. Y. C., The Impact and Bounce of Air Bubbles at a Flat Fluid Interface. *Soft Matter* **2016**, *12*, 3271-3282.

37. Wang, L.; Sharp, D.; Masliyah, J.; Xu, Z., Measurement of Interactions between Solid Particles, Liquid Droplets, and/or Gas Bubbles in a Liquid Using an Integrated Thin Film Drainage Apparatus. *Langmuir* **2013**, *29*, 3594-3603.

38. Zhang, X.; Tchoukov, P.; Manica, R.; Wang, L.; Liu, Q.; Xu, Z., Simultaneous Measurement of Dynamic Force and Spatial Thin Film Thickness between Deformable and Solid Surfaces by Integrated Thin Liquid Film Force Apparatus. *Soft Matter* **2016**, *12*,

9105-9114.

39. Manica, R.; Connor, J. N.; Carnie, S. L.; Horn, R. G.; Chan, D. Y. C., Dynamics of Interactions Involving Deformable Drops: Hydrodynamic Dimpling under Attractive and Repulsive Electrical Double Layer Interactions. *Langmuir* **2007**, *23*, 626-637.

40. Manica, R.; Parkinson, L.; Ralston, J.; Chan, D. Y. C., Interpreting the Dynamic Interaction between a Very Small Rising Bubble and a Hydrophilic Titania Surface. *J Phys Chem C* **2010**, *114*, 1942-1946.

41. Chan, D. Y. C.; Klaseboer, E.; Manica, R., Theory of Non-Equilibrium Force Measurements Involving Deformable Drops and Bubbles. *Adv Colloid Interface Sci* **2011**, *165*, 70-90.

42. Verwey, E. J. W.; Overbeek, J. T. G., *Theory of the Stability of Lyophobic Colloids*; Elsevier: Amsterdam, 1948.

43. Butt, H. J.; Cappella, B.; Kappl, M., Force Measurements with the Atomic Force Microscope: Technique, Interpretation and Applications. *Surf Sci Rep* **2005**, *59*, 1-152.

44. Israelachvili, J. N., *Intermolecular and Surface Forces*; Academic Press: London, 1992.

45. Hewitt, D.; Fornasiero, D.; Ralston, J.; Fisher, L. R., Aqueous Film Drainage at the Quartz Water Air Interface. *J Chem Soc Faraday T* **1993**, *89*, 817-822.

46. Visser, J., On Hamaker Constants: A Comparison between Hamaker Constants and Lifshitz-van Der Waals Constants. *Adv Colloid Interface Sci* **1972**, *3*, 331-363.

47. Li, C.; Somasundaran, P., Role of Electrical Double-Layer Forces and Hydrophobicity in Coal Flotation in Nacl Solutions. *Energ Fuel* **1993**, *7*, 244-248.

48. Yiantsios, S. G.; Davis, R. H., On the Buoyancy-Driven Motion of a Drop Towards

a Rigid Surface or a Deformable Interface. *J Fluid Mech* **1990**, *217*, 547-573.

49. Shahalami, M.; Wang, L. X.; Wu, C.; Masliyah, J. H.; Xu, Z. H.; Chan, D. Y. C., Measurement and Modeling on Hydrodynamic Forces and Deformation of an Air Bubble Approaching a Solid Sphere in Liquids. *Adv Colloid Interface Sci* **2015**, *217*, 31-42.

50. Klaseboer, E.; Manica, R.; Chan, D. Y. C., Universal Behavior of the Initial Stage of Drop Impact. *Phys Rev Lett* **2014**, *113,* 194501.

51. Manica, R.; Hendrix, M. H. W.; Gupta, R.; Klaseboer, E.; Ohl, C. D.; Chan, D. Y. C., Modelling Bubble Rise and Interaction with a Glass Surface. *Appl Math Model* **2014**, *38*, 4249-4261.

52. Klaseboer, E.; Chevaillier, J. P.; Gourdon, C.; Masbernat, O., Film Drainage between Colliding Drops at Constant Approach Velocity: Experiments and Modeling. *J Colloid Interface Sci* **2000**, *229*, 274-285.

53. Bouwhuis, W.; van der Veen, R. C. A.; Tran, T.; Keij, D. L.; Winkels, K. G.; Peters, I. R.; van der Meer, D.; Sun, C.; Snoeijer, J. H.; Lohse, D., Maximal Air Bubble Entrainment at Liquid-Drop Impact. *Phys Rev Lett* **2012**, *109,* 264501.

54. Berry, J. D.; Dagastine, R. R., Mapping Coalescence of Micron-Sized Drops and Bubbles. *J Colloid Interf Sci* **2017**, *487*, 513-522.

Chapter 5 Study of interactions between an air-bubble and hydrophobic flat solid surfaces using an integrated thin liquid film force apparatus (ITLFFA)

5.1 Introduction

Interest in understanding the boundary conditions at solid-liquid interfaces has been growing in the past decades, especially for systems of micro/nano length scales[1-2]. Determining the actual boundary conditions at the solid-liquid interface is not only essential in fundamental research in fluid dynamics, but also of great importance in applications of fluid dynamics dominant systems. The drag reduction that allows energy saving is attributed to the mobile boundary condition at the solid-liquid interface, which is of paramount importance in microfluidics, confined biological systems, and the permeability of microporous media[3-4]. Despite the debate on the occurrence of mobile behavior at the solid-liquid interface, the mobile boundary condition has been observed experimentally[5-9] and predicted theoretically[10-13]. Generally, the degree of mobile boundary condition at the surface is indicated by the slip length, defined as the distance inside the solid surface at which the velocity extrapolates linearly to zero. Thus, various techniques have been used to measure the slip length.

The earliest technique of investigating the slip length was the capillary method[14-15]. In this method, a liquid in a thin capillary was driven by external pressure at one end and the slip length was obtained by measuring the pressure drop between the two ends of the capillary and the flow rate. This method is easy to use but accurate measurement of the pressure drop is difficult. Direct measurement of the slip length can be done using the fluid flow tracing method, which uses either optical traceable particles or fluorescent molecules as velocity probes to determine the velocity profiles. The slip length varying from tens of nanometers to a few microns of silane has been measured by particle image velocimetry for hydrophobic surface grafted with a monolayer [16-17]. Using this technique, the slip length

of a superhydrophobic surface was found to be a few microns[18]. The fluorescent recovery technique was first used to measure the local velocity of a sheared polymer melt from a solid-liquid interface[19]. Since then, slip lengths in the order of several tens of nanometers have been detected using this technique for the hydrophobic surface[7, 20].

At present, the most popular method of measuring the slip length at a solid-liquid interface is the liquid drainage method using surface force apparatus (SFA) and atomic force microscopy (AFM). In this method, the hydrodynamic force between two solid surfaces as a function of separation distance is measured when the two surfaces approach each other at a given relative velocity. The slip length is obtained indirectly by fitting the measured hydrodynamic force rather than from the visualization of the flow profile. In SFA, the hydrodynamic force was measured between two cross cylindrical surfaces and the separation distance was accurately determined by the fringes of equal chromatic order. Using SFA, Zhu et al. investigated the boundary condition between two smooth hydrophobic surfaces[5]. They observed a large shear-dependent slip length up to a few microns. In their follow up work, the effect of surface roughness on slip boundary condition was studied and the increasing roughness was shown to decrease the degree of slip[21]. A smaller slip length of 20 nm was detected between two smooth hydrophobic surfaces using the same technique and the large slip length reported earlier was attributed to the contamination from the hydrophobic surfaces[22]. Because of the relatively large contact region in SFA experiments, the system is more sensitive to contaminations that will result in measurement errors. In contrast to SFA, the hydrodynamic force was measured between a sphere and a planar surface in AFM. The small contact area in the order of square nanometers improves the accuracy of measurements at nanoscales. The shear-dependent

slip length up to hundreds of nanometers was observed in AFM experiments[23-25]. In the measurements using AFM, the boundary slip was found to increase with increasing surface roughness that was opposite to the results in SFA experiments[26]. Recently, AFM has been widely used to study the effect of nanobubbles on the boundary slip[27-28]. In general, the slip is related to the coverage of nanobubbles on the surface. It is evident from the existing literature that, on the experimental side, there is no consensus on the magnitude of the boundary slip on hydrophobic surfaces even measured using the same technique. Therefore, new data preferably obtained with new experimental techniques for the same systems over a wider range of hydrodynamic conditions are necessary.

Here, we report a new approach for investigating the hydrodynamic boundary condition based on the measurement of the liquid drainage dynamics. In reality, hydrophobic surfaces are not smooth in molecular level, such as the hydrophobic/hydrophobized mineral particles in flotation cell. The boundary condition of aqueous solutions on these hydrophobic surfaces that possess surface roughness under different hydrodynamic conditions is of great importance. Thus, in this study, hydrophobic surfaces with nanoroughness were made to mimic the surfaces in practice. The evolution of spatiotemporal film thickness between an air bubble and these surfaces with different hydrophobicities was measured under different bubble approach velocities. The measured film profiles were fitted with a modified Stokes-Reynolds-Young-Laplace (SRYL) model to obtain the mobility of the hydrophobic surfaces, which qualitatively indicated as slip lengths in the model. The feasibility of our instrument-integrated thin liquid film force apparatus (ITLFFA)[29] allows us to obtain accurate film profiles to deduce the degree of surface mobilitiy.

5.2 Materials and methods

5.2.1 Materials

Water with a resistivity of 18.2 MΩ cm and Viscosity 0.89 mPa·s at 25 °C， purified by Milli-Q was used in all the experiments. Dimethyldichlorosilane (DMDCS, 99+%) purchased from Acros Organics was used as silane coupling reagent for hydrophobizing silica surfaces. Toluene (HPLC grade) and sulfuric acid (ACS Plus) supplied by Fisher Scientific, hydrogen peroxide aqueous solution (30% w/w, ACS grade) obtained from the Ricca Chemical Company and anhydrous ethyl alcohol acquired from Commercial Alcohols were used as received for various purposes. Prior to its use, potassium chloride (KCl) of ACS grade, purchased from Fisher Scientific was recrystallized and then calcined in an oven at 550 °C for 8 h to remove any impurities. Fused silica windows purchased from Edmund Optics were used as solid surfaces. The glass capillary obtained from Fisher Scientific with an inner diameter of 1.10 ± 0.05 mm was used to generate and hold air bubbles.

5.2.2 Preparation of hydrophobic surfaces

The fused silica surfaces as received were first soaked in freshly prepared piranha solution (3:1 of H_2SO_4:H_2O_2 by volume) for one hour and rinsed with a large amount of Milli-Q water to remove any possible contaminants. To hydrophobize the fused silica surface by silanation reaction, 0.824 mmol/L DMDCS in toluene solution was prepared. The cleaned fused silica was immersed into the DMDCS solution for 5 s and 30 min to obtain surfaces with water contact angle 36° and 90°, respectively. The surfaces silanized as such were rinsed with toluene, anhydrous ethyl alcohol and water in sequence to remove unbound

residual DMDCS. The smooth surface with designed hydrophobicity was successfully prepared after drying with nitrogen flow.

5.2.3 Contact angle measurement

The water contact angles on the hydrophobized silica surfaces were measured in air using a Theta Optical Tensiometer T200 (Biolin Scientific, Stockholm, Sweden). For each measurement, a water droplet of volume of 2 μL was deposited on the surface and brought into focus. The droplet profile was recorded and the contact angle was determined with the Theta software (Appendix C Figure C2).

5.2.4 Surface characterization

The roughness of the hydrophobized silica surfaces was determined by Dimension Icon Atomic Force Microscope (AFM) (Bruker Dimension Icon-PT). The surfaces were imaged by AFM tapping mode in air (Appendix C Figure C3). As shown in Table 5-1, the root mean square (RMS) roughness determined to be around 0.6 nm from these images did not change by silanation reactions while peak-to-valley roughness appeared to increase from 8.8 nm to 15.3 nm.

Table 5-1. Surface properties of the investigated surfaces.

Contact angle	RMS roughness (nm)	Peak-to-valley roughness (nm)
0°	0.636	8.8
36°	0.553	13.4
90°	0.608	15.3

5.3 Experimental

The spatiotemporal film thickness and the dynamic interaction forces between a hydrophobic surface and an approaching air bubble were measured simultaneously by integrated thin liquid film force apparatus (ITLFFA). Hydrophobic surfaces with nanoroughness and water contact angles 36° and 90° were investigated in our work. As shown in Figure 5-1, the air bubble of radius $R = 1.2$ mm is created from a gas-tight syringe at one end of the capillary connected to a motorized actuator (THORLABS, Z825B) that can move upward and downward with a step size of 20 nm. The air bubble remained pinned to the capillary over the entire process at an angle of $\theta \sim 150°$ with a constant volume. In each experiment, the initial separation between the bubble and the studied fused silica surface was fixed to 300 μm, then the bubble approached to the fused silica surface with the total displacement of 400 μm. Thus, the overlap between the bubble and fused silica surfaces was about 100 μm for all the experiments to facilitate the comparison of experimental results. After stopping moving, the bubble was held at the same position for a few seconds and then retracted from the surface with the same velocity. In this study, three bubble approach velocities of 0.01 mm/s, 0.1 mm/s and 1 mm/s were mainly investigated, which were maximum bubble approach velocities put in the settings of the motorized actuator. The displacement of the bubble during the entire approach process can be recorded separately by displacement sensor with a precision of 5 μm, allowing to compute the velocity of the bubble as it approached to the fused silica surface (Appendix Figure C1). The thorough detailed description of ITLFFA can be found elsewhere[29].

The interaction forces between the bubble and the fused silica surfaces were measured using a bimorph as a force sensor. Meanwhile, the absolute thickness of the intervening

liquid film between the air bubble and hydrophobic surface at the film rupture was determined using white light interferometry[30-31]. The film profiles before the rupture were obtained by counting back recorded frames to determine the interference order at the barrier rim of the film. Each experiment was repeated for at least 5 times to confirm the accuracy of measurement.

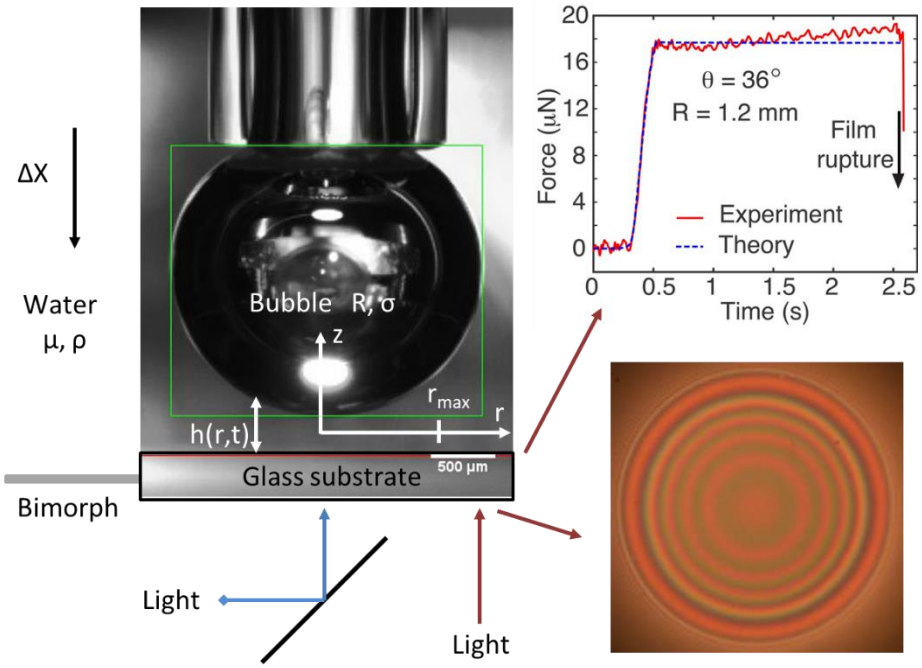

Figure 5-1. Images of simultaneous measurements of interaction forces and film thickness (including bubble photograph and force curve) for a bubble of radius $R = 1.2\,mm$ and interfacial tension σ in a liquid of density ρ and viscosity μ. The bubble is held by a capillary which is driven with precision towards (or away from) a glass substrate that is attached to a bimorph with known spring constant K. The deformation of the bimorph is used to determine directly the interaction force between the air bubble and the fused silica substrate (top right panel). The interference fringes (bottom right) are then used to extract the time evolution of the spatial thickness of the intervening liquid film, $h(r,t)$.

5.4 Theoretical model

A theoretical approach based on lubrication theory for the thin liquid film drainage is employed in combination with the Young-Laplace equation for the shape of the bubble. We account for the possibility of slip boundary condition using the form $u = b(\frac{du}{dz})$, where u is the radial component of the velocity, z is the direction that perpendicular to the fused silica surface as shown in Figure 5-1, b is the slip length as an indicator of surface mobility in our study.

Under these assumptions, the temporal film thickness $(\frac{\partial h}{\partial t})$ of the liquid from the film between the bubble and hydrophobic surface in reference to Figure 1 is given by the Stokes-Reynolds equation as[32]:

$$\frac{\partial h}{\partial t} = \frac{1}{12\mu r}\frac{\partial}{\partial r}\left(rh^3\frac{\partial p}{\partial r}\right) + \frac{1}{4\mu r}\frac{\partial}{\partial r}\left(\frac{r[(b_1+b_2)h^3+4b_1b_2h^2]}{h+b_1+b_2}\frac{\partial p}{\partial r}\right) \quad (5\text{-}1)$$

where b_1 and b_2 represent the degree of surface mobility at the bubble-liquid and solid-liquid interface, respectively and μ is viscosity of the aqueous solution. With the tangential immobile boundary condition at both the bubble-liquid and solid-liquid interface ($b_1 = 0, b_2 = 0$), the last term of eqn (5-1) vanishes. If one of the interfaces is fully mobile while the other is tangential immobile, eqn (5-1) converges to the form:

$$\frac{\partial h}{\partial t} = \frac{1}{3\mu r}\frac{\partial}{\partial r}\left(rh^3\frac{\partial p}{\partial r}\right) \quad (5\text{-}2)$$

However, for partially mobile interface, the value of b_1 and b_2 was fitted to quantify the degree of surface mobility.

The excess pressure p in the film, relative to the pressure in the bulk liquid, is given by the Young-Laplace equation that depends on the curvature of the air-liquid interface[32]:

$$\frac{\sigma}{r}\frac{\partial}{\partial r}\left(r\frac{\partial h}{\partial r}\right) = \frac{2\sigma}{R} - p - \Pi \quad (5\text{-}3)$$

where $\frac{2\sigma}{R}$ is the Laplace pressure and Π is the disjoining pressure. The disjoining pressure becomes important at the last stage of film drainage where the surface forces become dominant and is responsible for the final state of the film, either a stable film if repulsive or rupture of the film if it is attractive.

To complete the model we need four boundary conditions and one initial condition given by $h(r,0) = h_0 + r^2/(2R)$, where h_0 is the initial gap between the bubble and solid surface. Due to the symmetry $\frac{\partial h}{\partial r} = \frac{\partial p}{\partial r} = 0$ applies at $r = 0$. The pressure decay as $p \sim r^{-4}$ outside the interaction region at $r > r_{max}$[33]. The following equation is used as another boundary condition to take into account the deformation of the bubble at constant volume and the deflection of the solid surface attached to the bimorph (last term of eqn (5-4))[34]:

$$\frac{dh}{dt} = \frac{dX}{dt} - \frac{1}{2\pi\sigma}\frac{dF}{dt}\left[\log\left(\frac{r_{max}}{2R}\right) + 1 + \frac{1}{2}\log\left(\frac{1+cos\theta}{1-cos\theta}\right) - \frac{2\pi\sigma}{K}\right] \quad (5\text{-}4)$$

where $\frac{dX}{dt}$ is the velocity of the approaching air bubble, θ is the angle that the bubble is pinned at the end of the capillary. This boundary condition provides numerical results that are independent of the size of the computational domain as long as it is larger than the interaction zone but smaller than the radius of the bubble. The force acting on the bubble is then obtained by integrating the total pressure:

$$F(t) = 2\pi \int_0^\infty (p + \Pi) r dr \equiv 2\pi \int_0^{r_{max}} [p(r,t) + \Pi(h(r,t))] r dr \quad (5\text{-}5)$$

Outside the computational domain at $r > r_{max}$, hydrodynamic and disjoining pressures can be considered negligible. The model is solved numerically using a standard ODE solver in Matlab. Details of the numerical implementation can be found elsewhere[32, 34].

5.5 Results and discussion

In this section, the evolution of film profiles between a bubble and solid surfaces with different hydrophobicities under different approach velocities are obtained by the ITLFFA. By fitting the measured film profiles using the SRYL model, the mobility of hydrophobic surface for each condition is determined and possible mechanisms for this phenomenon are discussed.

5.5.1 Effect of hydrophobicity

For a given maximum approach velocity of 1 mm/s, the evolution of film profiles between the air bubble and fused silica surfaces of three different water contact angles are shown in Figure 5-2. When the bubble approached the hydrophilic surface (Figure 5-2a), the pressure in the film exceeded the Laplace pressure of the bubble at the film thickness of 2200 nm, resulting in a local change of bubble curvature that led to dimple formation. The dimple then became increasingly more pronounced as the film expanded and drained to a stable flat film at the end[35]. In the current study, everything is kept identical from the experiment of hydrophilic case except for the surfaces of increasing hydrophobicity. The evolution of film profile between the bubble and hydrophobic surface showed completely different behavior from that of hydrophilic surface as outlined below:

(1) The dimple for the hydrophobic surfaces formed at much thinner film thickness than that for the hydrophilic case. When the contact angle of the surface was 36^{o}, the dimple formed at the thickness of 1750 nm (Figure 5-2b) which decreased to around 1000 nm (Figure 5-2c) when the contact angle of the surface increased to 90^{o}, representing half of the film thickness value of the hydrophilic case. Thus, the

film thickness of the dimple formation decreased with increasing hydrophobicity of solid surfaces.

(2) The liquid in the film drained much faster in the hydrophobic case than that in the hydrophilic case (Figure 5-3), which was also observed by Fisher et al.[36]. The drainage rate of the liquid film increased with increasing hydrophobicity of the surface. For hydrophilic case, the film drained for around 2 minutes to reach the flat stable film. In contrast, the film drained for only 8 s before rupture when the surface became a little hydrophobic with a water contact angle of 36°. The drainage time decreased further to about 1 s when the water contact angle of the fused silica surface increased to 90°.

(3) Unlike the hydrophilic surface that formed a flat stable film, the rupture of the film was observed in every experimental run for hydrophobic surface. Film rupture generally occurred at the barrier rim where the film thickness was minimal. The rupture started at one point and expanded to the whole film within a few milliseconds, resulting in the adhesion of the bubble to the fused silica surface.

The smaller thickness of initial dimple formation and fast drainage rate when a bubble interacts with a hydrophobic surface inspired us to consider the possibility of mobile boundary condition at hydrophobic surfaces.

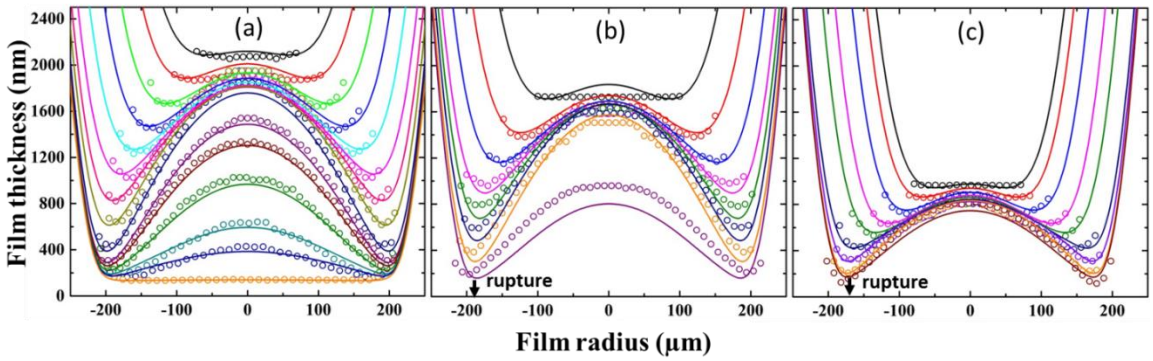

Figure 5-2. Comparison between theory (solid lines) and experimental results (open circles) for the evolution of spatiotemporal film thickness when an air bubble of radius $R = 1.2\ mm$ approached (a) a hydrophilic surface (Measurement times from top to bottom: 0.377, 0.392, 0.412, 0.437, 0.467, 0.507, 0.567, 0.687, 1.197, 2.912, 4.542, 9.075, 18.610, 28.124 and 101.755 s), (b) and (c) a hydrophobic surface with water contact angle 36° (Times: 0.377, 0.419, 0.457, 0.505, 0.571, 0.705, 1.209 and 8.099 s) and 90° (Times: 0.377, 0.385, 0.400, 0.422, 0.443, 0.490, 0.548, 0.865 and 1.621 s), respectively, in 10^{-5} M KCl solutions. In all the cases, the maximum bubble approach velocity was set to be 1 mm/s. The arrows indicate the last film profile of film rupture at the barrier rim for hydrophobic surfaces.

5.5.2 Effect of approach velocity

Since our ITLFFA has the specific feature that allows conducting measurements under a wide range of hydrodynamic conditions, the effect of approach velocity on the surface mobility was also investigated for the hydrophobic surfaces. The evolution of film profiles when the bubble approached the hydrophobic surface with a water contact angle 90° at approach velocities of 0.01 mm/s, 0.1 mm/s and 1 mm/s in 10^{-5} M and 0.1 M KCl solutionz is shown in Figure 5-4.

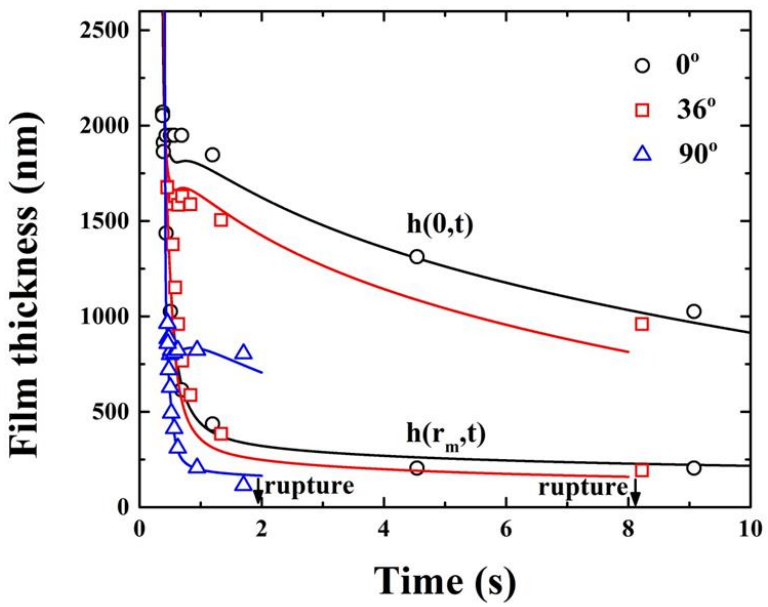

Figure 5-3. Comparison between theory (solid line) and experimental results (open symbols) for the film thickness at the center ($h(0,t)$) and the barrier rim ($h(r_m,t)$) for the hydrophilic and hydrophobic cases in Figure 5-2.

According to previous study for hydrophilic surface[35], high approach velocity promoted dimple formation and the thickness that the dimple appeared, which is defined as the film thickness of initial dimple formation (h_d), increased with increasing approach velocity. The experimental data for the hydrophobic case showed the same trend (Figure 5-4). However, compared to the hydrophilic case, the h_d was the same for approach velocity of 0.01 mm/s, while it decreased with increasing the approach velocity to 0.1 mm/s and 1 mm/s, indicating predominate effect of surface hydrophobicity on dimple formation at higher bubble approach velocities. For the hydrophobic surface, the film ruptured with smaller width for lower bubble approach velocity than for the case of higher bubble approach velocity, although the overlap was the same for all the experiments which should result in the same film width. This finding indicates that the film ruptured before the bubble stopped moving at low approach velocity.

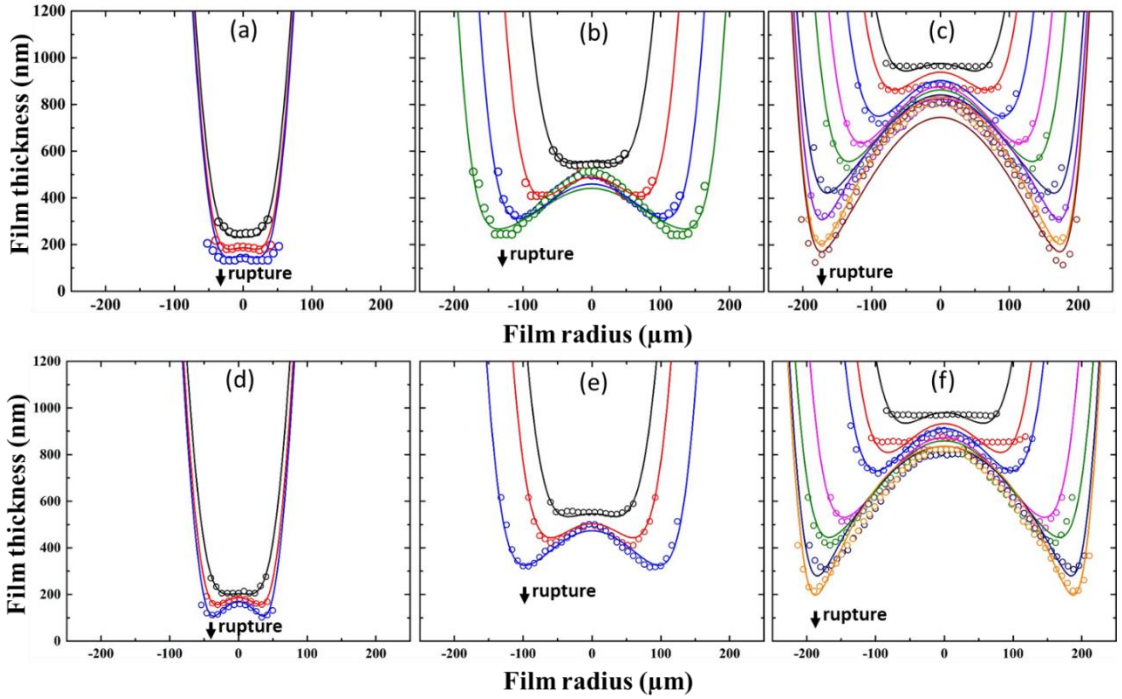

Figure 5-4. Comparison between theory (solid lines) and experimental results (open circles) for the evolution of spatiotemporal film thickness when an air bubble of radius 1.2 mm approaching a hydrophobic surface with water contact angle 90° in 10^{-5} M KCl solution (a, b and c) and 0.1 M KCl solution (d, e and f) with a bubble approach velocity of: (a) 0.01 mm/s (Measurement times from top to bottom: 34.982, 35.285 and 35.702 s), (b) 0.1 mm/s (Times: 3.311, 3.466, 3.691 and 3.921 s), (c) 1 mm/s (Times: 0.377, 0.385, 0.400, 0.422, 0.443, 0.490, 0.548, 0.865 and 1.621 s), (d) 0.01 mm/s (Times: 34.982, 35.302 and 35.910 s), (e) 0.1 mm/s (Times: 3.311, 3.399 and 3.612 s) and (f) 1 mm/s (Times: 0.377, 0.392, 0.403, 0.453, 0.485, 0.564 and 0.688 s. The arrows indicate that the film ruptured at the barrier rim.

5.5.3 Surface mobility

As discussed in our previous work for hydrophilic surface[35], the film thickness of dimple formation h_d is a function of approach velocity. Therefore one anticipates that the similar

dimple height and the evolution of film profile if the bubble approach velocity remains the same. The change of h_d and the fast drainage rate for hydrophobic surface inspired us to account for the possibility of mobile boundary condition at the air-liquid interface or/and the solid-liquid interface. In Figure 5-5, h_d was plotted as a function of approach velocity (represented by the Capillary number $Ca = \frac{\mu v}{\sigma}$) for different hydrophobic surfaces. According to our previous work[35], h_d can be expressed as $h_d = 0.49RCa^{1/2}$ with tangential immobile boundary condition. If one interface is fully mobile and the other one is immobile, h_d is given by $h_d = 0.49R(\frac{Ca}{4})^{1/2}$. For the case of hydrophilic surface, an excellent agreement between the theory and experimental data was achieved by assuming immobile boundary condition for both interfaces. For hydrophobic surfaces, the experimental film thickness of dimple formation fell between the no-slip and full slip boundary conditions of one interface, indicating a partial mobile boundary condition at the solid-water interface as the bubble boundary condition should not be affected by the change of solid surfaces. For the hydrophobic surface of relatively low surface hydrophobicity, the surfacemobility occurred when the approach velocity exceeded 0.1 mm/s. For the surface of higher hydrophobicity, the surface mobility appeared at approach velocity as low as 0.02 mm/s. From our experimental results, it is evident that the surface mobility not only depends on hydrophobicity of the surface but is also related to the relative velocity between the two approaching surfaces. The no-slip boundary condition for air-liquid and solid-liquid interface has been verified by previous experimental data for the bubble approaching a hydrophilic surface over the similar bubble approaching velocity range[35]. Since the only change in this study was the solid surface from hydrophilic to hydrophobic, the no-slip boundary condition should still apply to the air-liquid interface. We also notice that Peclet

number, $Pe = \lambda^2/D\tau$, where λ is a characteristic length in the radial direction, τ is a characteristic time and D is the diffusion coefficient of surface species, was critical in this dynamic drainage process[37-38]. In our system, Peclet number is around 100, which indicated that the convective transport of the liquid was larger than the diffusive transport when the surface gradient existed on the air-liquid interface. The large Peclet number also results in faster drainage of the liquid film. However, if this is the case, it should happen in the hydrophilic case as well. In the hydrophilic case, the no-slip boundary condition well explained the experimental behavior, excluding the presence of surface gradient at the air-liquid interface. Hence, we speculated that the apparent mobile boundary condition occurs at the hydrophobic surface to facilitate the drainage of liquid through the thin film, leading to a faster thinning rate.

In the following analysis, we introduced the slip length at hydrophobic surface in the theoretical model (eqns (5-1)-(5-5)) to fit the experimental film profiles, which qualitatively demonstrated the degree of mobility at partially mobile surfaces. Guided by the discussions mentioned above, we assume that the system remains axisymmetric and the bubble has tangentially immobile boundary condition ($b_1 = 0$), which means $u = 0$ at the bubble-liquid interface. The good agreement between the theory and experimental data shown in both Figure 5-2 and Figure 5-4 validates the existence of surface mobility for the solid-liquid interface. With the maximum approach velocity of 1 mm/s, the value of the slip length that provided the best agreement between the theory and experimental data was 150 nm for the hydrophobic surface with contact angle 36° (Figure 5-2b). However, eqn (5-2) was used to get the best prediction of the film profile evolution from the theoretical model for surface with the contact angle 90°, indicating a fully mobile surface under this

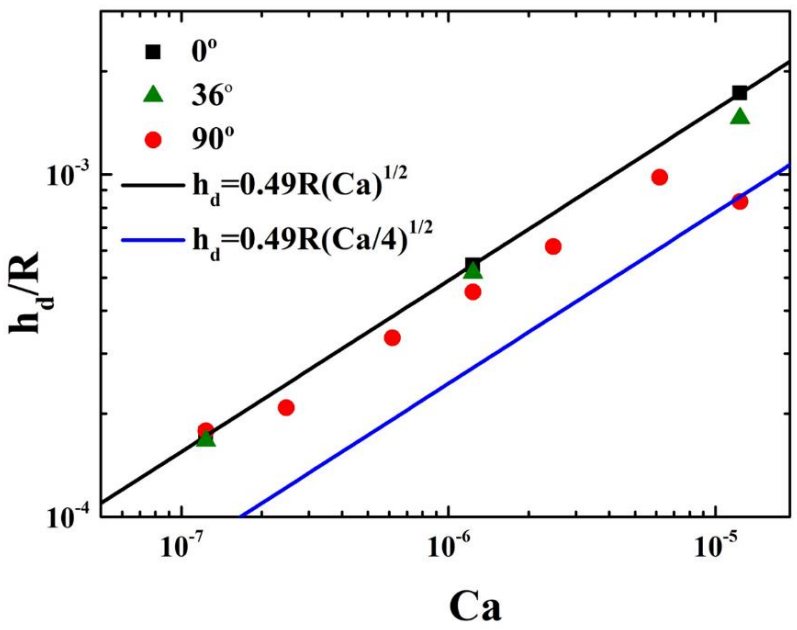

Figure 5-5. Experimental variation of the h_d with capillary number for solid surfaces with different hydrophobicities. Results assuming no-slip and full slip boundary conditions of one interface were calculated from the theoretical model (solid lines).

condition. Thus, the increase in surface hydrophobicity of solids dramatically increased the slip of water on the solid surface and facilitated the movement of liquid close to the liquid-solid interface. The slip lengths of the surface with contact angle 36° and 90° at other approach velocities were obtained using the same method. The fitted slip lengths were plotted as a function of bubble approach velocity (represented by Ca) as shown in Figure 5-6. In general, the slip length increased with increasing approach velocity for a hydrophobic surface with a given water contact angle. For a given approach velocity, the slip length increased with increasing surface hydrophobicity. The critical approach velocity at which the slip length started to increase decreased with the increasing surface hydrophobicity, indicating that the surface with higher contact angle was more mobile than that with lower contact angle. Since the approach velocity is related to shear rate, this

behavior can be regarded as shear-dependent mobile boundary condition. It is interesting to note the similar trend of approach velocity dependent mobile boundary condition occurred in 0.1 M KCl solutions (Figure 5-4d-f) as in 10^{-5} M KCl solutions, indicating a general shear-dependent mobile boundary condition for hydrophobic surfaces with nanoroughness.

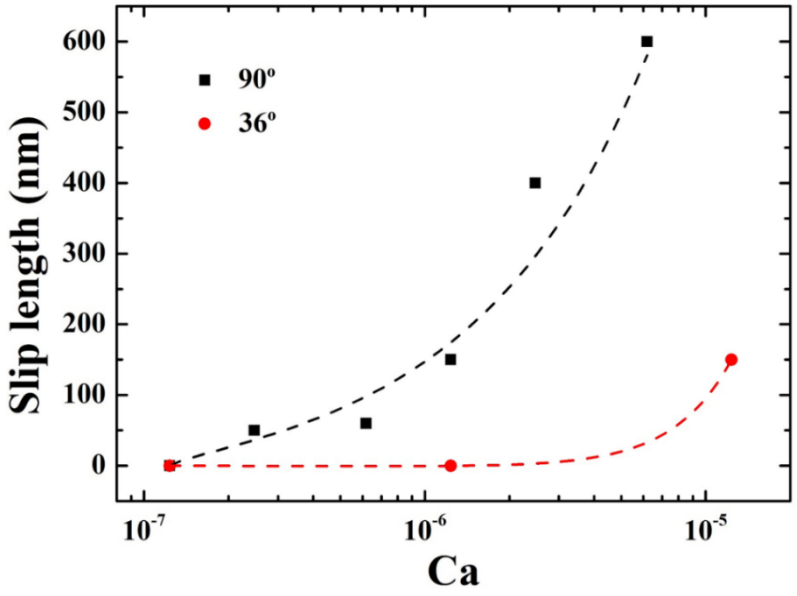

Figure 5-6. Dependence of fitted slip length on the approach velocity for an air bubble approaching two surfaces with different hydrophobicities. The dashed lines are used for eye guidance.

Compared with the slip length that was measured to be less than 100 nm at hydrophobic surface[16], the fitted slip lengths in our study are up to an order of magnitude larger than the length scale of the surface roughness, even larger at high shear rate with high surface hydrophobicity. These large slip lengths are similar with the results measured at the air-liquid interface for patterned superhydrophobic surface and for systems with nanobubbles on hydrophobic surfaces[28, 39]. The presence of nanobubble or air pockets on hydrophobic surfaces with nanoroughness has been verified by numerous researches as the surface

asperities provide more nucleation sites for nanobubbles or air pockets[40-42]. In this work, hydrophobic surfaces with the peak-to-valley roughness of around 15 nm were made, which provides large possibility of nanobubbles or air layer on the surface. The significant decrease of hydrodynamic drag forces was observed by Chan et. al on superhydrophobic surface with large scale roughness because of the existence of trapped air[43]. By adding surfactant, they showed that the hydrodynamic force increased which confirmed the mobility of trapped air on the rough surface. The shear-dependent surface mobility in this study can be attributed to the shear-induced nucleation of vapor bubbles on hydrophobic surfaces that has been proposed by de Gennes[5, 21] and supported by experiments conducted by Zhang et al.[44]. These shear-induced bubbles were fresh, unlike the bubble generated at the end of the capillary with immobile interface, leading to mobile boundary condition on the hydrophobic surfaces with nanoroughness. The high shear rate may increase the coverage of air layer on the surface of strong hydrophobicity, leading to a fully mobile boundary condition at the solid-liquid interface.

In addition, the rupture of the film occurred at the film thickness 100-200 nm in all cases. Assuming an attractive hydrophobic force as an exponential form reported previously[45], the model would require decay length of ~10 nm in this study that are much larger than the ones reported in literature (~0.8-1 nm). As discussed above, the air layer on the surfaces is believed to cause this large film rupture thickness that has been confirmed by early studies[46-48].

5.6 Conclusions

We have developed a new approach for determining the degree of surface mobility using the evolution of thin film profile when a bubble interacts with a flat surface. Unlike the no-slip boundary condition for hydrophilic surface, shear-dependent mobility was observed on the hydrophobic surface with nanoroughness, which is independent on the salt concentration of the solution. The change of boundary condition on these surfaces is believed to due to the presence of air pockets on such surfaces. Thus, surface roughness is a key feature that should be considered in practical dynamic interaction involving hydrophobic surfaces.

5.7 References

1. Cottin-Bizonne, C.; Barrat, J. L.; Bocquet, L.; Charlaix, E., Low-Friction Flows of Liquid at Nanopatterned Interfaces. *Nat Mater* **2003**, *2*, 237-240.

2. Karatay, E.; Haase, A. S.; Visser, C. W.; Sun, C.; Lohse, D.; Tsai, P. A.; Lammertink, R. G. H., Control of Slippage with Tunable Bubble Mattresses. *P Natl Acad Sci USA* **2013**, *110*, 8422-8426.

3. Majumder, M.; Chopra, N.; Andrews, R.; Hinds, B. J., Nanoscale Hydrodynamics - Enhanced Flow in Carbon Nanotubes. *Nature* **2005**, *438*, 44-44.

4. Bhushan, B., *Springer Handbook of Nanotechnology*, second ed.; Springer: Heidelberg, Germany, 2007.

5. Zhu, Y. X.; Granick, S., Rate-Dependent Slip of Newtonian Liquid at Smooth Surfaces. *Phys Rev Lett* **2001**, *87*, 096105.

6. Vinogradova, O. I.; Koynov, K.; Best, A.; Feuillebois, F., Direct Measurements of

Hydrophobic Slippage Using Double-Focus Fluorescence Cross-Correlation. *Phys Rev Lett* **2009**, *102*, 118302.

7. Pit, R.; Hervet, H.; Leger, L., Direct Experimental Evidence of Slip in Hexadecane: Solid Interfaces. *Phys Rev Lett* **2000**, *85*, 980-983.

8. Baudry, J.; Charlaix, E.; Tonck, A.; Mazuyer, D., Experimental Evidence for a Large Slip Effect at a Nonwetting Fluid-Solid Interface. *Langmuir* **2001**, *17*, 5232-5236.

9. Choi, C. H.; Kim, C. J., Large Slip of Aqueous Liquid Flow over a Nanoengineered Superhydrophobic Surface. *Phys Rev Lett* **2006**, *96*, 066001.

10. Thompson, P. A.; Troian, S. M., A General Boundary Condition for Liquid Flow at Solid Surfaces. *Nature* **1997**, *389*, 360-362.

11. Barrat, J. L.; Bocquet, L., Large Slip Effect at a Nonwetting Fluid-Solid Interface. *Phys Rev Lett* **1999**, *82*, 4671-4674.

12. Cieplak, M.; Koplik, J.; Banavar, J. R., Boundary Conditions at a Fluid-Solid Interface. *Phys Rev Lett* **2001**, *86*, 803-806.

13. de Gennes, P. G., On Fluid/Wall Slippage. *Langmuir* **2002**, *18*, 3413-3414.

14. Schnell, E., Slippage of Water over Nonwettable Surfaces. *J Appl Phys* **1956**, *27*, 1149-1152.

15. Churaev, N. V.; Sobolev, V. D.; Somov, A. N., Slippage of Liquids over Lyophobic Solid-Surfaces. *J Colloid Interf Sci* **1984**, *97*, 574-581.

16. Joseph, P.; Tabeling, P., Direct Measurement of the Apparent Slip Length. *Physical Review E* **2005**, *71*, 035303.

17. Tretheway, D. C.; Meinhart, C. D., Apparent Fluid Slip at Hydrophobic Microchannel Walls. *Phys Fluids* **2002**, *14*, L9-L12.

18. Joseph, P.; Cottin-Bizonne, C.; Benoit, J. M.; Ybert, C.; Journet, C.; Tabeling, P.; Bocquet, L., Slippage of Water Past Superhydrophobic Carbon Nanotube Forests in Microchannels. *Phys Rev Lett* **2006**, *97*, 156104.

19. Migler, K. B.; Hervet, H.; Leger, L., Slip Transition of a Polymer Melt under Shear-Stress. *Phys Rev Lett* **1993**, *70*, 287-290.

20. Lasne, D.; Maali, A.; Amarouchene, Y.; Cognet, L.; Lounis, B.; Kellay, H., Velocity Profiles of Water Flowing Past Solid Glass Surfaces Using Fluorescent Nanoparticles and Molecules as Velocity Probes. *Phys Rev Lett* **2008**, *100*, 214502.

21. Zhu, Y. X.; Granick, S., Limits of the Hydrodynamic No-Slip Boundary Condition. *Phys Rev Lett* **2002**, *88*, 106102.

22. Cottin-Bizonne, C.; Cross, B.; Steinberger, A.; Charlaix, E., Boundary Slip on Smooth Hydrophobic Surfaces: Intrinsic Effects and Possible Artifacts. *Phys Rev Lett* **2005**, *94*, 056102.

23. Zhu, L. W.; Neto, C.; Attard, P., Reliable Measurements of Interfacial Slip by Colloid Probe Atomic Force Microscopy. III. Shear-Rate-Dependent Slip. *Langmuir* **2012**, *28*, 3465-3473.

24. Neto, C.; Craig, V. S. J.; Williams, D. R. M., Evidence of Shear-Dependent Boundary Slip in Newtonian Liquids. *Eur Phys J E* **2003**, *12*, S71-S74.

25. Craig, V. S. J.; Neto, C.; Williams, D. R. M., Shear-Dependent Boundary Slip in an Aqueous Newtonian Liquid. *Phys Rev Lett* **2001**, *87*, 054504.

26. Bonaccurso, E.; Butt, H. J.; Craig, V. S. J., Surface Roughness and Hydrodynamic Boundary Slip of a Newtonian Fluid in a Completely Wetting System. *Phys Rev Lett* **2003**, *90*, 144501.

27. Wang, Y. L.; Bhushan, B.; Maali, A., Atomic Force Microscopy Measurement of Boundary Slip on Hydrophilic, Hydrophobic, and Superhydrophobic Surfaces. *J Vac Sci Technol A* **2009**, *27*, 754-760.

28. Li, D. Y.; Jing, D. L.; Pan, Y. L.; Bhushan, B.; Zhao, X. Z., Study of the Relationship between Boundary Slip and Nanobubbles on a Smooth Hydrophobic Surface. *Langmuir* **2016**, *32*, 11287-11294.

29. Zhang, X.; Tchoukov, P.; Manica, R.; Wang, L.; Liu, Q.; Xu, Z., Simultaneous Measurement of Dynamic Force and Spatial Thin Film Thickness between Deformable and Solid Surfaces by Integrated Thin Liquid Film Force Apparatus. *Soft Matter* **2016**, *12*, 9105-9114.

30. Butler, C. S.; Seeger, Z. L. E.; Bell, T. D. M.; Bishop, A. I.; Tabor, R. F., Local Determination of Thin Liquid Film Profiles Using Colour Interferometry. *Eur Phys J E* **2016**, *39*, 14.

31. Schilling, J.; Sengupta, K.; Goennenwein, S.; Bausch, A. R.; Sackmann, E., Absolute Interfacial Distance Measurements by Dual-Wavelength Reflection Interference Contrast Microscopy. *Phys Rev E* **2004**, *69*, 021901.

32. Chan, D. Y. C.; Klaseboer, E.; Manica, R., Film Drainage and Coalescence between Deformable Drops and Bubbles. *Soft Matter* **2011**, *7*, 2235-2264.

33. Yiantsios, S. G.; Davis, R. H., On the Buoyancy-Driven Motion of a Drop Towards a Rigid Surface or a Deformable Interface. *J Fluid Mech* **1990**, *217*, 547-573.

34. Chan, D. Y. C.; Klaseboer, E.; Manica, R., Theory of Non-Equilibrium Force Measurements Involving Deformable Drops and Bubbles. *Adv Colloid Interface Sci* **2011**, *165*, 70-90.

35. Zhang, X. R.; Manica, R.; Tchoukov, P.; Liu, Q. X.; Xu, Z. H., Effect of Approach Velocity on Thin Liquid Film Drainage between an Air Bubble and a Flat Solid Surface. *J Phys Chem C* **2017**, *121*, 5573-5584.

36. Fisher, L. R.; Mitchell, E. E.; Hewitt, D.; Ralston, J.; Wolfe, J., The Drainage of a Thin Aqueous Film between a Solid-Surface and an Approaching Gas Bubble. *Colloids Surf* **1991**, *52*, 163-174.

37. Manor, O.; Vakarelski, I. U.; Stevens, G. W.; Grieser, F.; Dagastine, R. R.; Chan, D. Y. C., Dynamic Forces between Bubbles and Surfaces and Hydrodynamic Boundary Conditions. *Langmuir* **2008**, *24*, 11533-11543.

38. Manor, O.; Vakarelski, I. U.; Tang, X. S.; O'Shea, S. J.; Stevens, G. W.; Grieser, F.; Dagastine, R. R.; Chan, D. Y. C., Hydrodynamic Boundary Conditions and Dynamic Forces between Bubbles and Surfaces. *Phys Rev Lett* **2008**, *101*.

39. Schaeffel, D.; Koynov, K.; Vollmer, D.; Butt, H.-J.; Schoenecker, C., Local Flow Field and Slip Length of Superhydrophobic Surfaces. *Phys Rev Lett* **2016**, *116*, 134501.

40. Yang, J.; Duan, J.; Fornasiero, D.; Ralston, J., Kinetics of CO_2 Nanobubble Formation at the Solid/Water Interface. *Phys Chem Chem Phys* **2007**, *9*, 6327-6332.

41. Mazumder, M.; Bhushan, B., Propensity and Geometrical Distribution of Surface Nanobubbles: Effect of Electrolyte, Roughness, PH, and Substrate Bias. *Soft Matter* **2011**, *7*, 9184-9196.

42. Liu, Y. W.; Zhang, X. R., Nanobubble Stability Induced by Contact Line Pinning. *J Chem Phys* **2013**, *138*.

43. Chan, D. Y. C.; Uddin, M. H.; Cho, K. L.; Liaw, II; Lamb, R. N.; Stevens, G. W.; Grieser, F.; Dagastine, R. R., Silica Nano-Particle Super-Hydrophobic Surfaces: The

Effects of Surface Morphology and Trapped Air Pockets on Hydrodynamic Drainage Forces. *Faraday Discuss* **2009**, *143*, 151-168.

44. Zhang, X. Y.; Zhu, Y. X.; Granick, S., Hydrophobicity at a Janus Interface. *Science* **2002**, *295*, 663-666.

45. Donaldson, S. H.; Das, S.; Gebbie, M. A.; Rapp, M.; Jones, L. C.; Roiter, Y.; Koenig, P. H.; Gizaw, Y.; Israelachvili, J. N., Asymmetric Electrostatic and Hydrophobic-Hydrophilic Interaction Forces between Mica Surfaces and Silicone Polymer Thin Films. *Acs Nano* **2013**, *7*, 10094-10104.

46. Tyrrell, J. W. G.; Attard, P., Images of Nanobubbles on Hydrophobic Surfaces and Their Interactions. *Phys Rev Lett* **2001**, *87*.

47. Tyrrell, J. W. G.; Attard, P., Atomic Force Microscope Images of Nanobubbles on a Hydrophobic Surface and Corresponding Force-Separation Data. *Langmuir* **2002**, *18*, 160-167.

48. Parker, J. L.; Claesson, P. M.; Attard, P., Bubbles, Cavities, and the Long-Ranged Attraction between Hydrophobic Surfaces. *J Phys Chem-Us* **1994**, *98*, 8468-8480.

Chapter 6 Conclusions and future perspectives

The conclusions of this thesis and the recommendations for the future research are summarized in this chapter.

6.1 Conclusions

The integrated thin liquid film force apparatus (ITLFFA) was successfully developed to study the interaction between deformable and solid surfaces in aqueous electrolyte solutions, which can be extended to non-aqueous systems. Using the bimorph as a force sensor combined with the interferometry technique, the ITLFFA is capable of simultaneously measuring the time-dependent interaction force and the spatiotemporal film thickness. Equipped with a speaker diaphragm and a motorized actuator, the ITLFFA is able to control the precise displacement of deformable surfaces over a wide range of velocities. The accurate determination of the spatiotemporal film thickness allows the calculation of total interaction forces between the deformable and solid surfaces. The excellent agreement of the calculated and measured interaction force indicates the high accuracy of both force and film thickness measurements by our ITLFFA.

Interactions between an air bubble and hydrophilic silica surface in aqueous electrolyte solutions were investigated using ITLFFA to study the effect of salt concentration and bubble approach velocity over a wide range. The bubble approach velocity was found to determine the shape of the film profile and the first occurrence of dimple formation. The salt concentration only affects the drainage time and equilibrium film thickness. A good agreement between the experimental results and numerical calculations by Stokes-Reynolds-Young-Laplace (SRYL) model allows us to use the model to infer quantitative information on the distribution of the film pressure and the details of the fluid flow within the liquid film, which cannot be directly measured. Such an agreement also further verifies

the feasibility of simultaneous force and film thickness measurement as well as the appropriate use of SRYL model over a wider range of global Reynolds number.

The interactions between an air bubble and hydrophobized silica surface with different hydrophobicities and nanoroughness were also studied using ITLFFA. Unlike forming a stable flat film for hydrophilic surface, the film ruptured at film thickness as large as 100 nm for hydrophobic surface. The evolution of the film profile before the film rupture was quite different from that of hydrophilic case. By fitting the experimental film profile using modified Stokes-Reynolds-Young-Laplace (SRYL) model, the presence of apparent surface mobility beyond a critical approach velocity was found for hydrophobic surfaces. The nanobubbles or air layer on the hydrophobic surface with nanoroughness is believed to be the possible reason for the change of boundary condition in our study.

6.2 Recommendations for future research

Future research should address the following areas:

- The experiments in Chapter 5 show the existence of surface mobility at liquid-solid interface when the solid surface is hydrophobic with nanoroughness. It would be important to do the similar experiments on molecular smooth hydrophobic surfaces to reduce the influence of air layer on surface mobility. The possible way to limit the surface roughness is to use mica or the alcohol surface modification.
- In our current study, the millimeter size bubble was used for all the experiments. It was found that the bubble/droplet radius plays a significant role in the bubble/droplet coalescence. It would be interesting to study the micron size bubble and summarize the influence of bubble size on dynamic film drainage and film rupture process, especially that our instrument is able to cover a wide range of

approach velocity.

- The ITLFFA has been verified to provide important information when a deformable surface approaching a solid surface. The current study only uses an air bubble as an deformable surfaces. Thus, the extend study of using oil droplet or water droplet is good for comparison and other practical applications. In addition, the study of bubble-bubble interaction with dissimilar size is also valuable as it shed light on the optimization of flotation.
- The current study only focuses on the simple solid surfaces. The interactions between deformable and solid surfaces with various surface structures and properties are of great interest in industrial and biological processes. The study of interactions involving engineered surfaces can explain the mechanism of these processes and promote their performance.

Bibliography

Attard, P., Nanobubbles and the Hydrophobic Attraction. *Adv Colloid Interface Sci* **2003**, *104*, 75-91.

Barrat, J. L.; Bocquet, L., Large Slip Effect at a Nonwetting Fluid-Solid Interface. *Phys Rev Lett* **1999**, *82*, 4671-4674.

Baudry, J.; Charlaix, E.; Tonck, A.; Mazuyer, D., Experimental Evidence for a Large Slip Effect at a Nonwetting Fluid-Solid Interface. *Langmuir* **2001**, *17*, 5232-5236.

Berry, J. D.; Dagastine, R. R., Mapping Coalescence of Micron-Sized Drops and Bubbles. *J Colloid Interf Sci* **2017**, *487*, 513-522.

Bhatt, D.; Newman, J.; Radke, C. J., Equilibrium Force Isotherms of a Deformable Bubble/Drop Interacting with a Solid Particle across a Thin Liquid Film. *Langmuir* **2001**, *17*, 116-130.

Bonaccurso, E.; Butt, H. J.; Craig, V. S. J., Surface Roughness and Hydrodynamic Boundary Slip of a Newtonian Fluid in a Completely Wetting System. *Phys Rev Lett* **2003**, *90*, 144501.

Browne, C.; Tabor, R. F.; Chan, D. Y. C.; Dagastine, R. R.; Ashokkumar, M.; Grieser, F., Bubble Coalescence During Acoustic Cavitation in Aqueous Electrolyte Solutions. *Langmuir* **2011**, *27*, 12025-12032.

Butt, H. J., A Technique for Measuring the Force between a Colloidal Particle in Water and a Bubble. *J Colloid Interf Sci* **1994**, *166*, 109-117.

Carnie, S. L.; Chan, D. Y. C.; Lewis, C.; Manica, R.; Dagastine, R. R., Measurement of Dynamical Forces between Deformable Drops Using the Atomic Force Microscope. I. Theory. *Langmuir* **2005**, *21*, 2912-2922.

Chan, C. U.; Ohl, C. D., Total-Internal-Reflection-Fluorescence Microscopy for the Study of Nanobubble Dynamics. *Phys Rev Lett* **2012**, *109*, 174501.

Chan, D. Y. C.; Dagastine, R. R.; White, L. R., Forces between a Rigid Probe Particle and a Liquid Interface - I. The Repulsive Case. *J Colloid Interf Sci* **2001**, *236*, 141-154.

Chan, D. Y. C.; Klaseboer, E.; Manica, R., Dynamic Interactions between Deformable Drops in the Hele-Shaw Geometry. *Soft Matter* **2010**, *6*, 1809-1815.

Chan, D. Y. C.; Klaseboer, E.; Manica, R., Film Drainage and Coalescence between Deformable Drops and Bubbles. *Soft Matter* **2011**, *7*, 2235-2264.

Chan, D. Y. C.; Klaseboer, E.; Manica, R., Theory of Non-Equilibrium Force Measurements Involving Deformable Drops and Bubbles. *Adv Colloid Interface Sci* **2011**, *165*, 70-90.

Chan, D. Y. C.; Uddin, M. H.; Cho, K. L.; Liaw, II; Lamb, R. N.; Stevens, G. W.; Grieser, F.; Dagastine, R. R., Silica Nano-Particle Super-Hydrophobic Surfaces: The Effects of Surface Morphology and Trapped Air Pockets on Hydrodynamic Drainage Forces. *Faraday Discuss* **2009**, *143*, 151-168.

Chen, J.; Gomez, J. A.; Hoffner, K.; Barton, P. I.; Henson, M. A., Metabolic Modeling of Synthesis Gas Fermentation in Bubble Column Reactors. *Biotechnol Biofuels* **2015**, *8*, 89.

Choi, C. H.; Kim, C. J., Large Slip of Aqueous Liquid Flow over a Nanoengineered Superhydrophobic Surface. *Phys Rev Lett* **2006**, *96*, 066001.

Choi, C. H.; Ulmanella, U.; Kim, J.; Ho, C. M.; Kim, C. J., Effective Slip and Friction Reduction in Nanograted Superhydrophobic Microchannels. *Phys Fluids* **2006**, *18*, 087105.

Christenson, H. K.; Claesson, P. M., Cavitation and the Interaction between Macroscopic Hydrophobic Surfaces. *Science* **1988**, *239*, 390-392.

Chuang, E. Y.; Lin, K. J.; Lin, P. Y.; Chen, H. L.; Wey, S. P.; Mi, F. L.; Hsiao, H. C.; Chen, C. T.; Sung, H. W., Self-Assembling Bubble Carriers for Oral Protein Delivery. *Biomaterials* **2015**, *64*, 115-124.

Claesson, P. M.; Christenson, H. K., Very Long-Range Attractive Forces between Uncharged Hydrocarbon and Fluorocarbon Surfaces in Water. *J Phys Chem-Us* **1988**, *92*, 1650-1655.

Connor, J. N.; Horn, R. G., The Influence of Surface Forces on Thin Film Drainage between a Fluid Drop and a Flat Solid. *Faraday Discuss* **2003**, *123*, 193-206.

Cottin-Bizonne, C.; Barrat, J. L.; Bocquet, L.; Charlaix, E., Low-Friction Flows of Liquid at Nanopatterned Interfaces. *Nat Mater* **2003**, *2*, 237-240.

Cottin-Bizonne, C.; Cross, B.; Steinberger, A.; Charlaix, E., Boundary Slip on Smooth Hydrophobic Surfaces: Intrinsic Effects and Possible Artifacts. *Phys Rev Lett* **2005**, *94*, 056102.

Craig, V. S. J.; Neto, C.; Williams, D. R. M., Shear-Dependent Boundary Slip in an Aqueous Newtonian Liquid. *Phys Rev Lett* **2001**, *87*, 054504.

Dagastine, R. R.; Manica, R.; Carnie, S. L.; Chan, D. Y. C.; Stevens, G. W.; Grieser, F., Dynamic Forces between Two Deformable Oil Droplets in Water. *Science* **2006**, *313*, 210-213.

Derjaguin, B.; Kussakov, M., Anomalousproperties of Thin Polymolecular Films V. An Experimental Investigation of Polymolecular Solvate (Adsorbed) Films as Applied to the Development of a Mathematical Theory of the Stability of Colloids. *Acta Physicochim Urs* **1939**, *10*, 25-44.

Dimitrov, D. S.; Ivanov, I. B., Hydrodynamics of Thin Liquid-Films - Rate of Thinning of

Microscopic Films with Deformable Interfaces. *J Colloid Interf Sci* **1978**, *64*, 97-106.

Djikaev, Y. S.; Ruckenstein, E., A Probabilistic Approach to the Effect of Hydrogen Bonding on the Hydrophobic Attraction. *J Chem Phys* **2009**, *130*, 124713.

Ducker, W. A.; Senden, T. J.; Pashley, R. M., Direct Measurement of Colloidal Forces Using an Atomic Force Microscope. *Nature* **1991**, *353*, 239-241.

Ducker, W. A.; Xu, Z. G.; Israelachvili, J. N., Measurements of Hydrophobic and Dlvo Forces in Bubble-Surface Interactions in Aqueous-Solutions. *Langmuir* **1994**, *10*, 3279-3289.

Fisher, L. R.; Hewitt, D.; Mitchell, E. E.; Ralston, J.; Wolfe, J., The Drainage of an Aqueous Film between a Solid Plane and an Air Bubble. *Adv Colloid Interface Sci* **1992**, *39*, 397-416.

Fisher, L. R.; Mitchell, E. E.; Hewitt, D.; Ralston, J.; Wolfe, J., The Drainage of a Thin Aqueous Film between a Solid-Surface and an Approaching Gas Bubble. *Colloids Surf* **1991**, *52*, 163-174.

Frankel, S. P.; Mysels, K. J., On Dimpling During Approach of Two Interfaces. *J Phys Chem-Us* **1962**, *66*, 190-191.

Frostad, J. M.; Collins, M. C.; Leal, L. G., Cantilevered-Capillary Force Apparatus for Measuring Multiphase Fluid Interactions. *Langmuir* **2013**, *29*, 4715-4725.

Hampton, M. A.; Donose, B. C.; Nguyen, A. V., Effect of Alcohol-Water Exchange and Surface Scanning on Nanobubbles and the Attraction between Hydrophobic Surfaces. *J Colloid Interf Sci* **2008**, *325*, 267-274.

Hampton, M. A.; Nguyen, A. V., Nanobubbles and the Nanobubble Bridging Capillary Force. *Adv Colloid Interface Sci* **2010**, *154*, 30-55.

Hartland, S.; Robinson, J. D., Model for an Axisymmetric Dimpled Draining Film. *J Colloid Interf Sci* **1977**, *60*, 72-81.

Hendrix, M. H. W.; Manica, R.; Klaseboer, E.; Chan, D. Y. C.; Ohl, C. D., Spatiotemporal Evolution of Thin Liquid Films During Impact of Water Bubbles on Glass on a Micrometer to Nanometer Scale. *Phys Rev Lett* **2012**, *108*, 247803.

Hewitt, D.; Fornasiero, D.; Ralston, J.; Fisher, L. R., Aqueous Film Drainage at the Quartz Water Air Interface. *J Chem Soc Faraday T* **1993**, *89*, 817-822.

Horn, R. G.; Asadullah, M.; Connor, J. N., Thin Film Drainage: Hydrodynamic and Disjoining Pressures Determined from Experimental Measurements of the Shape of a Fluid Drop Approaching a Solid Wall. *Langmuir* **2006**, *22*, 2610-2619.

Ishida, N.; Inoue, T.; Miyahara, M.; Higashitani, K., Nano Bubbles on a Hydrophobic Surface in Water Observed by Tapping-Mode Atomic Force Microscopy. *Langmuir* **2000**, *16*, 6377-6380.

Ishida, N.; Kusaka, Y.; Ushijima, H., Hydrophobic Attraction between Silanated Silica Surfaces in the Absence of Bridging Bubbles. *Langmuir* **2012**, *28*, 13952-13959.

Ishida, N.; Sakamoto, M.; Miyahara, M.; Higashitani, K., Attraction between Hydrophobic Surfaces with and without Gas Phase. *Langmuir* **2000**, *16*, 5681-5687.

Israelachvili, J., et al., Recent Advances in the Surface Forces Apparatus (SFA) Technique. *Rep Prog Phys* **2010**, *73*, 036601.

Israelachvili, J.; Pashley, R., The Hydrophobic Interaction Is Long-Range, Decaying Exponentially with Distance. *Nature* **1982**, *300*, 341-342.

Jain, R. K.; Ivanov, I. B., Thinning and Rupture of Ring-Shaped Films. *J Chem Soc Farad T 2* **1980**, *76*, 250-266.

Joseph, P.; Cottin-Bizonne, C.; Benoit, J. M.; Ybert, C.; Journet, C.; Tabeling, P.; Bocquet, L., Slippage of Water Past Superhydrophobic Carbon Nanotube Forests in Microchannels. *Phys Rev Lett* **2006**, *97*, 156104.

Joseph, P.; Tabeling, P., Direct Measurement of the Apparent Slip Length. *Phys Rev E* **2005**, *71*, 035303.

Kaggwa, G. B.; Nalam, P. C.; Kilpatrick, J. I.; Spencer, N. D.; Jarvis, S. P., Impact of Hydrophilic/Hydrophobic Surface Chemistry on Hydration Forces in the Absence of Confinement. *Langmuir* **2012**, *28*, 6589-6594.

Kolarov, T.; Zorin, Z.; Platikanov, D., Profile of the Transition Region between Aqueous Wetting Films on Quartz and the Adjacent Meniscus. *Colloids Surf* **1990**, *51*, 37-47.

Kosior, D.; Zawala, J.; Krasowska, M.; Malysa, K., Influence of N-Octanol and Alpha-Terpineol on Thin Film Stability and Bubble Attachment to Hydrophobic Surface. *Phys Chem Chem Phys* **2013**, *15*, 2586-2595.

Krasowska, M.; Malysa, K., Wetting Films in Attachment of the Colliding Bubble. *Adv Colloid Interface Sci* **2007**, *134-35*, 138-150.

Lasne, D.; Maali, A.; Amarouchene, Y.; Cognet, L.; Lounis, B.; Kellay, H., Velocity Profiles of Water Flowing Past Solid Glass Surfaces Using Fluorescent Nanoparticles and Molecules as Velocity Probes. *Phys Rev Lett* **2008**, *100*, 214502.

Lauga, E.; Brenner, M. P., Dynamic Mechanisms for Apparent Slip on Hydrophobic Surfaces. *Phys Rev E* **2004**, *70*, 026311.

Lee, C.; Choi, C. H.; Kim, C. J., Structured Surfaces for a Giant Liquid Slip. *Phys Rev Lett* **2008**, *101*, 064501.

Lee, C.; Kim, C. J., Influence of Surface Hierarchy of Superhydrophobic Surfaces on

Liquid Slip. *Langmuir* **2011**, *27*, 4243-4248.

Lee, D. J.; Cho, K. Y.; Jang, S.; Song, Y. S.; Youn, J. R., Liquid Slip on a Nanostructured Surface. *Langmuir* **2012**, *28*, 10488-10494.

Li, L. X.; Kazoe, Y.; Mawatari, K.; Sugii, Y.; Kitamori, T., Viscosity and Wetting Property of Water Confined in Extended Nanospace Simultaneously Measured from Highly-Pressurized Meniscus Motion. *J Phys Chem Lett* **2012**, *3*, 2447-2452.

Li, Z. L.; Yoon, R. H., Thermodynamics of Hydrophobic Interaction between Silica Surfaces Coated with Octadecyltrichlorosilane. *J Colloid Interf Sci* **2013**, *392*, 369-375.

Liu, Y. W.; Zhang, X. R., Nanobubble Stability Induced by Contact Line Pinning. *J Chem Phys* **2013**, *138*.

Lockie, H. J.; Manica, R.; Stevens, G. W.; Grieser, F.; Chan, D. Y. C.; Dagastine, R. R., Precision AFM Measurements of Dynamic Interactions between Deformable Drops in Aqueous Surfactant and Surfactant-Free Solutions. *Langmuir* **2011**, *27*, 2676-2685.

Malysa, K.; Krasowska, M.; Krzan, M., Influence of Surface Active Substances on Bubble Motion and Collision with Various Interfaces. *Adv Colloid Interface Sci* **2005**, *114*, 205-225.

Manica, R.; Chan, D. Y. C., Drainage of the Air-Water-Quartz Film: Experiments and Theory. *Phys Chem Chem Phys* **2011**, *13*, 1434-1439.

Manica, R.; Connor, J. N.; Carnie, S. L.; Horn, R. G.; Chan, D. Y. C., Dynamics of Interactions Involving Deformable Drops: Hydrodynamic Dimpling under Attractive and Repulsive Electrical Double Layer Interactions. *Langmuir* **2007**, *23*, 626-637.

Manica, R.; Parkinson, L.; Ralston, J.; Chan, D. Y. C., Interpreting the Dynamic Interaction between a Very Small Rising Bubble and a Hydrophilic Titania Surface. *J Phys Chem C*

2010, *114*, 1942-1946.

Manor, O.; Vakarelski, I. U.; Stevens, G. W.; Grieser, F.; Dagastine, R. R.; Chan, D. Y. C., Dynamic Forces between Bubbles and Surfaces and Hydrodynamic Boundary Conditions. *Langmuir* **2008**, *24*, 11533-11543.

Manor, O.; Vakarelski, I. U.; Tang, X. S.; O'Shea, S. J.; Stevens, G. W.; Grieser, F.; Dagastine, R. R.; Chan, D. Y. C., Hydrodynamic Boundary Conditions and Dynamic Forces between Bubbles and Surfaces. *Phys Rev Lett* **2008**, *101*.

Mazumder, M.; Bhushan, B., Propensity and Geometrical Distribution of Surface Nanobubbles: Effect of Electrolyte, Roughness, Ph, and Substrate Bias. *Soft Matter* **2011**, *7*, 9184-9196.

Meyer, E. E.; Lin, Q.; Hassenkam, T.; Oroudjev, E.; Israelachvili, J. N., Origin of the Long-Range Attraction between Surfactant-Coated Surfaces. *P Natl Acad Sci USA* **2005**, *102*, 6839-6842.

Miklavic, S. J.; Chan, D. Y. C.; White, L. R.; Healy, T. W., Double-Layer Forces between Heterogeneous Charged Surfaces. *J Phys Chem-Us* **1994**, *98*, 9022-9032.

Nedyalkov, M.; Alexandrova, L.; Platikanov, D.; Levecke, B.; Tadros, T., Wetting Films on a Hydrophilic Silica Surface Obtained from Aqueous Solutions of Hydrophobically Modified Inulin Polymeric Surfactant. *Colloid Polym Sci* **2007**, *285*, 1713-1717.

Neto, C.; Craig, V. S. J.; Williams, D. R. M., Evidence of Shear-Dependent Boundary Slip in Newtonian Liquids. *Eur Phys J E* **2003**, *12*, S71-S74.

Neto, C.; Evans, D. R.; Bonaccurso, E.; Butt, H. J.; Craig, V. S. J., Boundary Slip in Newtonian Liquids: A Review of Experimental Studies. *Rep Prog Phys* **2005**, *68*, 2859-2897.

Nguyen, A. V.; Ralston, J.; Schulze, H. J., On Modelling of Bubble-Particle Attachment Probability in Flotation. *Int J Miner Process* **1998**, *53*, 225-249.

Niecikowska, A.; Krasowska, M.; Ralston, J.; Malysa, K., Role of Surface Charge and Hydrophobicity in the Three-Phase Contact Formation and Wetting Film Stability under Dynamic Conditions. *J Phys Chem C* **2012**, *116*, 3071-3078.

Nonaka, M., A Waste-Water Treatment System Applying Aeration-Cavitation Flotation Mechanism. *Sep Sci Technol* **1986**, *21*, 457-474.

Palmer, L. A.; Cookson, D.; Lamb, R. N., The Relationship between Nanobubbles and the Hydrophobic Force. *Langmuir* **2011**, *27*, 144-147.

Pan, L.; Jung, S.; Yoon, R. H., Effect of Hydrophobicity on the Stability of the Wetting Films of Water Formed on Gold Surfaces. *J Colloid Interf Sci* **2011**, *361*, 321-330.

Parker, J. L.; Claesson, P. M.; Attard, P., Bubbles, Cavities, and the Long-Ranged Attraction between Hydrophobic Surfaces. *J Phys Chem-Us* **1994**, *98*, 8468-8480.

Parkinson, L.; Ralston, J., The Interaction between a Very Small Rising Bubble and a Hydrophilic Titania Surface. *J Phys Chem C* **2010**, *114*, 2273-2281.

Pit, R.; Hervet, H.; Leger, L., Friction and Slip of a Simple Liquid at a Solid Surface. *Tribol Lett.* **1999**, *7*, 147-152.

Pit, R.; Hervet, H.; Leger, L., Direct Experimental Evidence of Slip in Hexadecane: Solid Interfaces. *Phys Rev Lett* **2000**, *85*, 980-983.

Platikanov, D., Experimental Investigation on Dimpling of Thin Liquid Films. *J Phys Chem-Us* **1964**, *68*, 3619-3624.

Pushkarova, R. A.; Horn, R. G., Bubble-Solid Interactions in Water and Electrolyte Solutions. *Langmuir* **2008**, *24*, 8726-8734.

Rabinovich, Y. I.; Guzonas, D. A.; Yoon, R. H., Role of Chain Order in the Long-Range Attractive Force between Hydrophobic Surfaces. *Langmuir* **1993**, *9*, 1168-1170.

Ralston, J.; Fornasiero, D.; Hayes, R., Bubble-Particle Attachment and Detachment in Flotation. *Int J Miner Process* **1999**, *56*, 133-164.

Schaffel, D.; Koynov, K.; Vollmer, D.; Butt, H. J.; Schonecker, C., Local Flow Field and Slip Length of Superhydrophobic Surfaces. *Phys Rev Lett* **2016**, *116*, 134501.

Shi, C.; Chan, D. Y. C.; Liu, Q. X.; Zeng, H. B., Probing the Hydrophobic Interaction between Air Bubbles and Partially Hydrophobic Surfaces Using Atomic Force Microscopy. *J Phys Chem C* **2014**, *118*, 25000-25008.

Shi, C.; Cui, X.; Xie, L.; Liu, Q. X.; Chan, D. Y. C.; Israelachvili, J. N.; Zeng, H. B., Measuring Forces and Spatiotemporal Evolution of Thin Water Films between an Air Bubble and Solid Surfaces of Different Hydrophobicity. *Acs Nano* **2015**, *9*, 95-104.

Tabor, R. F.; Chan, D. Y. C.; Grieser, F.; Dagastine, R. R., Anomalous Stability of Carbon Dioxide in PH-Controlled Bubble Coalescence. *Angew Chem Int Edit* **2011**, *50*, 3454-3456.

Tabor, R. F.; Grieser, F.; Dagastine, R. R.; Chan, D. Y. C., The Hydrophobic Force: Measurements and Methods. *Phys Chem Chem Phys* **2014**, *16*, 18065-18075.

Tabor, R. F.; Lockie, H.; Mair, D.; Manica, R.; Chan, D. Y. C.; Grieser, F.; Dagastine, R. R., Combined AFM-Confocal Microscopy of Oil Droplets: Absolute Separations and Forces in Nanofilms. *J Phys Chem Lett* **2011**, *2*, 961-965.

Tabor, R. F.; Manica, R.; Chan, D. Y. C.; Grieser, F.; Dagastine, R. R., Repulsive van Der Waals Forces in Soft Matter: Why Bubbles Do Not Stick to Walls. *Phys Rev Lett* **2011**, *106*, 064501.

Tabor, R. F.; Wu, C.; Grieser, F.; Dagastine, R. R.; Chan, D. Y. C., Measurement of the

Hydrophobic Force in a Soft Matter System. *J Phys Chem Lett* **2013**, *4*, 3872-3877.

Thompson, P. A.; Troian, S. M., A General Boundary Condition for Liquid Flow at Solid Surfaces. *Nature* **1997**, *389*, 360-362.

Tretheway, D. C.; Meinhart, C. D., Apparent Fluid Slip at Hydrophobic Microchannel Walls. *Phys Fluids* **2002**, *14*, L9-L12.

Tretheway, D. C.; Meinhart, C. D., A Generating Mechanism for Apparent Fluid Slip in Hydrophobic Microchannels. *Phys Fluids* **2004**, *16*, 1509-1515.

Tsao, Y. H.; Evans, D. F.; Wennerstrom, H., Long-Range Attractive Force between Hydrophobic Surfaces Observed by Atomic-Force Microscopy. *Science* **1993**, *262*, 547-550.

Tsao, Y. H.; Yang, S. X.; Evans, D. F.; Wennerstrom, H., Interactions between Hydrophobic Surfaces - Dependence on Temperature and Alkyl Chain-Length. *Langmuir* **1991**, *7*, 3154-3159.

Tsukahara, T.; Hibara, A.; Ikeda, Y.; Kitamori, T., NMR Study of Water Molecules Confined in Extended Nanospaces. *Angew Chem Int Edit* **2007**, *46*, 1180-1183.

Tyrrell, J. W. G.; Attard, P., Images of Nanobubbles on Hydrophobic Surfaces and Their Interactions. *Phys Rev Lett* **2001**, *87*.

Tyrrell, J. W. G.; Attard, P., Atomic Force Microscope Images of Nanobubbles on a Hydrophobic Surface and Corresponding Force-Separation Data. *Langmuir* **2002**, *18*, 160-167.

Vakarelski, I. U.; Lee, J.; Dagastine, R. R.; Chan, D. Y. C.; Stevens, G. W.; Grieser, F., Bubble Colloidal Afm Probes Formed from Ultrasonically Generated Bubbles. *Langmuir* **2008**, *24*, 603-605.

Vakarelski, I. U.; Manica, R.; Tang, X. S.; O'Shea, S. J.; Stevens, G. W.; Grieser, F.; Dagastine, R. R.; Chan, D. Y. C., Dynamic Interactions between Microbubbles in Water. *P Natl Acad Sci USA* **2010**, *107*, 11177-11182.

Vinogradova, O. I., Drainage of a Thin Liquid-Film Confined between Hydrophobic Surfaces. *Langmuir* **1995**, *11*, 2213-2220.

Vinogradova, O. I., Slippage of Water over Hydrophobic Surfaces. *Int J Miner Process* **1999**, *56*, 31-60.

Wang, J. L.; Yoon, R. H.; Eriksson, J. C., Excess Thermodynamic Properties of Thin Water Films Confined between Hydrophobized Gold Surfaces. *J Colloid Interf Sci* **2011**, *364*, 257-263.

Wang, L. X.; Sharp, D.; Masliyah, J.; Xu, Z. H., Measurement of Interactions between Solid Particles, Liquid Droplets, and/or Gas Bubbles in a Liquid Using an Integrated Thin Film Drainage Apparatus. *Langmuir* **2013**, *29*, 3594-3603.

Webber, G. B.; Manica, R.; Edwards, S. A.; Carnie, S. L.; Stevens, G. W.; Grieser, F.; Dagastine, R. R.; Chan, D. Y. C., Dynamic Forces between a Moving Particle and a Deformable Drop. *J Phys Chem C* **2008**, *112*, 567-574.

Yang, J.; Duan, J.; Fornasiero, D.; Ralston, J., Kinetics of CO_2 Nanobubble Formation at the Solid/Water Interface. *Phys Chem Chem Phys* **2007**, *9*, 6327-6332.

Ybert, C.; Barentin, C.; Cottin-Bizonne, C.; Joseph, P.; Bocquet, L., Achieving Large Slip with Superhydrophobic Surfaces: Scaling Laws for Generic Geometries. *Phys Fluids* **2007**, *19*, 123601.

Zhang, X. H.; Kumar, A.; Scales, P. J., Effects of Solvency and Interfacial Nanobubbles on Surface Forces and Bubble Attachment at Solid Surfaces. *Langmuir* **2011**, *27*, 2484-

2491.

Zhang, X. H.; Zhang, X. D.; Lou, S. T.; Zhang, Z. X.; Sun, J. L.; Hu, J., Degassing and Temperature Effects on the Formation of Nanobubbles at the Mica/Water Interface. *Langmuir* **2004**, *20*, 3813-3815.

Zhu, L. W.; Neto, C.; Attard, P., Reliable Measurements of Interfacial Slip by Colloid Probe Atomic Force Microscopy. Iii. Shear-Rate-Dependent Slip. *Langmuir* **2012**, *28*, 3465-3473.

Zhu, Y. X.; Granick, S., Rate-Dependent Slip of Newtonian Liquid at Smooth Surfaces. *Phys Rev Lett* **2001**, *87*, 096105.

Zhu, Y. X.; Granick, S., Limits of the Hydrodynamic No-Slip Boundary Condition. *Phys Rev Lett* **2002**, *88*, 106102.

Zorin, Z.; Platikanov, D.; Kolarov, T., The Transition Region between Aqueous Wetting Films on Quartz and the Adjacent Meniscus. *Colloids Surf* **1987**, *22*, 147-159.

Appendix A

Additional calculations for Chapter 3

Calculating the equilibrium film thickness using DLVO theory

When the film drains to the flat equilibrium film, the Laplace pressure inside the bubble ($\frac{2\gamma}{R}$) equals to the total disjoining pressure Π, which is given by the sum of van der Waals interaction Π_{vdw} and electrical double-layer interaction Π_{edl}:

$$\frac{2\gamma}{R} = \Pi = \Pi_{vdw} + \Pi_{edl} \tag{A1}$$

The van der Waals interaction is calculated as:

$$\Pi_{vdw} = -\frac{A}{6\pi h^3} \tag{A2}$$

where h is the film thickness and A is the Hamaker constant. In our system, the value of A is taken to be -1.1×10^{-20} J according to the literature[1].

The electrical double-layer interaction is obtained by using the following equation derived by Verwey and Overbeek[2]:

$$\Pi_{edl} = 64nkT * \tanh\left(\frac{ze\varphi_{sl}}{4kT}\right) * \tanh\left(\frac{ze\varphi_{bl}}{4kT}\right) \exp(-\kappa h) \tag{A3}$$

where n is the number of electrolyte ions per unit volume in the aqueous film, k is the Boltzmann constant, ze is the charge on the electrolyte ions, T is the absolute temperature and κ^{-1} is the Debye length. φ_{sl} and φ_{bl} are the surface potential of surface-liquid and bubble-liquid interface, respectively.

In our system, the ionic strength of Milli-Q water is regarded as 5.6×10^{-6} mol/L, φ_{sl} is measured to be -148 mV and φ_{bl} is chosen to be -40 mV which is reasonable according to the literature[1, 3]. Thus, the equilibrium film thickness is calculated to be 114 nm which matches the experimental results.

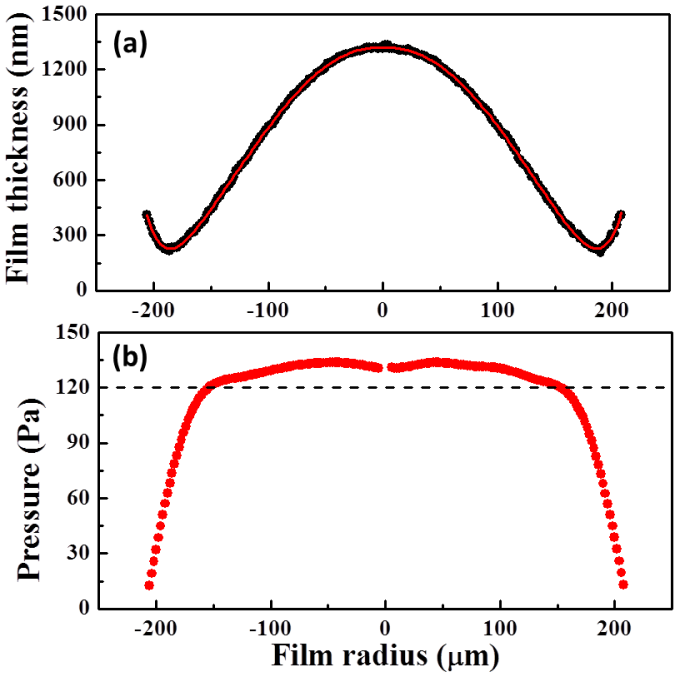

Figure A1. (a) Typical raw data of film thickness as a function of film radius (points) and film profile after smoothing (solid line) of a bubble interacting with a hydrophilic surface in Milli-Q water. (b) The total film pressure profile obtained for the film profile in (a).

An example of calculating film pressure from the spatial film profile

A typical result of film pressure calculated based on the measured film profile was exhibited in Figure A1 (b). In this case, there are 208 data points in the film profile (points in Figure A1 (a)). The smoothed profile is the solid curve in Figure A1 (a). The number of data points used in each local regression of Savitzky-Golay ("window size") was chosen to be 20. This number has to be optimized to acquire good smoothness for each film profile. The acceptable smoothness is indicated by conservation of the features of the raw data and lack of oscillation in the first and second derivatives of film thickness. In general, the results presented in this paper were all attained with the "window size" between 20 and 80. The axial symmetry of this system demands that the pressure profile on the left and right

sides should be the same. The small difference between the two pressure profiles on the left and right sides of Figure A1 (b) is due to the reasonable uncertainty in pressure determined by this method. Note that eqn (3-7) contains a singularity at $r=0$, which can be handled by using l'Hospital rule to obtain continuous pressure profile at $r=0$.

References

1. Hewitt, D.; Fornasiero, D.; Ralston, J.; Fisher, L. R., Aqueous Film Drainage at the Quartz Water Air Interface. *J Chem Soc Faraday T* **1993**, *89*, 817-822.

2. Overbeek, E. J. W. V. a. J. T. G., *Theory of the Stability of Lyophobic Colloids*; Elsevier: Amsterdam, 1948.

3. Graciaa, A.; Morel, G.; Saulner, P.; Lachaise, J.; Schechter, R. S., The Zeta-Potential of Gas-Bubbles. *J Colloid Interf Sci* **1995**, *172*, 131-136.

Appendix B

Additional calculations for Chapter 4

Calculation of the shear rate at the bubble-liquid interface

As mentioned in Chapter 4, the flow in the thin film trapped by the bubble and solid surface can be regarded as Stokes flow. According to the lubrication theory, the velocity of the flow in the radial r-direction, $u(r,z,t)$, is given by:

$$\mu \frac{\partial^2 u(r,z,t)}{\partial z^2} = \frac{\partial p(r,t)}{\partial r} \tag{B-1}$$

where μ is the viscosity of the liquid and $p(r,t)$ is the pressure in the r-direction. Integrating eqn. (B-1) with respect to z twice, $u(r,z,t)$ can be written as:

$$u(r,z,t) = \frac{1}{\mu}\frac{\partial p(r,t)}{\partial r}\left(\frac{z^2}{2} + c_1 z + c_2\right) \tag{B-2}$$

With the no-slip boundary condition for both solid-liquid and bubble-liquid interface, that is $u(r,z,t) = 0$ at $z = 0$ and $z = h$, the value of c_1 and c_2 can be obtained and the velocity of the flow in the trapped thin film can be expressed as:

$$u(r,z,t) = \frac{1}{\mu}\frac{\partial p(r,t)}{\partial r}\left(\frac{z^2}{2} - \frac{hz}{2}\right) \tag{B-3}$$

The shear rate for a fluid flowing between two parallel plates, one of which is moving at a constant speed and the other of which is stationary is defined by:

$$\dot{\gamma} = \frac{v}{h} \tag{B-4}$$

where v is the velocity if the moving plates and h is the distance between the plates. Therefore, in our system that is similar to the condition described above, the shear rate has the form:

$$\dot{\gamma} = -\frac{du}{dz} \tag{B-5}$$

Combining eqn. (B-5) with eqn. (B-3), the shear rate at the bubble-liquid interface ($z = h$) can be written as:

$$\dot{\gamma} = -\frac{h}{2\mu}\frac{\partial p(r,t)}{\partial r} \tag{B-6}$$

The relationship between drainage time and capillary number

As the film thickness of dimple formation increased with the increasing approach velocity (Figure 4-10), the more pronounced dimple resulted in longer film drainage time (Figure B1). In addition, the narrow neck at the barrier rim of the film in high salt concentration prolonged the drainage time compared to that in low salt concentration.

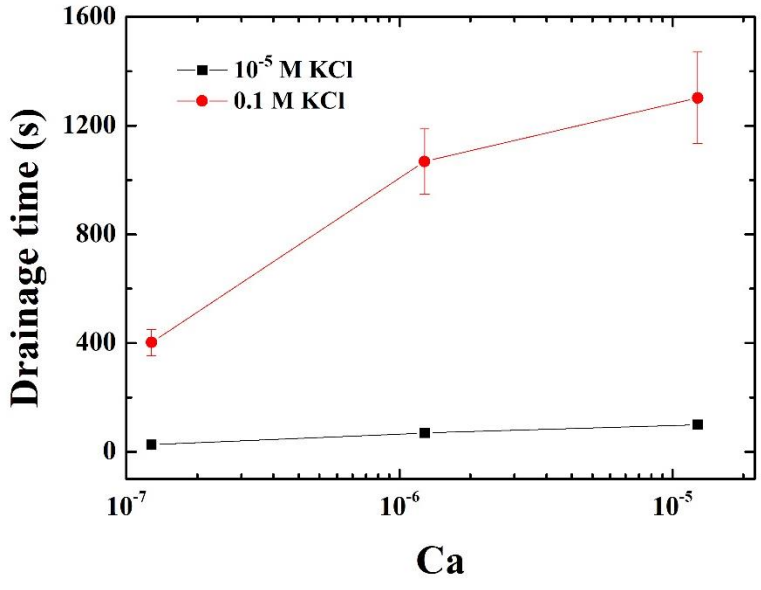

Figure B1. Drainage time as a function of capillary number in different salt concentrations.

Appendix C

Additional figures for Chapter 5

Displacement and velocity of the capillary

The displacement of the capillary that drives the bubble against the surface is controlled accurately by a motorized actuator. The system was programed to move a displacement of 400 µm at the velocity of 1mm/s. The total displacement was achieved exactly (Figure C1). The displacement signal was matched to a sixth order polynomial to obtain the bubble approach velocity using the derivative of the polynomial (Figure C1). Though the approach velocity was set to be 1 mm/s, the total displacement is too short for the velocity to stabilize. The curve shows an initial acceleration and later the velocity reduces to zero after about 0.55 s. This experimental velocity as shown here was used in the numerical code as the driving function rather than assuming a constant velocity of 1mm/s, which was essential in capturing the excellent agreement between theory and experiments shown in the main manuscript.

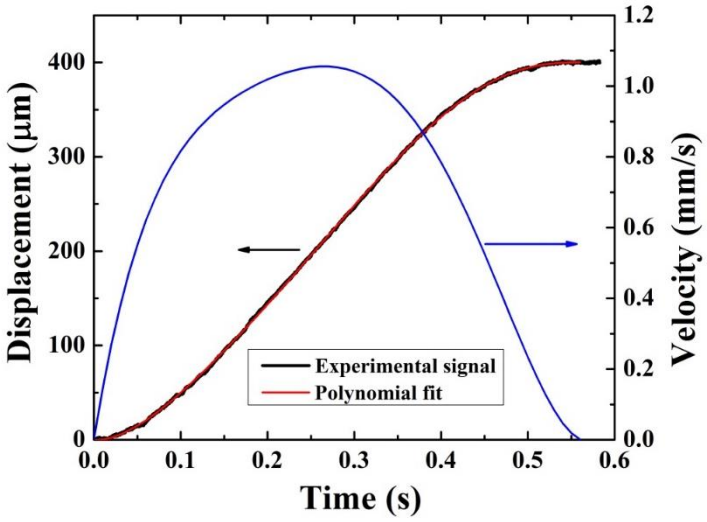

Figure C1. Displacement and velocity of bubble when the motorized actuator was programed to travel a displacement of 400 µm at a velocity of 1 mm/s.

The contact angle measurements and AFM images of hydrophobic surfaces

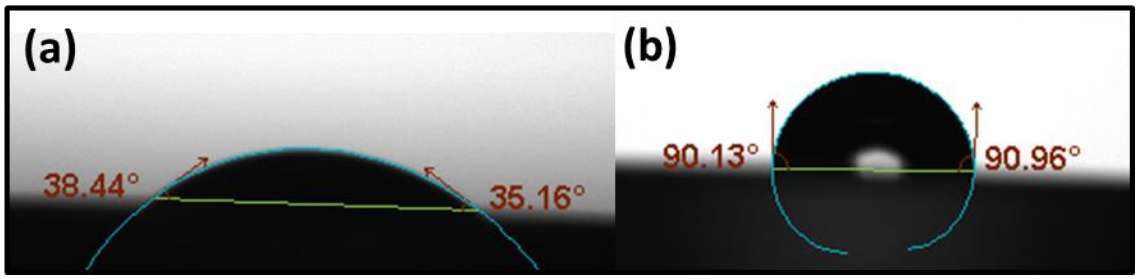

Figure C2. Water contact angle of (a) 36° and (b) 90° on hydrophobized silica glass surface.

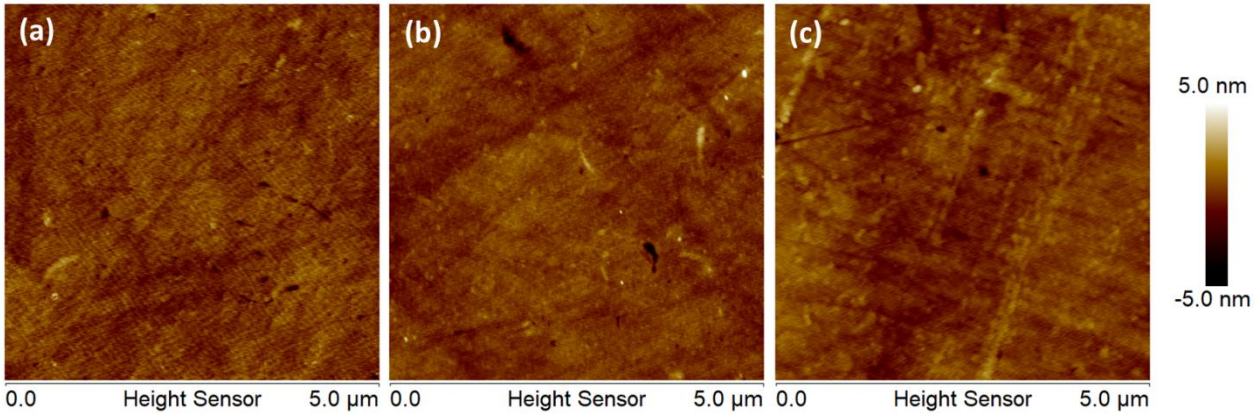

Figure C3. AFM topography images of (a) hydrophilic silica glass surface and hydrophobized silica glass surfaces with water contact angle of (b) 36° and (c) 90°.

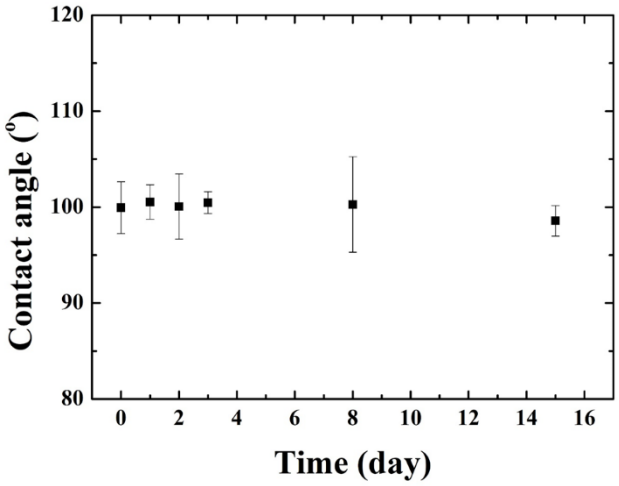

Figure C4. Water contact angle of hydrophobic surface as a function of time.

As shown in Figure C4, hydrophobicity of the surface that was hydrophobized using silane solution is quite stable without noticeable change for two weeks.